# Characterization of Iron Oxide Nanoparticles (IONPs) for Brain Targeted Delivery

**By**
**Zhizhi Sun**

**A thesis submitted to**
**the Faculty of Graduate Studies**
**in partial fulfillment**
**of the requirements for the degree of**
**DOCTOR OF PHILOSOPHY**

**Department of Pharmacology and Therapeutics**
**Faculty of Medicine**
**University of Manitoba**

# Abstract

The restrictive nature of the brain endothelial cells that form the blood-brain barrier (BBB) limits both the paracellular and transcellular passage of many molecules into the brain. Therefore, effective treatment of brain disorders requires a focus on improving drug permeability across the BBB. This thesis focuses on characterization and optimization of iron oxide nanoparticles (IONPs) as a potential platform for drug delivery to the brain. Given concerns with metal toxicity in the brain, we first examined the biocompatibility and cellular uptake profile of positively and negatively charged IONPs in brain endothelial cells, astrocytes, and neurons. These *in vitro* studies showed both IONP formulations were well tolerated at concentrations less than 100ug/mL, and that positively charged IONPs have a greater uptake profile than negatively charged IONPs across all cell types examined. It is hypothesized that transient disruption of the BBB combined with the application of a magnetic field, a process we have termed "Magnetic Field Enhanced Covective Diffusion" (MFECD), could be used to enhance IONPs penetration of the BBB. Using the cell culture model of the BBB, disruption of tight junctions with a hyperosmotic mannitol solution resulted in significant increases in permeability for the negatively charged IONP. Even further enhancement of negatively charged IONP permeability was observed when an external magnetic field was applied. Positively charged IONPs showed no significant change in permeability to osmotic disruption or magnetic field. Encouraged by the *in vitro* permeability studies, the pharmacokinetic properties of negatively charged IONPs was examined in healthy mice under control conditions or following transient BBB disruption using lysophosphatidic acid (LPA). Under normal conditions, IONPs had half-life of 6 minutes and liver and spleen were the major organs of IONP deposition, with limited distribution to the brain. Treatment with LPA significantly enhanced the brain accumulation of IONPs. In addition,

examination of microglia and astrocyte activation showed transient BBB disruption and enhanced IONP accumulation in the brain did not lead to inflammation or toxicity. Together, our findings suggest transient disruption of the BBB, alone or coupled with MFECD, may be a safe and effective method for increasing IONP delivery to the brain.

# Acknowledgements

First, I would like to express my sincere gratitude to my supervisor Dr. Donald W Miller for taking me in as his graduate student with my mediocre undergraduate GPA. It was through his understanding and kindness that I was encouraged to apply for graduate training. His patience, motivation, encouragement and immense knowledge continuously supported me during my Ph.D study. His guidance extended beyond research and writing of this thesis. I have learned not only how to do research but how to be a better person. I could not have imagined having a better advisor and mentor for my Ph.D study.

Besides my advisor, I would like to thank the rest of my thesis committee: Dr. Donald Smyth, Dr. Fiona Parkinson, and Dr. Torsten Hegmann for their insightful comments and encouragement, but also for the hard question which incented me to widen my research from various perspectives.

I thank Dr. Trosten Hegmann and his former group member Vinith Yathindranath and Matthew Warden for making different iron oxide nanoparticles. I extend my gratitude to Dr. Johan van Lierop and his group member Yaroslav Wroczynskyj and Palash K. Manna for their assistance in nanoparticle size and zeta potential characterization. I also like to thank Dr. James A. Thliveris for helping me fix and perfuse mice and taking beautiful TEM images. I thank Dr. Fiona Parkinson and her former student Steph Chu for isolating primary mouse neuron and astrocytes.

I thank Dr. Thomas Klonisch and Farhana Begum for slicing mouse brains and running H&E and immunofluorescence analysis. I extend my graduate to Dr. Dr. Tom Ward and Jannifer Bestland

for measuring Fe concentration by ICP analysis. I thank Dr. Dr. Emmanuel Ho and his student Yufei Chen and Sidi Yang for access and assistance with facilities in their labs. I thank Dr. Grant Hatch and his group member Marilyne Vandel and Edgar Majia for helping me with RT-PCR.

I thank my fellow labmates in for the stimulating discussions and for all the fun we have had. I extend my gratitude to Dr. Ngoc On for training me in mouse work. I thank Dr. Vinith Yathindranath for all his help with nanoparticles. I also like to thank Wei Xiong for helping me with western blot. My thanks goes to Marlyn Laksitorini, Eman Alraddadi, Michael Pogorzelec and Fang Chen for their help and support.

I thank Raquel Nowlin for booking my flight, claiming travel expense, and ordering. I thank Karen Donald for her help with administrative paper work and registration.

My studies at the University of Manitoba were supported by postgraduate scholarship from NSERC of Canada. Additional travel awards from Faculty of Graduate Studies, University of Manitoba, Canadian Society of Pharmacology and Therapeutics, and Globalization of Pharmaceutics Education Network are greatly appreciated. Financial support for the projects from the agencies including Paul H.T. Thorlakson Foundation Fund and NSERC-CIHR Collaborative Health Research Projects are greatly appreciated.

Last but not the least, I would like to thank my family: my parents, my wife and my daughter for your unconditional love and support.

# Dedication

***Dedicated to***

***my mother, my father, my wife and my daughter***

# Table of Content

# List of Tables

# List of Figures

# List of Copyrighted Materials

Figure 1.4 Effect of nanoparticles on lactate dehydrogenase (LDH) leakage (A) and ROS generation (B) in human cardiac microvascular endothelial cells after 24 hour incubation time. The respective metal nanoparticles had no surface coatings and thus represent the core metal oxide unit. Reproduced with permission from Sun et al. Cell Biol Toxicol. 2011 Oct;27(5):333-42. Copyright © Springer.

Figure 1.5 Prominent in vitro assays that are used to determine the impact of nanomaterials on cells; (b) TEM of HepG2 showing the mechanism of action of representative cell assays (i.e., MTT, checking mitochondria activity; PI, DNA staining; BrdU, DNA replication staining; LDH, membrane integrity assessment). Reproduced with permission from Mahmoudi et al. Chem Rev. 2012 Apr 11;112(4):2323-38. Copyright © American Chemical Society.

Figure 1.7 Cell fate of clathrin mediated endocytosis. Reproduced with permission from El-Sayed et al. Mol Ther. 2013 Jun;21(6):1118-30. Copyright © Nature Publishing Group.

Figure 1.8 Schematic overview of macropinocytosis and inhibitors. Reproduced with permission from El-Sayed et al. Mol Ther. 2013 Jun;21(6):1118-30. Copyright © Nature Publishing Group.

Figure 1.9 Choroid plexuses and blood-CSF barrier. (A) The choroid plexuses are present in the two lateral, third and fourth ventricles (red ribbons). (B) Each of the plexuses is comprised of fenestrated vessels, with a single layer of intimately opposed choroid epithelial cells, joined by tight junctions—forming the blood-CSF barrier. CPEC: choroid plexus epithelial cells. Blood-CSF barrier: blood-cerebrospinal fluid barrier. Reproduced with permission from Liddelow SA. Front Neurosci. 2015 Mar 3;9:32. Copyright © Liddelow

Figure 1.10 Anatomical structure of the BBB. Reproduced with permission from Abbott NJ. J Inherit Metab Dis. 2013 May;36(3):437-49. Copyright © Springer.

Figure 1.11 Tight junction structures. Reproduced with permission from Tajes et al. Mol Membr Biol. 2014 Aug;31(5):152-67. Copyright © Informa Healthcare.

**Chapter 2** Characterization of cellular uptake and toxicity of aminosilane-coated iron oxide nanoparticles with different charges in central nervous system-relevant cell culture models Reproduced with permission from Sun et al. Copyright © Dove Medical Press.

Sun, Z., Yathindranath, V., Worden, M., Thliveris, J. A., Chu, S., Parkinson, F. E., … Miller, D. W. (2013). Characterization of cellular uptake and toxicity of aminosilane-coated iron oxide nanoparticles with different charges in central nervous system-relevant cell culture models. International Journal of Nanomedicine, 8, 961–970. http://doi.org/10.2147/IJN.S39048

**Chapter 3** Magnetic field enhanced convective diffusion (MFECD) of iron oxide nanoparticles in an osmotically disrupted cell culture model of the blood-brain barrier. Reproduced with permission from Sun et al. Copyright © Dove Medical Press.

Sun, Z., Worden, M., Wroczynskyj, Y., Yathindranath, V., van Lierop, J., Hegmann, T., & Miller, D. W. (2014). Magnetic field enhanced convective diffusion of iron oxide nanoparticles in an osmotically disrupted cell culture model of the blood–brain barrier. International Journal of Nanomedicine, 9, 3013–3026. http://doi.org/10.2147/IJN.S62260

# List of Abbreviations and Symbols

| | |
|---|---|
| ABC | ATP-binding cassette |
| APTES | 3-Aminopropyltriethoxysilane |
| AR | Aspect ratio |
| ATP | Adenosine triphosphate |
| BBB | Blood-Brain Barrier |
| BCRP | Breast Cancer-Resistance Protein |
| bEnd.3 | Mouse brain endothelial cell line |
| bFGF | Basic fibroblast growth factor |
| BrdU | Bromodeoxyuridine |
| BSA | Bovine serum albumin |
| Caco2 | Caucasian colon adenocarcinoma cell line |
| CED | Convection-enhanced delivery |
| CNS | Central Nervous System |
| CSF | Cerebrospinal fluid |
| CTB | Cholera toxin B |
| DLS | Dynamic Light Scattering |
| DMEM | Dulbecco's Modified Eagle's Medium |
| DMSA | Dimercaptosuccinate |
| DMSO | Dimethyl Sulfoxide |
| ECM | Extracellular matrix |
| EPR | Enhanced Permeability and Retention |
| FBS | Fetal Bovine Serum |

| | |
|---|---|
| FDA | Food and Drug Administration (USA) |
| FDX | Fluorescein labeled dextran |
| FITC | Flourescein isothiocyanate |
| FTIR | Fourier transform infrared spectroscopy |
| GDNF | Glial-derived neurotrophic factor |
| GFAP | Glial Fibrillary Acidic Protein |
| GPCR | G-Protein Coupled Receptor |
| GPI | glycosylphosphatidylinositol |
| H & E | Hematoxylin and Eosin |
| HeLa | Human cervix epithelial adenocarcinoma cell line |
| HepG2 | Human liver hepatocellular cell line |
| HER2 | Human epidermal growth factor receptor 2 |
| IL | Interleukin |
| IONPs | Iron oxide nanoparticles |
| JAM | Junctional adhesion molecule |
| KB | Oral squamous carcinoma cell line |
| LDH | Lactate dehydrogenase |
| LPA | Lysophosphatidic Acid |
| LPAR | Lysophosphatidic Acid Receptors |
| MDCK | Madin-Darby Canine Kidney Epithelial Cells |
| MFECD | Magnetic Field Enhanced Convective Diffusion |
| MIONs | Magnetic iron oxide NPs |
| MRI | Magnetic Resonance Imaging |

| | |
|---|---|
| MTT | 3-(4,5-dimethylthiazol-2-yl)-2,5-diphenyltetrazolium bromide |
| MWCO | Molecular weight cut off |
| NPs | Nanoparticles |
| PAA | Poly(acrylic acid) |
| PBS | Phosphate buffered saline |
| PCS | Photon correlation spectroscopy |
| PECAM | Platelet endothelial cell adhesion molecule |
| PEG | Poly(ethylene) glycol |
| PEI | Polyethyleneimine |
| PI | Propidium iodide |
| PLGA | Poly(lactic-co-glycolic acid) |
| RES | Reticuloendothelial system |
| ROS | Reactive oxygen species |
| siRNA | Small interfering RNA |
| SPIONs | Superparamagnetic iron oxide NPs |
| TEER | Transepithelial electric resistance |
| TEM | Transmission electron microscopy |
| TGA | Thermogravimetric analysis |
| TGF-β | Transforming growth factor-β |
| TNF-α | Tumor necrosis factor alpha |
| USPIONs | Ultrasmall superparamagnetic iron oxide NPs |
| XRD | Powder X-ray Diffraction |
| ZO | zonula occludens protein |

# Chapter 1 : Introduction to Iron Oxide Nanoparticles (IONPs) as a Drug Delivery Platform Targeting the Brain

# 1.1 Introduction

Nanoparticles (NPs) generally refer to synthetically engineered materials that are 1 to 100 nm in diameter in at least one dimension. Human use of nano-sized materials can be traced back thousands of years where lead based nanocosmetic preparations were used by ancient Egyptians and nanocrystal-containing hair dye formulations were used by Greeks and Romans[1]. Although NPs have been used several millennia ago, the idea of nanotechnology was introduced in 1953 by Richard Feynman, a physicist at Cal Tech. His talk entitled "There's Plenty of Room at the Bottom" has been considered the first to deal with materials at the level of atoms and molecules[2]. The discovery and understanding of unique properties of nanoparticles has been growing significantly since. Figure 1 shows the number of publications in PubMed with title or abstract containing "nanoparticles" in each year. In 2014, the number of publications related to nanoparticles was 6 times more than 10 years ago. Indeed, the field of nanotechnology has rapidly expanded to various biomedical applications such as drug delivery, cancer hyperthermia, imaging applications, and cell tracking and migration.

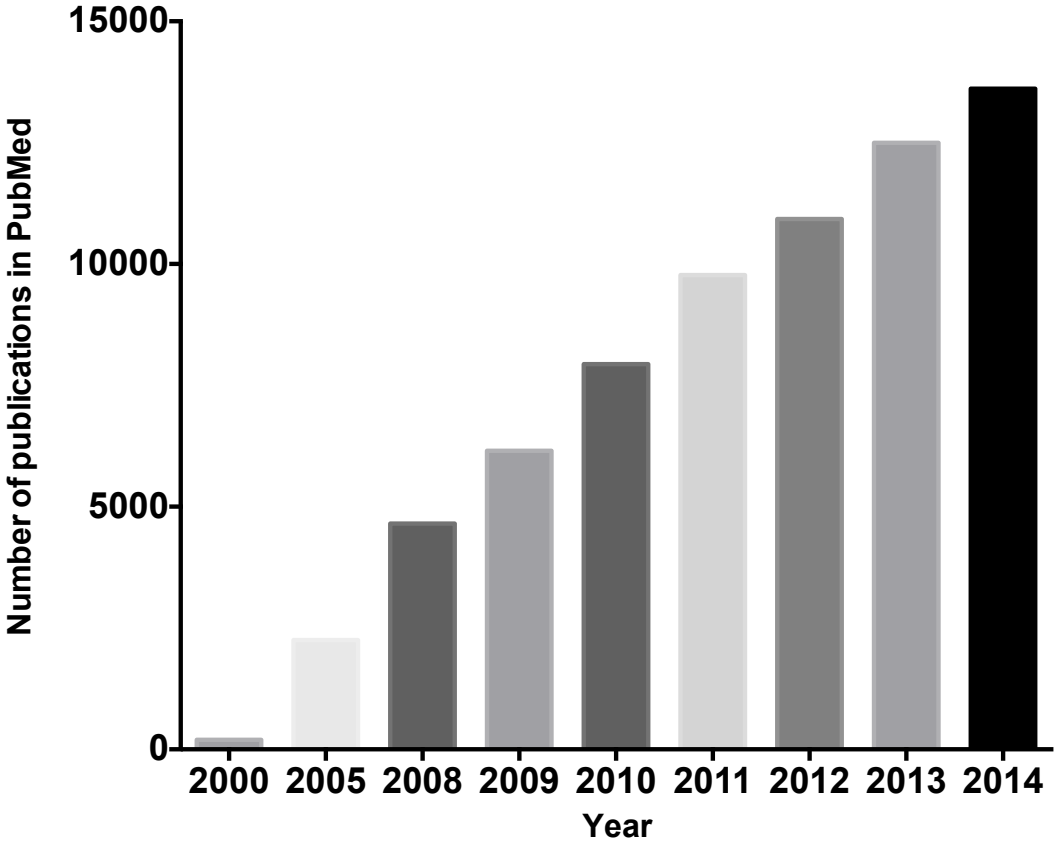


**Figure 1.1 Number of scientific studies published in PubMed with title or abstract containing "nanoparticles" in recent years.**

### 1.1.1 Iron oxide nanoparticles (IONPs)

Iron oxide nanoparticles (IONPs) generally refer to NPs with a core made of γ-$Fe_2O_3$ (maghemite) or $Fe_3O_4$ (magnetite). IONPs are biocompatible and possess magnetic moment potentially suitable for MRI or magnetic enhanced drug targeting. IONPs administered to humans can be incorporated into natural iron metabolism pathways and biological process such as hemoglobin synthesis. IONPs can be metabolized, stored and transported by proteins including ferritin, and transferrin. The metabolized iron is incorporated into the iron pool in the body. Moreover, it is easy to graft various ligands, dyes, proteins, antibodies, and polymers onto IONPs. These characteristics make IONPs promising candidates for biomedical applications. To

increase magnetic susceptibility, other metals such as manganese or cobalt (e.g., $MnFe_2O_4$, FeCo and $CoFe_2O_4$) can be incorporated into IONPs. However, these IONPs are much less common in biomedical application mainly due to rapid oxidization and toxicity related issues[3,4]. Most of the IONPs in the literature are magnetite or maghemite due to their excellent chemical stability and biocompatibility. Depending on the publication, magnetite and maghemite NPs may also be referred to as SPIONs (superparamagnetic iron oxide NPs), USPIONs (ultrasmall superparamagnetic iron oxide NPs), or MIONs (magnetic iron oxide NPs).

IONPs are composed of domains each containing large numbers of atoms. A micron sized iron oxide is composed of many domains. When particle size is reduced to less than 50nm, the particle is said to have a single domain[5]. In absence of magnetic field, the magnetic moment of the domain is randomly oriented giving a zero magnetic moment of the material. In contrast, when IONPs are placed in a magnetic field, the magnetic moment in each domain aligns with the applied magnetic field and IONPs become magnetized to their saturation magnetization. Upon removal of magnetic field, no residual magnetic moment is present and IONPs become randomly oriented again. This unique property of being magnetic when in an external magnetic field and displaying no magnetic properties when the external magnetic field is removed is termed "superparamagnetic". This feature is crucial for biomedical applications as they have the ability to form stable colloidal suspensions. Furthermore, the superparamagnetic properties of IONPs provide the additional advantages of being traceable within the body, using magnetic resonance imaging (MRI), as well as being targetable to selected tissues with application of magnetic fields. The latter property is of particular interest to overcome obstacles such as non-specific toxicity due to general systematic distribution of nanoparticles as well as poor therapeutic effect due to sub-therapeutic concentrations at target site.

### 1.1.2 Agglomeration of IONPs and Ways to Overcome the Problem

Agglomeration of IONPs occurs when two or more particle surfaces come in contact with each other and thermodynamically favor particle–particle interaction. Generally speaking, the smaller the NPs, the higher the tendency to agglomerate. As NPs get smaller, the surface energy increases and agglomeration is thermodynamically favored to reduce the free energy in the system[6]. Uncoated IONPs are particularly susceptible to agglomeration when placed in an aqueous environment. The agglomeration problems observed with uncoated IONPs are emphasized in the presence of an external magnetic field[7]. Surface coating of the NPs has been used to overcome the problem of agglomeration by enhancing electrostatic, steric, or electrostatic repulsive forces between NPs. Figure 1.2 demonstrates the increased colloidal stability provided to IONPs by coating with negative or positively charged coatings. The electrostatic repulsion keeps charged IONPs from agglomeration. Uncoated IONPs quickly settled down to the bottom of the vial, as the increase in size and Brownian motion can no longer keep them suspended in water. Other factors influencing agglomeration include, ionic strength in solution, concentration of NPs, temperature, and gravitational force[6].

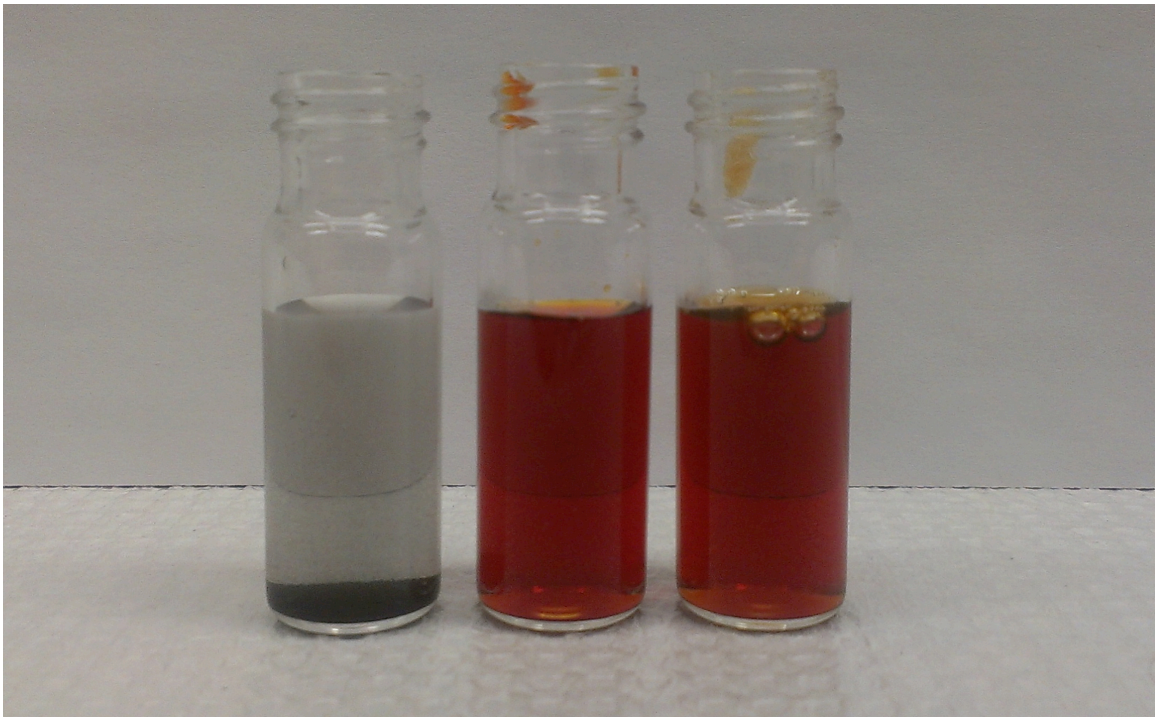

**Figure 1.2 Uncoated (left), positively charged (middle) and negatively charged IONPs suspension in water after 2 hour of settling time.**

### 1.1.3 Protein Corona

When exposed to biological fluid, various proteins and biomolecules may adhere onto the surface of the IONPs to form a protein corona. The protein corona generally consists of two layers. The first protein layer that interacts directly with the nanomaterial surface and is tightly attached to the surface via hydrogen bonds, solvation forces, electrostatic and hydrophobic interactions is called the "hard corona". A secondary protein layer, the so called "soft corona" interacts with the proteins forming the hard corona via weak protein-protein interaction[8]. The soft corona undergoes rapid exchange with surrounding proteins responding dynamically to its environment compared to hard corona that has a slow protein exchange rate. The formation of a protein corona depends on the physiochemical characteristic of IONPs surface as well as the proteins present in the media[8]. A recent publication investigated the effect

of temperature on the composition of protein corona and the affinity of various proteins to the surface of NPs to demonstrate change of body temperature can also affect protein corona formation[9].

A common method for analyzing the protein-NP complex is to expose the NPs to the biological sample and then isolate the protein-NP complex by centrifugation. However, with this method, many proteins can be false-positively identified as bound to NP surface due to insufficient washing. Sakulkhu et al., 2014 developed magnetic separation method to remove IONP-attached protein coronas[10]. Besides common drawback on separation methods, contribution of various proteins on IONP surface is still questionable. Different association/dissociation rates, and variation in amounts and types of protein available in the cells or tissues to complex with IONPs play essential roles in determining the impact of the protein corona on the biological fate of the IONPs[11]. For example, opsonin interaction with IONPs will lead to elimination by macrophages resulting in reduced plasma half-lives, whereas albumin interaction with IONPs might lead to prolonged circulation time. However, due to difficulties in acquiring a comprehensive understanding of the corona, the dynamic nature and dependence of corona when interacting with cell or tissue is not clearly elucidated. The general understanding is that the soft corona contributes more to the circulation half life of IONPs while the hard corona contributes more to cellular interaction / uptake.

Surface coating can influence formation of a protein corona. For example, multiphosphonic acid polyethylene glycol (PEG) copolymer coating of IONPs provide long term stability in culture media and prevent protein corona formation[12]. Surface modification of IONPs play an essential role in determining the amount and types of protein absorbed. For example, there is a significantly lower amount of proteins in the hard coronas of positively charged

dextran IONPs compared to negatively charged dextran IONPs[13]. Calatayud et al., 2014 reported the formation of large protein-MNP aggregates (1-3 μm) with a negative surface charge within 4 hours, irrespective of the MNP-core charge In contrast, positively charged polyethyleneimine (PEI) coated IONPs favor uptake in neuroblastoma cells compared to negatively charged poly(acrylic acid) (PAA) coated NPs in 15 and 72 hour of incubation time[14]. This finding is consistent with our observations of positive charged IONPs. Figure 1.3 shows the effects of surface charge on corona formation. Two IONP formulations displaying opposing surface charges in water have similar charges when in culture media containing proteins (Figure 1.3). These observations together seem to suggest protein corona composition alters the size, surface charge and interactions between cell and IONPs.

Protein corona composition can be influenced by size of IONPs. This was demonstrated by the studies of Ashby et al., 2014[11]. Keeping the surface ligand coating the same, authors showed that increasing the size of IONPs resulted in a more dynamic protein corona with a larger portion of the involved proteins with fast exchange rates[11]. A recent study reported that protein with low molecular weight would preferentially bind to small IONPs; whereas the protein with large molecular weight would mostly interact with large IONPs even though the composition and concentration of protein corona were random[15]. Based on the above observations regarding IONP size and resulting protein corona, small nanoparticles with diameters between 20 and 50nm appear to provide the least amount of tissue accumulation and longest circulating half-life.

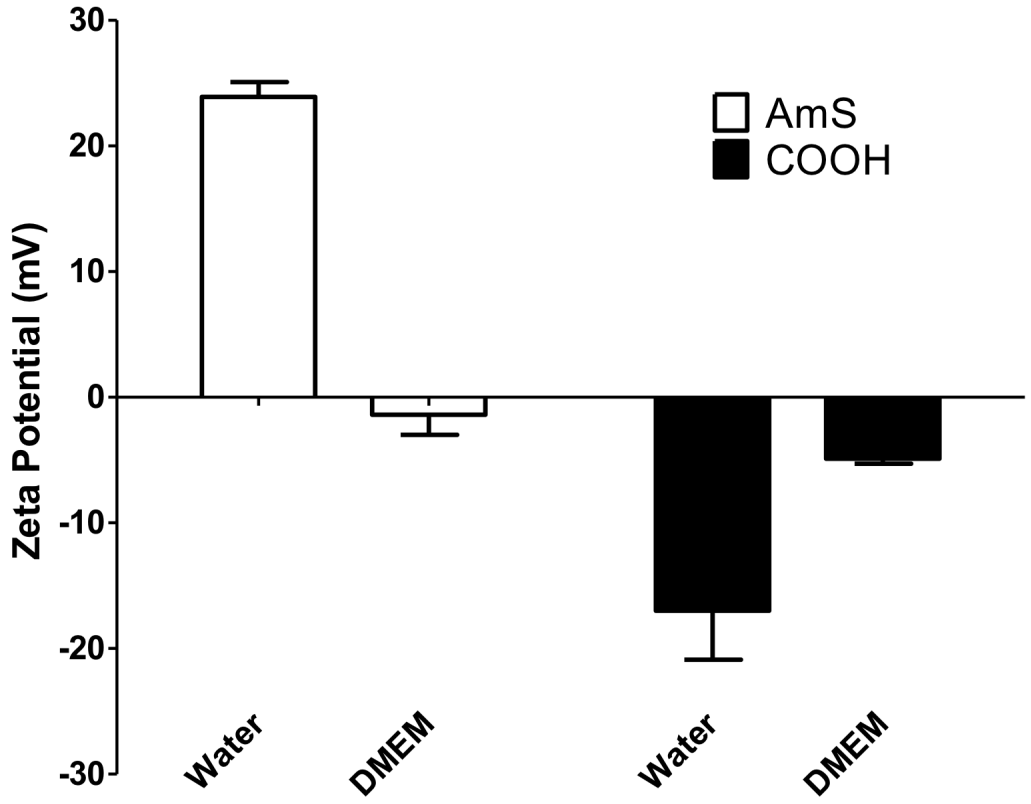


**Figure 1.3 Effect of DMEM media with 10% FBS on zeta potential measurement of positively charged aminosilane (AmS) coated and negatively charged carboxylic acid (COOH) coated IONPs.**

## 1.1.4 Biocompatibility of IONPs

IONPs are generally considered biocompatible with the iron from the NPs being incorporated into iron metabolism pathway[16]. The breakdown of IONPs most likely occurs in the lysosome of cells[17]. The free iron ion in the lysosome is then transferred to the intracellular iron metabolic pool by divalent metal transporter 1 present on the lysosomal membrane[18]. As free, unbound iron in the cell is tightly regulated, the added iron entering into the cellular pool is accompanied by an increased expression of the iron storage protein, ferritin[19]. Evidence that IONPs are metabolized in the manner described above are the reports of increased cellular iron content following exposure to IONPs and the associated robust up-regulation of ferritin[20]. This

phenomenon has been observed in many different cells including oligodendrocyte cells[21], macrophages[22], and astrocytes[23]. Free iron ion can be transported out of the cell by ferroportin protein on the plasma membrane[24].

Although IONPs are generally considered biocompatible, cellular toxicity has been reported with regard to production of reactive oxygen species (ROS) such as hydrogen peroxide, hydroxyl radicals, and superoxide anion by Fenton and/or Haber–Weiss reactions[25]. Elevated ROS within the cell can lead to oxidative stress that is associated with the onset and/or progression of a variety of pathological conditions such as neurodegenerative disease, inflammation, cardiovascular disease, and cancer. The detrimental effects of ROS within the cell are multi-centered with alterations in cell membrane leading to the generation of lipid peroxidation products, disruption of DNA, altered protein expression and interrupted mitochondrial respiration[26]. Several lines of evidence suggest that maghemite NPs induce a higher level of reactive oxygen species, proinflammatory cytokines and autophagosome-like vacuoles than magnetite[27-29]. However, oxidative toxicity has also been reported for magnetite species of IONPs[30]. Nonetheless, compared to other metal oxide nanoparticles, IONPs appear to have the least toxicity[31-34]. This is illustrated in Figure 1.4 showing the effect of different metal oxide nanoparticles on lactate dehydrogenase (LDH) leakage and ROS generation in human cardiac microvascular endothelial cells. In the cultured endothelial cell preparation, neither $Fe_2O_3$ nor $Fe_3O_4$ NPs displayed significant effects on cytotoxicity and ROS production at concentration up to 100μg/mL while ZnO, CuO, and MgO NPs produced cytotoxicity in both a concentration and time-dependent manner.

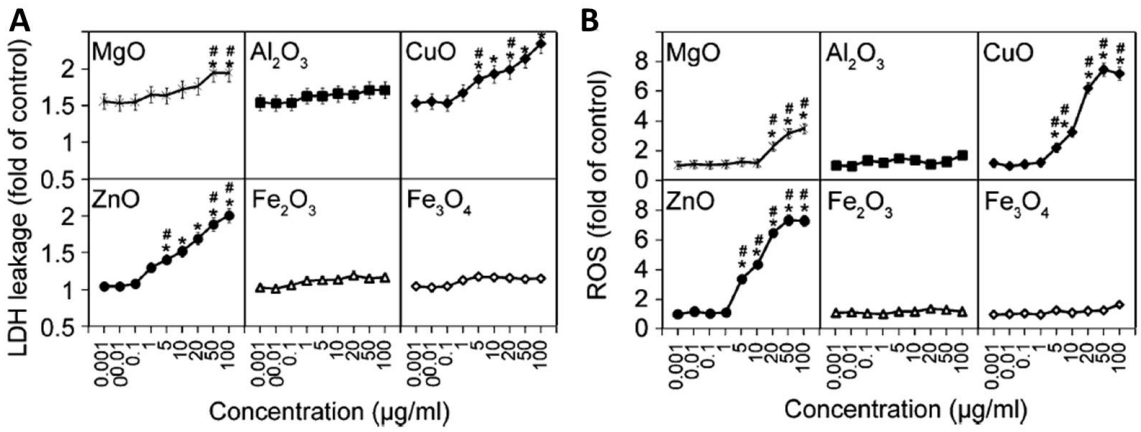


**Figure 1.4 Effect of nanoparticles on lactate dehydrogenase (LDH) leakage (A) and ROS generation (B) in human cardiac microvascular endothelial cells after 24 hour incubation time. The respective metal nanoparticles had no surface coatings and thus represent the core metal oxide unit. Reproduced with permission from Sun et al. Cell Biol Toxicol. 2011 Oct;27(5):333-42. Copyright © Springer.**

Because ROS were generated from the core of the IONPs, coating the IONPs surface with a more biocompatible shell can minimize potential toxicity. IONPs can be coated with organic (e.g. dextran, chitosan, and polymers) or inorganic materials (e.g. gold and silica) thereby shielding the IONP core from interaction with biological matrices such as cells and tissues. Because of this it is important when discussing the biocompatibility of IONPs to note the specific surface coating applied. Studies have shown uncoated IONPs at both 5 and 30nm diameter induced a 6 fold increase cellular toxicity and ROS production compared to IONPs coated with dextran, or PEG in endothelial cells[35]. It has been confirmed that dextran or PEG coated IONPs did not increase intracellular ROS production compared to uncoated IONPs. The level of inflammatory cytokines such as Tumor necrosis factor alpha (TNF-α) and interleukins IL-6, IL-8, and IL-1β were also not changed compared to control[36]. Such findings are not confined to the cell culture setting as *in vivo* studies in mice reported no genotoxicity with silica coated IONPs[37]. Another recent study investigated biodistribution and toxicokinetics of different sized (from 10nm to 40nm) carboxyl coated IONPs in mice. Hematological analyses and

histological examination demonstrated that there was no apparent acute toxicity caused by intravenous administration of IONPs although genes related to oxidant stress, iron transport, metabolic processes were altered[38]. It should be noted that not all coatings result in reduced toxicity. Oleate-coated IONPs induce cytotoxicity in a dose-dependent manner in human lymphoblastoid cells[39]. Positively charged polycationic IONPs may lead to increased cytotoxic effect and ROS production compared to negative or neutral IONPs[40]. These studies suggest that hydrophilic surface coating can reduce toxicity whereas hydrophobic coating increase toxicity.

The *in vitro* assessment of toxicity of many IONPs has been limited to simple proliferation assays such as MTT or LDH assay. This is understandable, as the MTT and LDH assays provide an inexpensive, quick and quantitative assessment of toxicity. However, as they only examine toxicity in the form of cell death, these assays may miss more subtle cellular responses to the IONPs. Because of this, assays for inflammatory stress, oxidative stress, and genotoxicity have gained interest for determining the biocompatibility of IONPs. Figure 1.5 summarizes the various *in vitro* assays that have been used to probe the potential toxicity of IONPs. It has been reported that IONPs with different surface charges and sizes induced no significant reduction in cell viability as measured by LDH assay; however, genotoxicity assay results revealed potential DNA damage at concentration higher than 200 μg/mL regardless of the charge and size[41]. Authors also indicated that the high cellular uptake profiles are directly correlated with increased toxicity. Di Bona et al., 2014 examined the effect of IONPs with positive or negative surface charges on toxicity and biodistribution in pregnant mice. The results indicated the positively charged PEI coated IONPs with a high tissue uptake profile significantly decreased maternal weight gain, crossed the placenta and accumulated in the fetal liver[42]. Thus

coatings that restrict or limit uptake (i.e. dextran, carboxylic acid) will have reduced toxicity, while coatings that enhance uptake (i.e. oleic acid, PEI) will display increased toxicity.

Often *in vitro* toxicity screening will be conducted first. If the IONPs pass the *in vitro* toxicity assays, then *in vivo* assay can be carried out on a relevant animal model. However, because different research groups utilize different assay parameters such as cell types, cell culture growth conditions, dosing regimen of IONPs, it is quite difficult to obtain consistent data on the toxicity of IONPs to allow for comparison across the different studies[5]. Furthermore, the different coating and physiochemical properties (size, colloidal stability) of IONPs add another layer of complexity to the big picture of determining IONPs biocompatibility. Many of the IONPs used in toxicity reports are poorly characterized with issues of aggregation, and unclear coating procedures (i.e. covalently attached or non-covalently absorbed onto IONPs). For example, in a study conducted by Guadagnini and coworkers, several of the IONP formulations displayed bimodal distribution of hydrodynamic size, as determined by dynamic light scattering (DLS)[43]. This is a clear sign of agglomeration and low colloidal stability. For this reason, these particular IONPs should not be used in biomedical applications as they are too heterogenous and potential toxicity related with agglomerated IONPs does not necessarily carry over to the individual IONPs. Moreover, other reports suggest coating of IONPs with a biocompatible compound, sodium oleate increased toxicity. If the coating was simply absorbed onto the IONPs by sonication, it is likely that free oleic acid is also present during the IONPs incubation with cells. If the coating were covalently attached onto the IONPs, the IONPs would be hydrophobic with high uptake profile, which in turn leads to toxicity. There is an urgent need not only for standardizing various *in vitro* and *in vivo* toxicity assays, but also applying these assays to well-characterized, highly colloidal stable, and pure IONPs. For this, a good understanding of the

physiochemical properties of IONPs to be used is necessary for studying their biological behavior.

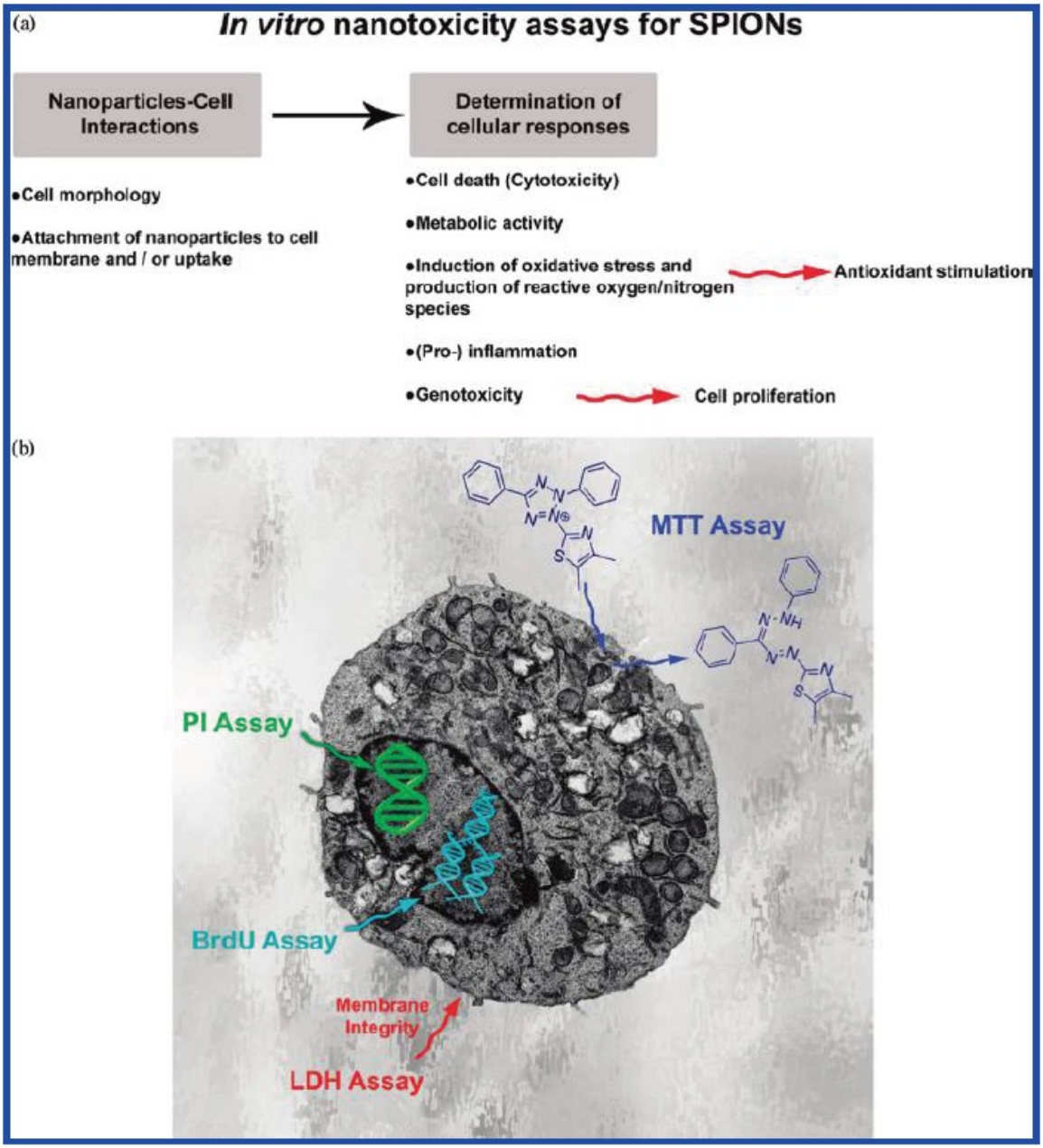


**Figure 1.5 Prominent in vitro assays that are used to determine the impact of nanomaterials on cells; (b) TEM of HepG2 showing the mechanism of action of representative cell assays (i.e., MTT, checking mitochondria activity; PI, DNA staining; BrdU, DNA replication staining; LDH, membrane integrity assessment). Reproduced with permission from Mahmoudi et al. Chem Rev. 2012 Apr 11;112(4):2323-38. Copyright © American Chemical Society.**

## 1.2 Importance of Physiochemical Properties of IONPs

To develop a successful drug delivery platform, the physiochemical properties of IONPs such as size, shape, and surface coating play a pivotal role in determining the behavior in a biological system (cellular internalization and pharmacokinetic properties).

### 1.2.1 Size

The size of IONPs can be determined by two different methods: Transmission electron microscopy (TEM) or DLS. The size determined by TEM represents the size of iron oxide core; whereas the size determined by DLS represents the hydrodynamic size of the IONPs. The DLS estimate the hydrated NPs in Brownian motion suspended in an aqueous solution based on scattered light intensities. Of note, DLS assume that the NPs are spherical. Ambiguous results may be obtained when measuring non-spherical NPs using DLS. When protein corona is present, DLS will capture the size of NPs-protein corona complex. This leads to an increase in size measurement of NPs dispersed in media compared to ones dispersed in water. When protein is present in solution, the size measured by DLS depends on the types and amount of proteins present. Therefore, when reporting the hydrodynamic size of NPs, it is assumed that the measurement was performed in water unless indicated otherwise.

There is a clear size dependent uptake of IONPs *in vitro*. The uptake profile of various different sized (26, 53, 76 and 98 nm) IONPs with positive charge was studied with Caucasian colon adenocarcinoma cell line (Caco2). The large IONPs (76 and 98 nm) exhibited a higher uptake rate compared to small IONPs (26 and 53 nm)[44]. A size-dependent effect has also been reported in macrophages. In these studies, a library of PEGylated IONPs, spanning a range of 30–100 nm in diameter were synthesized and their internalization rate in macrophages were

determined *in vitro*. As observed in the Caco-2 cells, as the size of IONPs increased, the non-specific uptake of IONPs also increased[45].

The size of IONPs not only affect cellular uptake but also influence their biodistribution *in vivo*. Yang et al., 2015 recently have shown that small IONPs (10nm) accumulate more in the liver whereas the large IONPs (40nm) accumulate more in the spleen[38]. The plasma half-life of IONPs was found to be dependent on their size, with an inverse correlation between size of IONPs and plasma half-life. The half-life of 20nm carboxydextran coated was 49 minutes while the 50nm IONPs with identical coating had a plasma half-life of 5 minutes[46]. The reduced half-life observed with IONPs of increasing size appears to be attributable to increased macrophage clearance of large IONPs[46].

The size of IONPs plays an important role in selective tumor cell accumulation. Due to poor perfusion, poor lymphatic drainage, heterogeneity and leakiness of the tumor vasculature, an increased accumulation of macromolecules in solid tumor including primary and metastatic tumor were observed. This phenomenon was called enhanced permeability and retention (EPR) effect[47]. The EPR effect is also apparent in the increased tumor permeability reported for various types of NPs[48]. It is speculated that the small IONPs can re-enter the blood stream after tumor extravasation resulting in reduced amounts retained within the tumor, while the larger IONPs are trapped within the tumor site. In contrast to these studies, IONPs targeting human epidermal growth factor receptor 2 (HER2) receptor show increased tumor tissue accumulation for 30 nm compared to 100 nm IONPs in a tumor xenograft mouse model[49]. Such apparent discrepancy may be explained by the presence of targeting ligand on the surface of IONPs. The smaller size IONPs may be advantageous with regards to ligand directed tumor penetration.

There are several MRI imaging studies investigating the effect of size on the lymphatic distribution of IONPs. Injection of IONPs with size ranging from 50 to 1000 nm into footpad of mice and sequential MRI imaging of popliteal and inguinal lymph nodes revealed IONPs less than 100 nm can be used to visualize the lymphatic structure by crossing lymphatic walls. In contrast, IONPs larger than 200nm were quickly phagocytized by macrophages and resulted in poor imaging of lymphatics[50]. Another study utilized IONPs up to 20 nm in diameter and suggested 20nm diameter IONPs were best for lymph node detection[51]. In these studies, 15, 27 and 58 nm diameter PEGlyated IONPs were examined for their uptake in sentinel lymph nodes. These studies reported that the 15nm diameter IONPs accumulated the most quickly and to the greatest extent in sentinel lymph nodes compared to the other larger sized IONPs[51]. However, another study performed by Pouw et al., 2015 examined the effect of dextran-coated IONPs of different size (32, 59, and 111 nm diameter) as tracers for sentinel lymph node biopsy within an *in vivo* porcine model. In these studies, the 59 nm diameter IONPs resulted in a significantly higher lymph node accumulation compared to the 32 nm diameter IONPs. Interestingly the largest IONPs examined (111 nm diameter) were detected in lymph nodes, although the time required was significantly longer (i.e. 4 hours). The extended time required for lymph node distribution suggests that these particles may be taken up by macrophages and as such more likely to image the higher echelon nodes beyond the sentinel lymph node[52]. While these studies provide insight into the influence of size on cell and tissue distribution of IONPs, caution should be taken as the coating of the IONPs will also have an impact and may explain some of the discrepancies in the literature.

### 1.2.2 Surface Coating

Surface coatings of IONPs are necessary to increase colloidal stability, to allow complexation with a drug payload, and to establish a multifunctional drug delivery system. More importantly, the biological properties of IONPs are predominately determined by their surface coating. This section will discuss the effect of surface coating on cellular uptake of IONPs.

The effect of surface charge has been extensively studied. Several lines of evidence suggest that positively charged IONPs show a higher cellular uptake profile compared to negatively charged IONPs. For example, compared to bare, dextran coated, and silica coated IONPs, aminosilane coated IONPs exhibited the highest cellular uptake efficiency in various macrophage, fibroblast, cancer and epithelial cell lines[53]. In the human oral squamous carcinoma cell line (KB), the cellular uptake of positively charged chitosan coated IONPs were higher than negatively charged dimercaptosuccinic acid coated IONPs[54]. Similar studies also confirmed that IONPs with neutral surface charge were not internalized into the human cervical epithelial adenocarcinoma cell line (HeLa); negatively charged IONPs show low cellular uptake with non-toxic effects; and positively charged IONPs show effective internalization in the endosome without any cytotoxicity[55]. The electrostatic interaction between the positively charged NPs and the negatively charged glycocalix certainly favors fast attachment to the cell membrane and subsequent internalization of cationic species[56]. However, some studies have reported increased cellular uptake with negatively charged IONPs. For example, the uptake of IONPs coated with varying amounts of carboxymethyl dextran and thus varying surfaces charges was evaluated in Caco2 cells. Increased uptake of nanoparticles with greater negative charge was observed. Mechanistic studies suggest that uptake of the most negatively charged particles occurs via macropinocytosis[57]. Another study compared cellular uptake of 28 and 74 nm alkali-treated dextran coated IONPs (-15mV zeta potential), to carboxymethyl dextran IONPs (-24mV zeta

potential) of similar size in a macrophage cell line, RAW264. No significant difference was found in the cellular accumulation of the large (74 nm diameter) and small (28 nm diameter) IONPs of the same coating. In contrast, carboxymethyl dextran IONPs show significantly greater cell labeling than alkali-treated dextran coated counterparts[58]. This study suggested surface coating is a more important factor than size with regard to uptake in macrophage. More importantly, macrophage, specialized in phagocytosis, can take up either charged IONPs to a great extent.

To improve the targeting efficiency, various ligands are often grafted onto the surface of the IONPs. However, the relationship between the density of ligands and targeting efficiency is not linear and varies depending on both the IONPs and targeting ligand. Comparing the influence of ligand grafting density (6 -36 ligands per IONP), Elias and colleagues showed optimal binding and targeting to cells with IONPs having an intermediate ligand grafting density (11 and 23 ligands per IONP)[59]. The optimized number of ligands per IONP is dependent on the size of IONP as well as types of targeting ligand. Other factors such as ligand orientation, receptor mobility and receptor internalization can also influence the targeting efficiency[59]. Targeting efficiency can also be optimized by alternative variant antibody against target of interest. Fiandra and colleagues assessed tumor-targeting efficiency against HER2 *in vitro* and *in vivo* of IONPs coated with trastuzumab, or lower molecular weight variants of the half-chain and scFv fragments of the antibody. They found that IONPs coated with half-chain antibody were the best candidates owing to their increased affinity to HER2 positive cells and tumor homing ability[60].

### 1.2.3 Shape

There are few reports regarding the biological properties of non-spherical IONPs. Examination of the nanoparticle literature show only limited reports where a side-by-side comparison of how non-spherical nanoparticles and their spherical counter parts interact with biological milieu. These relatively limited studies are highlight below to provide an assessment of the effect of NP shape on biological response.

Chauhan and colleague have studied the effect of nanoparticles shape on tumor penetration[61]. In this study, colloidal quantum dot-based nanospheres and nanorods were designed to have tunable size but identical surface PEG coating and charge. The size of nanorods was measured to be 15 nm diameter and 54 nm length while hydrodynamic size of nanosphere was 35nm. Thus these studies provide an assessment of the general uptake and tissue distribution properties of a non-targeted NP. The nanorods had significantly better permeability across semi-permeable membrane and higher tumor penetration compared to the nanospheres. Such improved transport rate into tumor might be attributed to reduced steric hindrance near the pore walls[61].

Antibodies have been commonly grafted either chemically or physically onto the surface of the nanoparticles for active targeting or therapeutic applications in various disease models including cancer. Recently, it has been reported that nanoparticles shape affects the avidity and specificity of antibodies attached on the surface for their cellular targets. Barua et al., 2013 investigated the effect of polystyrene particles of different shape (ie. spheres, rods, and disks) for cell targeting and therapeutic efficacy of trastuzumab, a human epidermal growth factor receptor2 (HER2) monoclonal antibody in different breast cancer cell lines[62]. Trastuzumab coating significantly enhanced uptake of both the nanorod and nanodisk in HER2+ breast cancer cells compared to nanosphere counterparts. However, trastuzumab coated nanorods exhibited the highest uptake profile in both HER2+ breast cancer cell line BT-474 and SK-BR-3. Pretreatment

of the cells with free trastuzumab reduced the uptake profile of the trastuzumab coated nanorod, suggesting a specific targeted uptake role for trastuzumab. Furthermore, the shape enhanced nanoparticle uptake was more prominent in larger size (1μm) compared to smaller nanoparticles (200nm). The authors elegantly demonstrated that such enhanced uptake of nanorod over nanosphere is due to enhanced binding of trastuzumab coated nanorods to the cell membrane receptor over their nanosphere counterparts. Most importantly, there was a significant enhancement of therapeutic effect of the trastuzumab-coated nanorods compared to either trastuzumab alone or trastuzumab labeled nanospheres.

In accordance with this study, shape-dependent adhesion kinetics of non-spherical nanoparticles under shear flow using a Brownian motion dynamics computational model was examined[63]. Spherical particles with 380nm size and rod shaped nanoparticles with 1000nm length and aspect ratio of 5 were considered in this study. Nanorods were predicted to contact and adhere to the vascular bed much easier than their spherical counterparts under shear rate of 8/s due to their tumbling motion. Furthermore, nanorods have higher binding probability compared to nanospheres at the same shear rate. As the shear rate increases, there is a larger difference in adhesion probability between nanorods and nanospheres. These studies collectively contribute understanding of how particle shape affects the transport and targeting efficiency of nanocarriers. The development of shape specific nanomedicine is a very promising approach for targeted drug delivery applications.

Besides shape-dependent differences in nanoparticle uptake and cell association, nanoparticles shape can also influence cell function such as cell adhesion and migration. This is illustrated in studies using mesoporous silica nanoparticles with aspect ratios (ARs) (the ratio of the width to the height) of 1 (sphere), 2 (short rod), and 4 (long rod)[64]. A decreased expression of

important adhesion molecules such as ICAM-1 and MCAM-1 was observed upon treatment of NPs, leading to diminished cell adhesion ability and altered cell proliferation and homeostasis[64]. NPs with larger ARs had a greater effect on cellular function including cell proliferation, cytoskeleton formation, adhesion and migration[64]. This study suggests that different shaped NPs can mediate biological effect in addition as a drug carrier.

The shape of NPs can affect their *in vivo* biodistribution and clearance. It has been shown that rod shaped PEGylated gold NPs have higher circulation half-life and higher level of accumulation in tumor compared to spherical shaped counterparts[65]. The increased half-life of rod shaped NPs is attributed to decreased uptake by macrophages. However, both nanospheres and nanorods accumulated to a significant extent in the liver and spleen[65]. It has been shown that PEGylated short rod silica NPs with 1.5 aspect ratio accumulate more in liver whereas PEGylated long rod shaped NPs with aspect ratio of 5 deposited more in spleen[66]. In addition, although there is more renal clearance of short rod NPs, long rod NPs exhibited faster clearance rate from the tissues. It is speculated that biodistribution and retention ability of particles in tissues may be relative to the uptake ability of various types of immune cells in different tissues. Another study also demonstrated differential biodistribution and clearance of different shaped NPs[67]. The accumulation of discoidal particles in heart and lung were increased with decreased liver deposition compared to spherical particles. This might be associated with larger rotational inertia and surface of adhesion of discoidal particles. In contrast, cylindrical particles were most concentrated in liver than other peripheral tissues due to increased internalization in Kupffer cells[67].

## 1.3 Internalization and Cell Fate of NPs

For certain applications like siRNA delivery, an IONP formulation that possesses a high internalization rate is preferred. In contrast, IONP formulations that minimize cell uptake are preferred to optimize pharmacokinetic parameters such as half-life. Thus, it is important that the basic physicochemical properties governing the tissue and cellular accumulation of IONPs be identified. Biotransformation and degradation of IONPs in vivo can be studied by monitoring the loss of magnetic properties and total iron content in tissue[68]. Moreover, as cell toxicity is likely directly correlated to the tissue and cellular uptake of IONPs such an understanding of the important physicochemical properties involved in NP uptake is likely to lead to a better management of toxicity concerns[69].

It is generally understood that endocytosis is the primary mechanism by which IONPs enter the cells.[70] Some early works revealed that the amount of IONPs uptake in macrophages is directly correlated with cellular phagocytic activity[71]. Endocytosis is an energy dependent process often associated with other cell trafficking events such as secretory pathways and autophagy[72,73]. Although many questions regarding endocytosis still remain unknown, continued research examining IONPs internalization has enhanced our understanding of this particular cellular response and ultimately assisted in the rational design of IONP formulations that can take advantage of specific endocytosis pathways[74]. The various types of endocytosis is illustrated by Figure 1.6. Conventionally, endocytosis is categorized as a “cell drinking” process called pinocytosis and “cell eating” process called phagocytosis. Based on the proteins involved in initial adhesion and internalization at the plasma membrane, pinocytosis is further classified into clathrin mediated, caveolae mediated, macropinocytosis, and clathrin and caveolae independent endocytosis[75].

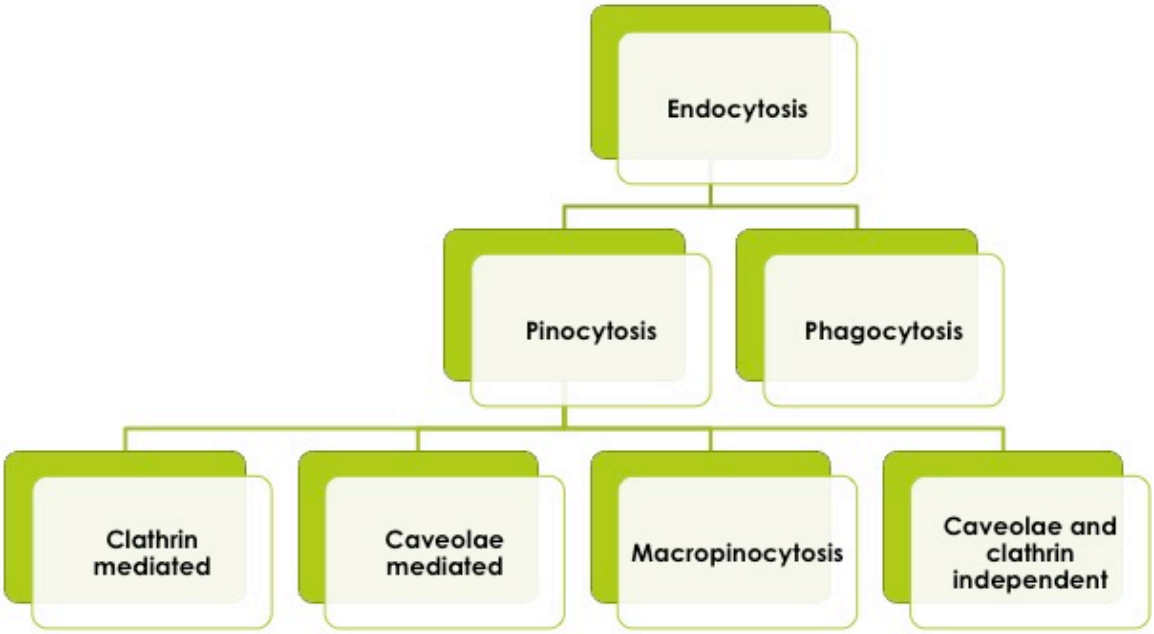


**Figure 1.6 Classification of endocytosis.**

It is of note that IONPs internalization pathway is not mutually exclusive. There are many reports that show IONPs internalization utilize more than one pathway. For example, a recent study reported IONPs accumulate in three different cells using clathrin mediated and macropinocytosis pathways[76]. Another study shows that internalization of silica coated IONPs in HeLa cells were mediated by caveolin-1 and Cdc42[77].

## 1.3.2 Clathrin Mediated Endocytosis

Clathrin mediated endocytosis has been extensively characterized. It is responsible for uptake of essential nutrients like cholesterol by low density lipoprotein (LDL) receptor, or iron by transferrin receptor[78]. Therefore, transferrin has been used as marker to probe the clathrin mediated endocytosis pathway[79]. The hallmark of clathrin-mediated endocytosis is formation of clathrin coated pits around the membrane invagination following transmembrane receptor

activation[80]. The size of clathrin coated pits can reach up to 200 nm diameter[81]. Once the membrane vesicle is internalized into the cytosol, the clathrin coated pits will lose their clathrin coating and fuse with various other endocytic vesicles to form early endosomes. At the same time, early endosomes can be recycled back to the cell surface and release their contents, or fuse with the lysosome for degradation[82]. Figure 1.7 illustrated the events occurring during clathrin mediated endocytosis.

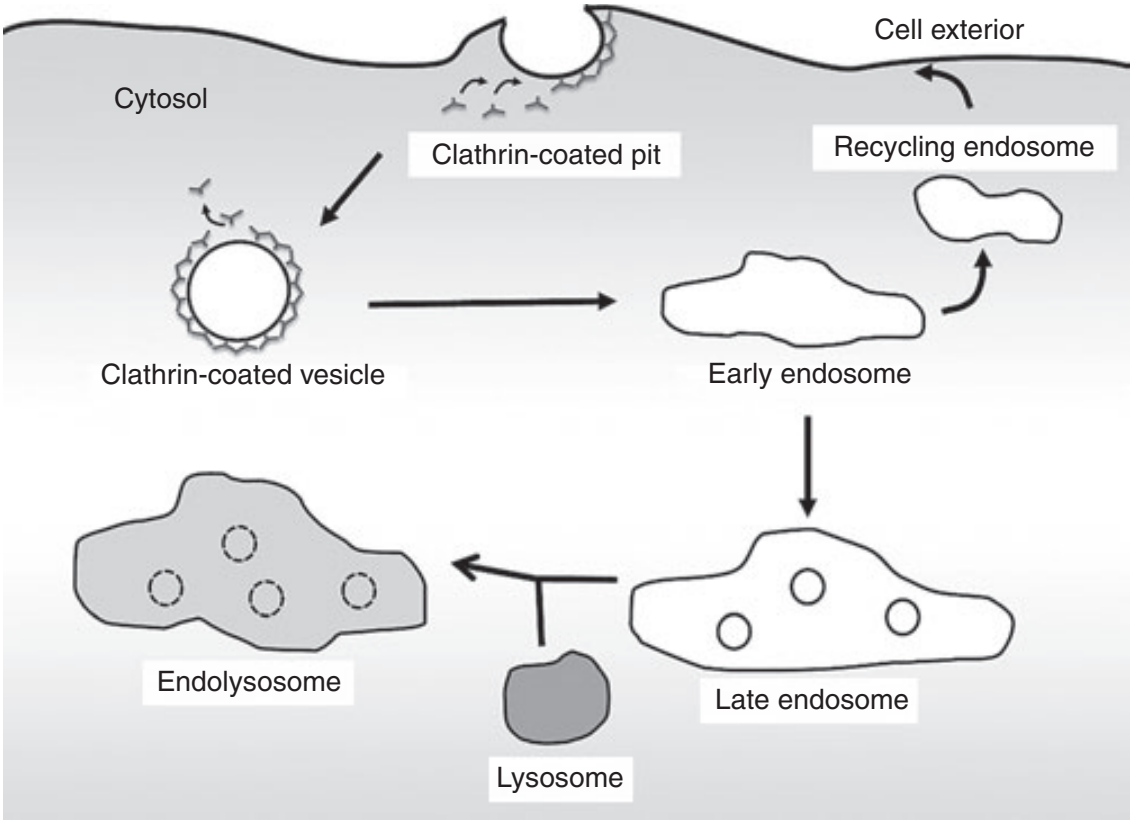


**Figure 1.7 Cell fate of clathrin mediated endocytosis. Reproduced with permission from El-Sayed et al. Mol Ther. 2013 Jun;21(6):1118-30. Copyright © Nature Publishing Group.**

To determine if cells employ clathrin mediated endocytosis to internalize NPs, pharmacological inhibitors, such as chlorpromazine, are widely used[83]. Positively charged IONPs are most commonly internalized by clathrin mediated endocytosis, although additional endocytic pathways have also been reported. Studies by Huth et al., 2004 reported cell-dependent

mechanism of entry of PEI coated IONPs. In both human lung epithelial cells (BEAS-2B) and liver cancer cell lines (HepG2), clathrin mediated endocytosis played an important role whereas in human cervical cancer cells (Hela), both clathrin and caveolae dependent pathway were utilized[84]. It is hypothesized that albumin binding to PEI facilitated the endocytosis process via clathrin[85]. A recent study shows that in the presence of fetal calf serum, primary rat neurons treated with a clathrin mediated endocytosis inhibitor displayed significantly reduced uptake of dimercaptosuccinate (DMSA)-coated IONPs[86]. In contrast, inhibitors of other endocytosis pathways had no effect. Based on these findings, it is suggested that protein absorbed onto IONPs surface could regulate their internalization pathway[86]. This effect is more dominant for clathrin dependent endocytosis pathways due to abundance of albumin protein in blood stream.

### 1.3.1 Caveolae Mediated Endocytosis

Recently, El-Sayed et al., 2013 suggested classifying endocytosis based on the cell membrane location where internalization occurs (i.e. lipid raft)[87]. Lipid rafts are small patches of cell membrane that are heterogeneous and rich in cholesterol, sphingolipid and glycosylphosphatidylinositol (GPI) anchored proteins[88]. Caveolae are inward, flask-shaped curvatures of the plasma membrane formed when a group of caveolin proteins bind to cholesterol in the lipid raft region of cell membrane[89]. The typical size of the caveolae are approximately 60-80 nm diameter in size, however, studies have demonstrated that caveolae can accommodate up to 100 nm NPs[90]. Caveolae are particularly enriched in endothelial cells, but also present in fibroblasts, and adipocytes[91]. Following of the initial internalization of the caveolae from lipid rafts, the fate of caveolae is dependent on the cell type in which endocytosis occurs. In non-endothelial cells, caveolae are subjected to endosomal-lysosomal system processing, while in endothelial cells, caveolae may bypass the lysosome and transport cargo across the endothelial

cell layer[87,92]. Bovine serum albumin (BSA) and cholera toxin B (CTB) are known markers for caveolae mediated endocytosis[93]. Therefore, they can be used as probes for caveolae mediated endocytosis. Several pharmacological inhibitors of this pathway have been described. Cholesterol depletion agents like Methyl-β-cyclodextrin (MβCD) and other cholesterol interacting molecules like nystatin and genestin have been widely used as inhibitors for caveolae mediated endocytosis[94].

Although negatively charged IONPs show lower uptake profile compared to positively charged IONPs, IONPs with negative surface charge still interact with the cellular membrane and are taken up by different cells. It has been reported that negatively charged IONPs can interact with cationic lipid domains in the lipid raft. For this reason, the internalization of negatively charged IONPs was often mediated by caveolae dependent endocytosis[95]. These findings are important as they suggest that surface chemistry and functional groups present on the outside of the IONPs dictate the route of internalization in the cell. Further evidence of this are the studies by Hsu et al., 2012 demonstrating that positively charged chitosan coated IONPs and negatively charged hyaluronan-modified chitosan coated IONPs may activate different endocytosis pathway. In these studies, chitosan coated IONPs favored uptake by clathrin mediated endocytosis, while the hyaluronan modified chitosan favored more caveolae mediated endocytosis routes[96].

### 1.3.3 Macropinocytosis

Macropinocytosis begins with ruffing of the plasma membrane and actin polymerization[97]. The ruffled membrane folds over and eventually forms a closed loop called "macropinosomes". The macropinosomes can be quite large (0.5–10 μm) and accommodate a large payload. Once in the cytosol, the macropinosomes shed off actin filament on the surface

and fuse with lysosomes for either degradation or recycling back to the cell surface depending on the cell type[87]. Macropinocytosis can be inhibited by actin polymerization inhibitor cytochalasin D, the $Na^+/H^+$ exchanger inhibitor amiloride. Figure 1.8 shows a schematic drawing of macropinocytosis and inhibitors. There are only few cell types where macropinocytosis is absent, such as macrophages and brain microvessel endothelial cells. Thus, in most cell types, it can serve as a non-specific entry point into the cells[75].

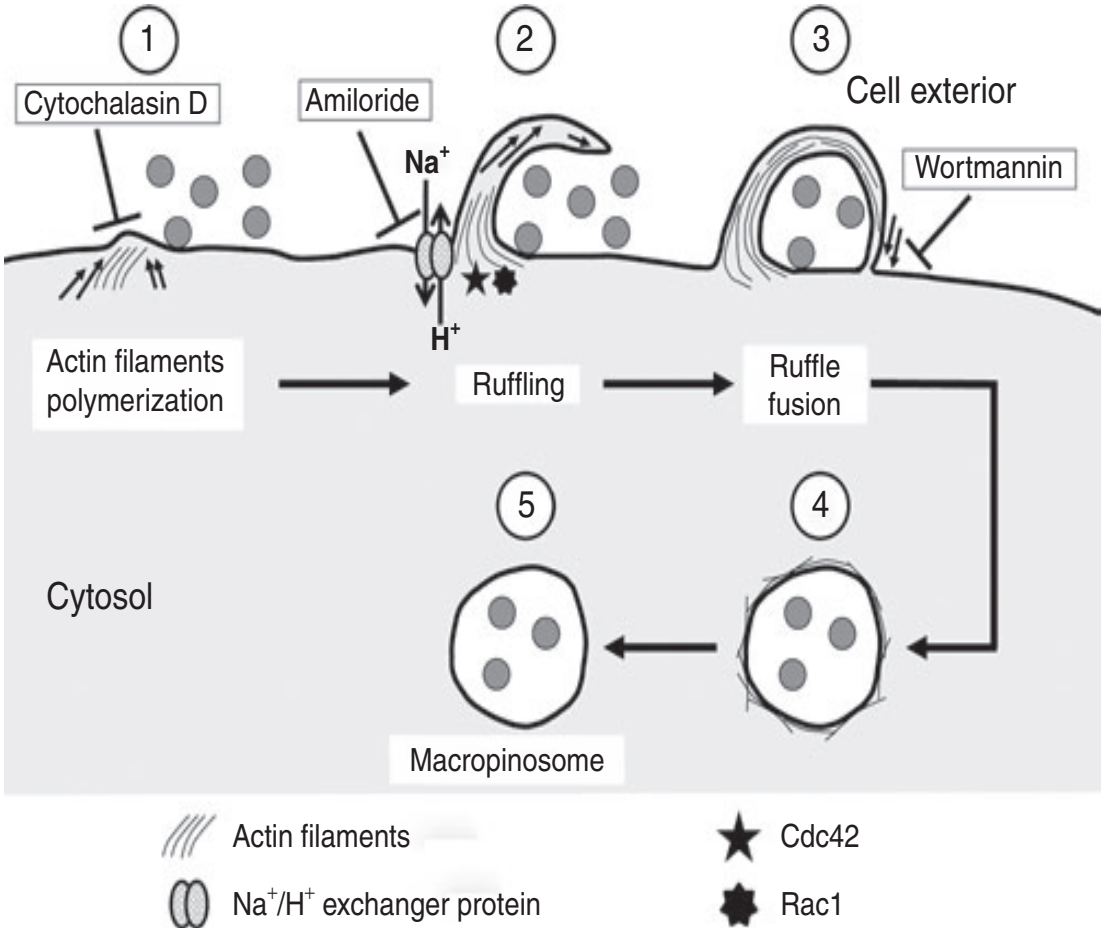


**Figure 1.8 Schematic overview of macropinocytosis and inhibitors. Reproduced with permission from El-Sayed et al. Mol Ther. 2013 Jun;21(6):1118-30. Copyright © Nature Publishing Group.**

Examples of IONPs using macropinocytosis as a route of entry can be found in several different cells. Panariti and colleagues demonstrated L-3,4-dihydroxyphenylalanine (L-

DOPA) coated IONPs activated macropinocytosis pathways in lung epithelial cells[98]. In addition, entry of oleic acid coated IONPs into HeLa cells were mediated by a macropinocytosis-like mechanism as a reduced number of IONPs accumulated inside the cell upon treatment with macropinocytosis inhibitors like wortmannin[99]. Once inside the cell, IONPs were subject for lysosomal degradation[99].

### 1.3.4 Clathrin and Caveolae Independent Endocytosis

This type of endocytosis consists of any endocytosis process that does not take place through clathrin or caveolin coated regions of the plasma membrane. Based on regulator proteins involved in this process, it is now further classified as Arf6- dependent, flotillin-dependent, Cdc42-dependent and RhoA-dependent pathways[75]. Arf6 is a small GTPase protein that not only plays an active role in clathrin mediated endocytosis, but also implicated in a distinctive endocytic pathway involving the uptake and recycling of class I major histocompatibility complex (MHC-I)[100]. This pathway requires the activation of Arf6 and the presence of actin filaments[100]. In addition to MHC-1, β1-integrin, cellular prion protein and E-cadherin can also undergo this pathway[101-103]. Flotillin dependent pathway is similar to caveolae mediated endocytosis expect the vesicles does not contain caveolin. The vesicle membranes are enriched with flotillin-1 and flotillin-2 proteins. There is no selective chemical inhibitor for flotillin-dependent endocytosis available[87]. Cdc42 dependent pathway is sensitive to cholesterol depletion and requires actin polymerization, which is mediated by Cdc42 activation[104]. The vesicles are different from macropinosome and free of clathrin coating and caveolae enrichment[105]. A specific inhibitor for this pathway is not available, however, a small molecule inhibitor “Secramine A” for Cdc42 GTPase can be used[106]. RhoA dependent pathway was first

discovered in internalization of IL-2 receptor on T cells[107]. This pathway seems to have a limited number of substrate such as Clostridium toxins and also sensitive to cholesterol depletion[108].

Researchers are still working out the molecular details regarding endocytosis pathways and developing specific inhibitors. Very few IONPs have been reported to undergo clathrin and caveolae-independent endocytosis. Using genetic tools, a recent study demonstrated that Cdc42 and caveolin-1 facilitate internalization of negatively charged silica coated, carboxylated and PEGylated IONPs in HeLa cells[77].

### 1.3.5 Phagocytosis

Phagocytosis often occurs in specialized immune cells such as macrophages or dendritic cells for the purpose of internalization of micron sized large particles like fungi, bacteria or viruses[109]. There are some similarities between phagocytosis and macropinocytosis with regards to actin cytoskeleton reorganization. Particles are internalized into uncoated vesicles called “phagosomes”. Phagosomes fuse with early endosomes and fuse with other early endosomes to create later endosome. Eventually, phagosome will fuse with lysosomes to digest the particles[110]. To date, there is no inhibitor specifically for phagocytosis. However, it has been shown that phagocytosis depends on dynamin-2 and actin polymerization. Phagocytosis may be identified by the combined treatment of cytochalasin D and dynasore, which are inhibitors for actin polyermerization and dynamin-2, respectively[79].

Macrophages are specialized for recognition of foreign particles. Absorption of opsonins including complement proteins, serum proteins, and immunoglobulin allows receptor on macrophage to bind to opsonized particles. This process is called “opsonization”. Fc receptor or complement receptors play a direct role in opsonization[75]. Other receptors may also play a role

in phagocytosis of IONPs. Scavenger receptor expressed on the surface of macrophage can recognize both positively and negatively charged IONPs[111].

## 1.4 Barriers of the Brain

German scientist Paul Ehrlich made important observations in 1885 when he discovered that intravenous injection of trypan blue dye stained all peripheral organs except the brain and spinal cord. Ehrlich believed that this phenomon was attributed to the fact that brain possessed lower binding affinity for the dye. Later, Edwin E. Goldmann, an associate of Paul Ehrlich, found that brain tissue stained with the trypan blue dye following injection of the dye into the cerebrospinal fluid (CSF), thus confirming a cellular barrier between the blood and the brain[112]. In the late nineteenth century, Bield, Kraus and Lewandowsky coined the term "blood-brain barrier" to describe this observation. The development of electron microscopy greatly unraveled the mystery of the BBB formed by brain endothelial cells. However, the barrier property of brain vasculature is not uniform throughout the brain. It is found that the capillaries around circumventricular organs near the third and fourth ventricle region of the brain are more permeable to allow release of hormones from brain into blood[113]. Moreover, the epithelial cells of the choroid plexus formed the blood cerebral spinal fluid (CSF) barrier. The blood-cerebral spinal fluid barrier, together with the BBB, together have a protective role limiting toxic molecules and drug accumulation in the brain as illustrated in Figure 1.9[114].

The blood-CSF barrier consists of a single layer of epithelial cells surrounding extensive network of capillaries in choroid plexus that are specialized structures projecting in ventricles of the brain and are responsible for the active secretion of CSF. A drawing of choroid plexus and blood-CSF barrier is shown in Figure 1.9. Despite the fact that blood-CSF barrier is considered smaller than BBB, the presence of microvilli on the apical epithelial surface of the blood-CSF barrier provides considerable surface area[115]. Tight junctions are also present between choroidal epithelial cells, providing restrictive paracellular diffusion within the blood-CSF

barrier[116]. However, the tight junction proteins expressed on blood-CSF barrier are different than the ones in BBB. For example, claudin 2, characterized as a monovalent cation selective channel, expressed on blood-CSF barrier belong to pore forming category whereas claudin 5 on BBB belong to barrier tightening category[117]. A thin endothelium resting on basal membrane shows fenestration allowing free movement of fluid and molecules such as solutes and proteins[118]. Choroid plexus epithelial cells transport various nutrients, including folate and vitamins, and proteins like prolactin and leptin from blood to CSF where they can readily enter the brain across the permeable ependyma and pia-glia[119,120]. The characteristics of choroidal epithelium include high level of pinocytotic vesicles and large number of mitochondria to maintain energy required for ionic gradients and fluid secretion[121].

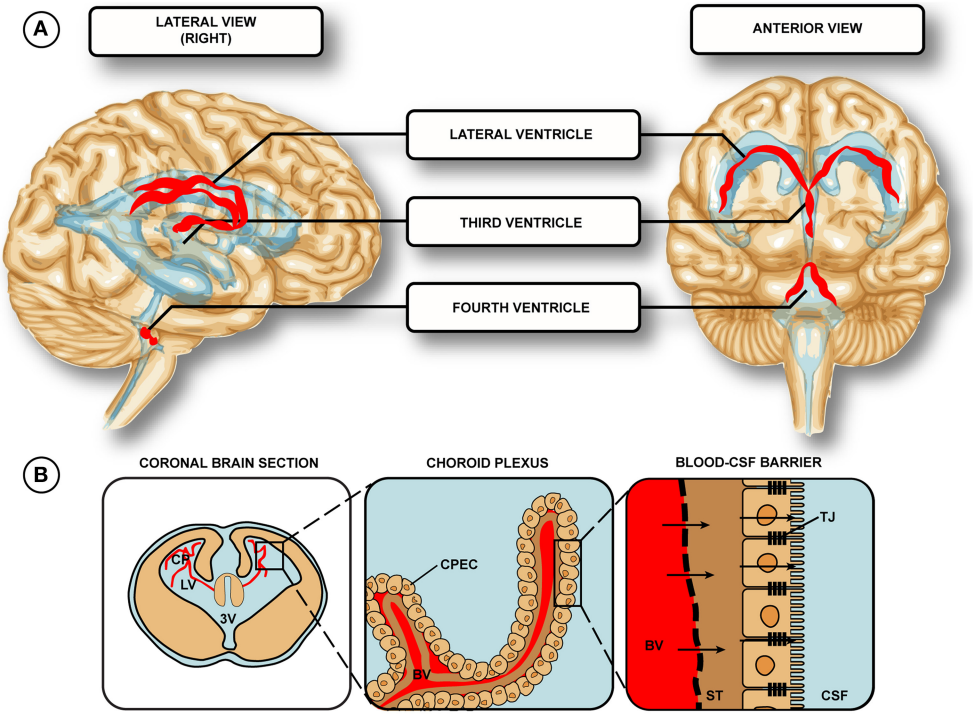


**Figure 1.9 Choroid plexuses and blood-CSF barrier. (A) The choroid plexuses are present in the two lateral, third and fourth ventricles (red ribbons). (B) Each of the plexuses is comprised of fenestrated vessels, with a single layer of intimately opposed choroid epithelial cells, joined by tight junctions—forming the blood-CSF barrier. CPEC: choroid plexus epithelial cells. Blood-CSF barrier: blood-cerebrospinal fluid barrier. Reproduced**

**with permission from Liddelow SA. Front Neurosci. 2015 Mar 3;9:32. Copyright © Liddelow**

## 1.4.1 Structure and Physiology of the BBB

The BBB consists of brain microvessel endothelial cells surrounded by pericytes, astrocyte end feet, and neuronal terminations as shown in Figure 1.10. Astrocyte end feet spread over the basal lamina of the brain endothelial cells and contribute to the barrier properties by releasing various signaling molecules such as transforming growth factor-β (TGF-β), glial-derived neurotrophic factor (GDNF), basic fibroblast growth factor (bFGF), interleukin (IL) 6, and neurotrophins[122-124]. Astrocyte end feet also possess a high density of orthogonal arrays of particles (OAPs) including water channel aquaporin 4 and the Kir4.1potassium channel, which facilitates ion and water volume regulation capability. It has been found that the expression of OAPs correlates with expression of agrin on the basal lamina membrane of endothelial cells. Agrin regulates integrity of the BBB. Astrocytes and brain endothelial cell coculture exhibit higher transepithelial electrical resistance (TEER) readings compared to brain endothelial cells alone, indicating astrocytes enhance the integrity of the BBB[125,126]. Pericytes lie between the astrocyte end feet and capillary wall. The ratio of pericytes to endothelial cells is proposed to be 1:3[127]. The pericytes have similar function as smooth muscle, which control vasculature tone, and endothelial growth[128]. Pericytes regulate BBB-specific gene expression patterns in endothelial cells, and induce polarization of astrocyte end-feet surrounding CNS blood vessels[129]. Dysfunction of pericytes in animal model leads to loss of BBB integrity and reduction in regional cerebral blood flow[129]. Finally, neuronal terminations are linked and supplied with oxygen and nutrient by astrocytes. In brain capillaries, blood cells, such as polymorphonuclear

cells, lymphocytes and monocytes adhere and roll along the vascular lumen and providing surveillance for brain activity[130].

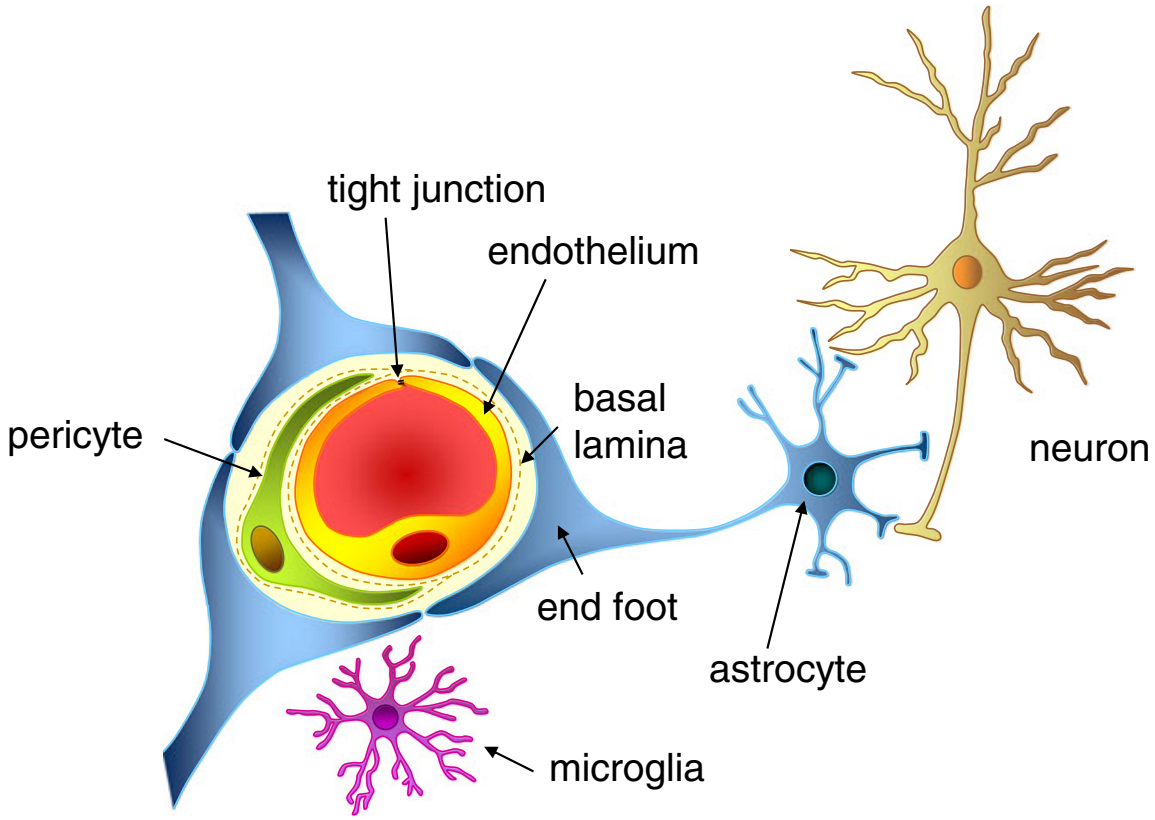


**Figure 1.10 Anatomical structure of the BBB. Reproduced with permission from Abbott NJ. J Inherit Metab Dis. 2013 May;36(3):437-49. Copyright © Springer.**

Although brain capillaries are morphologically similar to other capillary beds, they have the following distinct features: 1) low pinocytic activity; 2) absence of fenestrations; 3) presence of tight junctions; 4) high mitochondrial content; 5) specialized transport systems[131]. The physical barrier of the BBB is attributable to the presence of tight junctions and absence of macropinocytosis and fenestrations, that together limit transcellular and paracellular permeability of hydrophilic molecules[132]. For hydrophobic molecules, brain endothelial cells are able to utilize the ATP energy generated by high mitochondrial volume to actively transport a broad range of substrates back to the blood stream via drug efflux transporters.

### 1.4.2 Tight Junction Proteins

The tight junctions between endothelial cells limit the paracellular diffusion of hydrophilic molecules into the brain. Generally, there is little paracellular diffusion of hydrophilic molecules with greater than 600 Da across the tight junction[133]. The transepithelial electrical resistance (TEER) across the BBB can reach up to 2000 Ω.cm$^2$ compared to less than 50 Ω.cm$^2$ in other tissues[134]. Tight junctions consist of transmembrane proteins including occludin, claudins, and junctional adhesion molecule (JAM) as illustrated in Figure 1.11. These proteins are located on the apical side of the plasma membrane. Occludin is one of the first tight junction proteins discovered. It contains two identical extracellular loops of occludin, four transmembrane domains and a conserved C terminus that connects with zonula occludens protein (ZO) via a helical structure[135]. ZO proteins can directly bind to F-actin, and interact with regulatory proteins such as protein kinase C (PKC), tyrosine kinase c-Yes, PI3K and gap junction component, connexin 26. It is reported that the enhanced junctional properties of occludin in brain endothelial cells is due in part to a high degree of phosphorylation compared to the occludins found in the peripheral endothelium[136,137]. Similar to occludin, claudins can form homophilic interactions with each other. Claudins and occludin can also form heteropolymers that regulate diffusion of ions and hydrophilic molecules[138]. The expression of claudins seems to contribute to high TEER reading[139]. Transfection of MDCK cells with claudin-1 increased the transepithelial resistance about 4- fold and reduced the paracellular flux[140]. Claudin-1, -3, -5 and -12 were found in endothelial cells[141]. However, the presence of claudin-1 in the blood brain barrier seems to be variable among different species and is not definitively clarified[139]. This may attribute to the fact that certain antibody against claudin-3 may also cross-reactive with claudin-1. The claudin-5 mRNA level of cerebral capillaries is 600–700 times higher compared to

claudin-1, -3 or -12 mRNAs[142-144]. The cloudin-5 knockout mice show BBB impairment and die 10 hour after birth[145]. JAMs belong to the immunoglobulin superfamily. JAMs can form homo or heterodimers between different JAM family members as well as other adhesion molecules such as integrins that contribute to tight junction structure[146]. JAMs regulate the formation of tight junctions during the acquisition of cell polarity[147]. JAMs are also associated with monocyte extravasation[148].

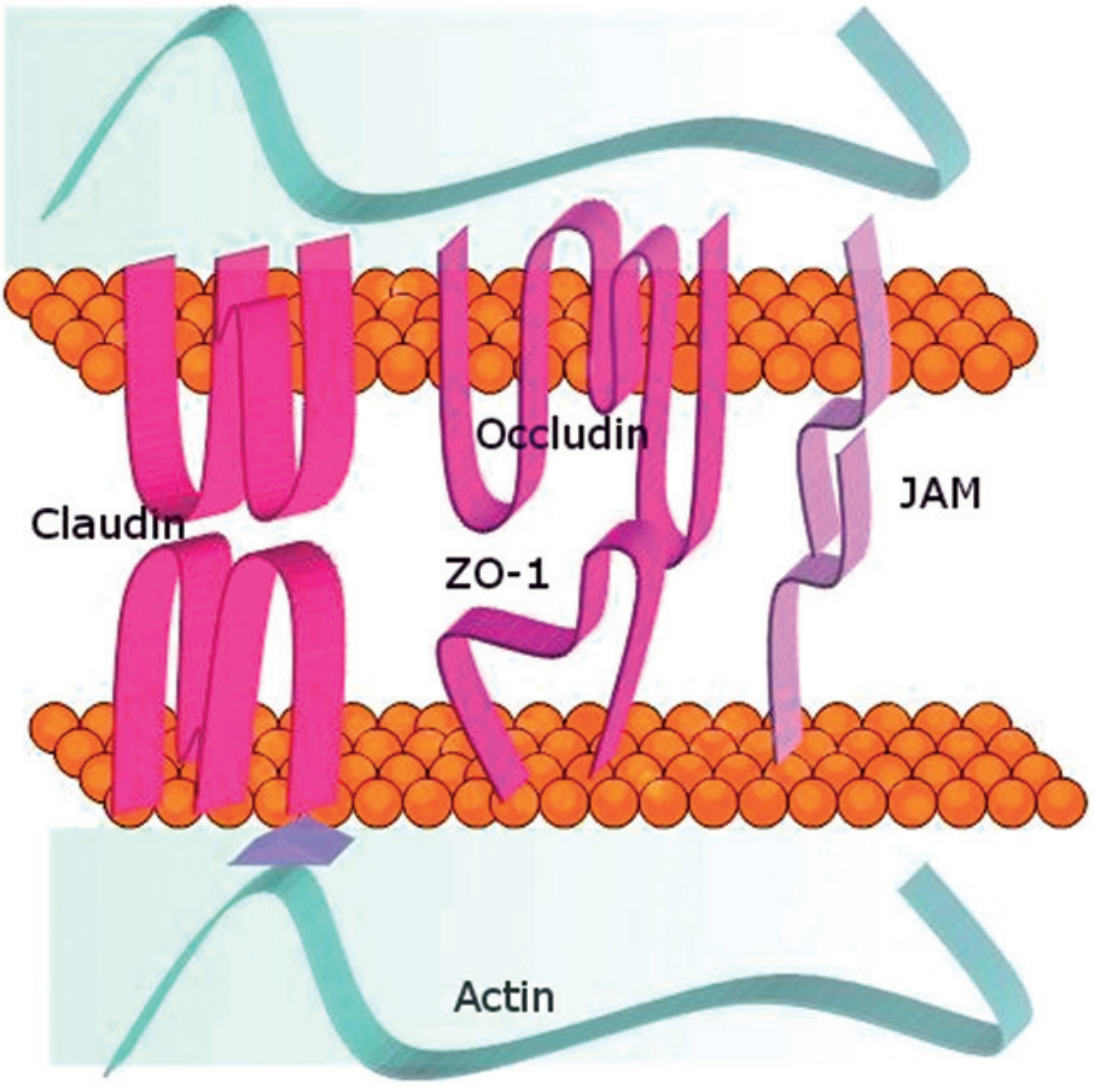


**Figure 1.11 Tight junction structures. Reproduced with permission from Tajes et al. Mol Membr Biol. 2014 Aug;31(5):152-67. Copyright © Informa Healthcare.**

Besides tight junction proteins, adherens junction proteins are also present between brain endothelial cells and help maintain cell-cell contact[136]. The main components of adherens junctions are vascular endothelium cadherin (VE-cadherin) that forms homotypic adhesive complexes with adjacent cells in the presence of calcium[149]. Cadherin proteins are linked to the actin cytoskeleton through β-catenin, α-actinin, and vinculin protein. Although cadherin proteins have generally been considered to have a minor role maintaining BBB integrity, studies have shown VE-cadherin promotes claudin-5 expression[150]. Furthermore, β-catenin plays an essential role in regulating tight junction permeability as a transcription factor. As part of the downstream Wnt signaling pathway, β-catenin induces formation, maturation, and maintenance of BBB during developmental. Another adherens junction protein is platelet endothelial cell adhesion molecule (PECAM-1), also known as CD31. While CD31 does not appear to be important in maintaining BBB integrity it has a role in restoration of the barrier properties following injury. A study by Graesser et al., 2002 demonstrated CD31 knock down mice results in early onset of experimental autoimmune encephalomyelitis with increased leukocyte migration across the BBB[151].

### 1.4.3 Transporters

Due to restricted paracellular diffusion, many transporters are expressed on brain endothelial cells to facilitate the entry of nutrients into the brain. For example, glucose and amino acid can be transported into the brain via specific transporter proteins located on the plasma membrane of the endothelial cells. Besides various solute uptake transporters, the expression of efflux transporters plays a protective role in limiting the entry of hydrophobic molecules into the brain. P-glycoprotein (P-gp), multidrug resistance associated proteins (MRP),

and breast cancer resistance protein (BCRP) can greatly affect the brain distribution of many drugs[152]. Therefore, they significantly contribute to the barrier function of the BBB.

P-gp, MRP and BCRP belong to ATP-binding cassette (ABC) protein superfamily. They are expressed in various tissues including the apical side of human brain microvessel endothelial cells that form the BBB. They play a critical protective role in normal BBB function effluxing potential toxic compounds/xenobiotics out of the brain through an ATP-dependent process[153]. Generally speaking, P-gp and BCRP binds to positively charged molecules whereas MRP binds to negatively charged compounds. In disease condition, the expression and function of these efflux transporters may be altered and in turn contribute to pathology of the disease such as Alzheimer's disease[154].

P-gp possesses the ability to efflux out its substrates directly from the plasma membrane[155]. P-gp can binds to its substrate with molecular weight up to 2000 Da. It is very common for P-gp substrate to have two aromatic rings and a basic nitrogen atom. Recent reports suggest that P-gp but not BCRP can actively transport β-amyloid protein out of the brain[156,157]. There is a continuous interest to develop specific and highly potent P-gp inhibitors. Especially in the field of cancer research, due to expression of P-gp on various cancer cells, inhibition of P-gp activity can result in increased cellular concentration of chemotherapeutics that are P-gp substrates. The first generation of P-gp inhibitor includes verapamil and cyclosporin A with low specificity and profound side effect. They inhibit by competitive binding to active site of P-gp. The second generation of P-gp inhibitor includes dexverapamil and dexniguldipine with decreased side effect. The third generation includes tariquidar and elacridar as non-competitive, non-substrate with increased specificity.

MRP was first identified in 1992 with the initial cloning of MRP1 from a small cell lung cancer cell line[158]. The MRP family now consists of 9 MRPs (MRP1 – 9). Besides brain, MRP can also expressed on other tissues such as liver, kidney and small intestines. It has been reported that MRP2 is expressed on apical membrane whereas MRP3 is expressed on basolateral membrane of hepatocytes[159]. MRP1 and 4 are expressed in brain endothelial cells[160]. MRP1 and 4 are expressed on apical membrane of brain endothelial cells and basolateral membrane of epithelial cells forming the blood-cerebrospinal fluid barrier (blood-CSF barrier)[161]. The MRP family members play multiple roles in limiting the drug accumulation in CNS.

BCRP was initially discovered in the MCF-7 breast cancer cell line after observing that the cells are resistant to several chemotherapeutics including mitoxantrone, doxorubicin, and daunorubicin[162]. BCRP is considered as a half-transporter with 72 kDa molecular weight. BCRP is expressed on the apical membrane of brain endothelial cells. It limits the brain accumulation of endogenous substrates such as sulfate and glucuronide conjugates of estrone and dehydroepiandrosterone[163,164]. BCRP also interacts with many xenobiotics, many of which are also substrates of P-gp.

# 1.5 NP Delivery across the BBB

## 1.5.1 Receptor Mediated Transcytosis

Receptor mediated delivery of NPs to the brain has attracted much attention in recent years due to the non-invasive nature and potential for targeted delivery to the brain. The design of NPs to utilize specific receptor-mediated vesicular transport processes in the brain capillary endothelial cells represents what has been termed the "Trojan Horse" approach for enhancing transcellular permeability across the BBB. The most well characterized receptor-mediated transport processes in the BBB are discussed below.

### 1.5.1.1 Low-Density Lipoprotein Receptor Mediated Delivery

The low-density lipoprotein receptor related protein 1 (LRP1/CD91/α2-macroglobulin receptor) is a member of the LDL receptor family and it is highly expressed at both luminal and ablumenal of brain microvessel endothelial cells[165]. Upon binding to their ligands, the receptors carry the ligand across the BBB through a receptor-mediated transcytosis process. There are two forms of LRP1 receptor, one is membrane bound, and the other is soluble form. This section focuses mainly on membrane bound form of LRP1. The natural ligand of LRP1 includes beta amyloid, ApoE, lactoferrin, RAP, α2-macrogloblin and many others[166]. It has been reported that LRP1 mediates cellular internalization of ligands and their transport across the BBB.

Angiopep has demonstrated high transcytosis capacity in brain capillaries and substantial parenchymal brain accumulation due to binding and transport via LRP1[167]. The Angiopep peptides have been advanced as potential BBB targeting vectors for drug delivery applications to the brain, especially for delivery of chemotherapeutics for treating brain tumors.

A potential advantage of Angiopep targeted brain delivery of therapeutic molecules is the ability of the targeting vector to localize in tumors with increased LRP1 expression[168]. Particularly attractive, in addition to the high transcytosis of the peptide, is the capability to attach multiple drug molecules to the peptide. With the ability to attach up to three small molecules onto the Angiopep peptide backbone, the relatively low efficiency of the trancytosis pathway can be countered.

Recently, the use of Angiopep targeting vectors to deliver NPs to the brain has also been reported. Using angiopep coated nanoparticles, a significant increase in survival rate was observed in a mouse glioma model compared to both control and temozolomide treatment groups[169]. In these studies the angiopep peptide was used to deliver DNA loaded nanoparticles to the tumor cells, taking advantage of the relatively potent activity of the gene based therapy. Additional studies have used angiopep peptide to deliver paclitaxel loaded nanoparticles (ANG-PEG-NP)[170]. These studies showed an enhanced tumor response to paclitaxel loaded ANG-PEG-NP compared to paclitaxel loaded nanoparticles without the ANG vector in a mouse glioblastoma model[170].

The most clinically advanced angiopep delivery molecule is GRN1005, a paclitaxel–Angiopep-2 peptide–drug conjugate that has successfully completed phase I clinical trial for the treatment of recurrent glioma[171]. Additional angiopep conjugations with doxorubicin have shown good response in pre-clinical brain tumor models[172]. However, phase II clinical trial of GRN1005 in non-small cell lung cancer patients with brain metastases was discontinued and it is likely not to advance past phase III due to absence of significant effect. This discrepancy may be due in part to the substantial smaller size of rodent brains used in the pre-clinical trials. Leakiness within a rodent brain tumor may result in greater brain exposure than that observed in

human brain tumor patients. Currently, GRN1005 is undergoing a phase II study conducting in patients with high-grade glioma.

Besides angiopep, apoE is another ligand used for LRP1 mediated transcytosis across the BBB. Instead of using apoE as a targeting ligand directly, polysorbate 80 (Tween-80) is often used. It has been reported that polysorbate 80 coated NPs are capable for delivering BBB-impermeable molecular imaging contrast agents into the brain[173]. However, the same NPs do not cross the BBB in apoE knockout mice, demonstrating polysorbate 80 can absorb apoE on NPs surface and cross the BBB via receptor-mediated transcytosis[173].

#### 1.5.1.2 Diphtheria Toxin Receptor Mediated Delivery

Another novel ligand for transport cross the BBB is cross-reacting material 197 (CRM197), a non-toxin protein mutant of diphtheria toxin. Like diphtheria toxin, it binds to diphtheria receptors that are expressed in the BBB and are up regulated in ischemic stroke and glioma[174,175]. CRM197-grafted polybutylcyanoacrylate (PBCA) nanoparticles were able to traverse a monolayer of human brain-microvascular endothelial cells (HBMECs) *in vitro*[176]. In addition, an increase in the grafting quantity of CRM197 enhanced the permeability and the uptake efficiency of NPs by HBMECs[176]. Another study suggested that CRM197 can increase BBB permeability via up-regulation of caveolin-1 protein, increased pinocytotic vesicles, and redistribution of tight junction-associated proteins in brain microvessel[177].

#### 1.5.1.3 Considerations of Receptor Mediated Transport across the BBB

Drug delivery utilizing receptor-mediated transcytosis in the BBB certainly shows great potential to enhance drug accumulation in the brain. However, the most limiting drawback associated with this method is its low efficiency. For example, transferrin conjugated micelles have been reported with 0.03% ID/g inside the brain[178]. By fusing with an insulin receptor

antibody, there was 0.02% of ID/g of human erythropoietin taken up by brain[179]. This represents a very small fraction of the drug reaching its intended target within the primate brain. While the LRP1 receptor has shown substantially better delivery efficiencies (approximately 10-fold better using angiopep modified Polyamidoamine dendrimers) there was still only 0.25% ID/g delivered to the brain[180]. The best efficiency to date is with doxorubicin and etoposide conjugated angiopep, with reported delivery of 0.5% and 1% ID/g in mouse brain tissue and brain tumor tissue, respectively[172]. These data collectively suggest that 1% of the ID/g is the upper limit for receptor mediated transport across the BBB. With this relatively low efficiency of delivery, receptor mediated transport would be limited to high potency therapeutic agents, and would substantially limit the drug delivery options.

One of the limitations in evaluating the various receptor-mediated vesicular transport routes for delivery of drugs to the brain is a lack of standardization in terms of both the drug being delivered and the pre-clinical model used to examine effectiveness of delivery approach. However, studies by van Rooy and colleagues provide an initial assessment of the various receptor-mediated delivery approaches by comparing the brain delivery efficiency of five targeting ligands including transferrin, RI7217 (an antibody against transferrin receptor), COG133 (an apoE-mimetic peptide targeting LRP1), angiopep-2, and CRM197[181]. Each targeting ligand was attached to a liposome drug carrier using similar chemistry and stoichiometry and evaluated for BBB permeability using the same *in vitro* and *in vivo* models[181]. *In vitro* experiments show that only CRM197-modified liposomes were able to bind to murine endothelial cells (bEnd.3) while both CRM197 and RI7217-modified liposomes associated with human endothelial cells (hCMEC/D3). Interestingly, only the RI7217 was able to significantly enhance brain parenchyma uptake of liposome. However, despite a 4.3 fold increase in delivery

to the brain with RI7217 modified liposomes there was only 0.18% of the injected dose detected in the brain after 12 hours[181]. In light of the positive *in vitro* findings, the possible explanation for failure of CRM197 modified liposome to cross the BBB *in vivo,* is low expression level of target receptor in healthy mice.

A recent review has summarized the ligand-targeted nanomedicines currently undergoing clinical trials[182]. None of the nanoparticle formulations have progressed into phase III clinical trials. This is due to the fact that comparison of PK and tissue distribution of ligand-targeted versus non-targeted nanomedicine is often inconclusive and the contribution of targeting ligands has yet to be proven to enhance delivery efficacy[182]. Given the lack of translation of Trojan horse technology to the delivery of NPs in the clinic, alternative routes should be considered, some of which are discussed below.

### 1.5.2 Disruption of the BBB

It is reported that more than 98% of small molecules cannot penetrate the BBB[183]. Many attempts to modulate the permeability of BBB and to enhance drug localization in brain have been made. Various endogenous and exogenous compounds modulate the BBB permeability. For example, vasogenic agents histamine, and bradykinin, growth factors vascular endothelial growth factor (VEGF), basic fibroblast growth factor bFGF and transforming growth factor–β (TGFβ), have been used to regulate BBB permeability[184-186]. In addition, inflammatory mediators including the cytokines, interleukin-1β, tumor necrosis factors-α, interferon-γ and chemokines (CCL2 and CXCL8); matrix metalloproteinases (MMP2 and MMP9); and lipid mediators including prostaglandin E2 and lysophosphatidic acid (LPA) have been reported to increase BBB permeability[187-189]. Many endogenous compounds modulate the BBB permeability are released during pathological conditions such as ischemia-reperfusion injury[190,191].

#### 1.5.2.1 Osmotic Disruption

From a drug delivery standpoint, the disruption of tight junctions has to be transient and reversible in order to limit the risk of brain trauma. One of the most established methods for transient disruption of the BBB is intracarotid infusion of a high concentration of mannitol solution. The exposure to hypertonic solution leads to shrinkage of brain endothelial cells and opening of the tight junctions of the BBB. This technique has been extensively studied and has progressed into clinic practice being used in treatment of brain tumors that have poor prognosis and limited chemotherapeutic response due to restricted BBB penetration[192-194]. Several clinical studies demonstrated the enhanced delivery efficacy for drugs such as bevacizumab and methotrexate using osmotic BBB disruption[195-198]. While mannitol disruption technique is promising to deliver drug to the brain, there is a correlation between brain toxicity and the duration of BBB disruption. Mannitol-induced opening of BBB can last up to 4 to 6 hours depends on the type of animal model used[199]. Long recovery periods associated with the disruption allows immune cells as well as small and large molecules to enter the CNS. Water accompanied with cells and molecules induces a transient increase in intra-cranial pressure. These adverse effects are the major concern for brain tumor treatment[200]. As a result, several other chemical disruption methods with a shorter window of opening have been proposed.

#### 1.5.2.2 Activation of Receptors on Brain Microvasculature

Bradykinin and its analog RMP-7 (also called Cereport) bind to bradykinin receptors on brain endothelial cells leading to increased permeability across the BBB via disruption of the tight junctions. In contrast of osmotic disruption, the window of opening by bradykinin can only last 20min. Intravenous injection of RMP-7 enhanced accumulation of carboplatin in rat brain tumour tissue[201,202]. Although several *in vivo* and uncontrolled phase II studies of RMP-7 showed

very promising results, a randomized, double blind, placebo controlled phase II study of RMP-7 in combination with carboplatin failed to demonstrate clinical benefit for recurrent malignant glioma[203]. The potential reason for the negative results might be the low dose of RMP-7 or individual differences in expression of bradykinin B2 receptor in glioma patients; or tachyphylaxis to bradykinin receptor-induced effects on BBB permeability occurring within minutes following the continuous or multiple administrations of the compound[204].

Another agent to modulate tight junction permeability for BBB disruption is lysophosphatidic acid (LPA). Lysophosphatidic acid is capable of producing a variety of responses in mammalian cells by binding to receptors on the surface of plasma membrane and initiating their response through G-protein coupled receptor (GPCR) signaling pathways. There are currently at least 6 different types of LPA receptors (LPAR1-LPAR6)[205,206]. Within the brain, LPAR1 is the most highly expressed; although LPAR2 and LPAR3 are also present[205]. Recent studies by On et al., 2013 demonstrated that intravenous injections of LPA produced dose-dependent disruption of BBB integrity[192]. Modulation of BBB permeability with LPA was rapid in onset (within 3 minutes) and short in duration, with complete restoration of BBB integrity observed within 20 minutes[192]. Furthermore, disruption of the BBB by LPA promote an increased paracellular diffusion route through altered tight junction between the brain endothelial cells[192]. There are several advantages to targeting LPA receptors for pharmacological modulation of BBB permeability. One is the fast onset of BBB disruption observed following LPA exposure and the relatively short time course for restoration of BBB integrity. A second advantage is the wide range of molecules that could be delivered with this approach. Additionally, unlike RMP-7 that appears to have non-uniform disruption of BBB, LPA produced similar magnitudes of BBB opening throughout all areas of the brain examined[192]. While there are multiple LPA receptors

expressed within the brain microvasculature, there is the possibility that targeting selected LPA receptors with more selective pharmacological agents would further refine the extent of BBB modulation. Thus there is reason to be guardedly optimistic about the potential for modulation of BBB permeability through phospholipid receptors on the brain microvasculature.

#### 1.5.2.3 Ultrasound Disruption

Besides chemical disruption of the BBB, focused ultrasound combined with circulating microbubbles presents a physical disruption method that has gained favor in the past decade. This method can be achieved by IV injection of microbubbles that consist of semi-rigid lipid or albumin shells that encapsulate a gas followed by application of a focused ultrasound field[207]. The size of microbubbles can range from 1 to 10 micron. Under an ultrasound field, microbubbles oscillate and interact with vessel endothelium causing BBB disruption through widening of tight junctions and activation of transcellular mechanisms[208]. This technique is non-invasive and showed no apparent neuronal damage[209]. The BBB disruption occurred immediately following the ultrasound. Similar to osmotic disruption, the opening window of ultrasound disruption is about 6 hours[210,211].

The integration of nanomedicine and ultrasound to enhance and monitor delivery of multifunctional NPs to the brain was first published in 2010. Liu et al., 2010 combined the use of focused ultrasound and magnetic targeting to synergistically deliver therapeutic IONPs across the BBB[212]. This technique can be extended to other types of NPs such as gold and polyer based NPs[213,214]. For example, gold nanoparticles were found in perivascular and intraparenchymal regions in the brain following ultrasound disruption[215]. Studies demonstrated the feasibility of using gold nanoparticle as contrast agent for photoacoustic imaging to quantitatively monitor focused-ultrasound induced BBB opening in a rat model[216]. It was shown that MRI guided

transcranial-focused ultrasound can be used to open the BBB to allow entry of gold nanoparticles used for imaging of brain tumor margin[217]. Fan et al., 2013 proposed injection of IONPs and doxorubicin containing microbubbles and followed by ultrasound disruption method. Combined with magnetic targeting, IONPs deposition in tumor area was greatly increased[218]. While ultrasound certainly holds promise in delivering NPs across the BBB, the efficiency of such approach has not been determined. The efficiency of NP delivery using ultrasound disruption of the BBB in a normal animal model is also lacking and needed to better understand and further optimize the parameters of ultrasound for applications in CNS related pathologies.

## 1.6 Statement of the Problem

The blood-brain barrier that restricts drug molecules from entering the brain remains a major challenge to the development of drugs targeting brain disorders. Many therapeutic agents are ineffective in treatment of brain disorders due to poor BBB permeability. Effective treatment of brain disorders requires a focus on improving drug permeability across the BBB. Indeed, the clinical failure of many potential effective therapeutic agents is often not due to a lack of drug efficacy at the target site, but rather to shortcomings in the method by which the drug is delivered.

The research objective of the current dissertation is to identify safe and effective approaches for delivery of IONPs to the brain. It is hypothesized that transient disruption of the BBB combined with the application of a magnetic field, a process we have termed "Magnetic Field Enhanced Covective Diffusion (MFECD) can be used to enhance IONPs penetration in brain. Testing of this hypothesis requires identification of suitable IONP properties for utilizing MFECD, as well as determination of the biocompatibility of this approach.

The main objectives are:

1) To investigate the effect of surface charge and magnetic field on toxicity and uptake of IONPs in various brain related cell cultures.
2) To examine the use of an external magnetic field in combination with disruption of tight junctions to enhance the permeability of IONPs across an *in vitro* model of the BBB.
3) To determine pharmacokinetic properties of IONPs and capability of using LPA to disrupt the tight junction to allow IONPs to enter the brain.

4) To examine the effect of nanoparticle shape in regulating preferential uptake in endothelial cells compared to epithelial cells.

This study has important implications in nanoparticle based drug delivery in the treatment of different brain disorders. Our strategy of delivering nanoparticles into the brain has broad applicability. MFECD approach has the potential for efficient, targeted and safe delivery to the brain.

# Chapter 2 Characterization of cellular uptake and toxicity of aminosilane-coated iron oxide nanoparticles with different charges in central nervous system-relevant cell culture models

This chapter was published: Sun Z, Yathindranath V, Worden M, Thliveris JA, Chu S, Parkinson FE, Hegmann T, Miller DW. Characterization of cellular uptake and toxicity of aminosilane-coated iron oxide nanoparticles with different charges in central nervous system-relevant cell culture models. Int J Nanomedicine 2013;8:961-70. Zhizhi Sun performed cell culture, uptake of IONPs, quantification of IONPs, toxicity studies, and wrote the manuscript. Vinith Yathindranath and Matthew Worden carried out the synthesis and characterization of IONPs. James A. Thliveris performed electron microscopy analysis. Stephanie Chu isolated primary neuron and astrocytes from mice.

# 2.1 Introduction

Iron oxide nanoparticles (IONPs) have been proposed for various biomedical applications targeting the brain, including cell labeling[219], cancer hyperthermia,[220] and drug delivery[221]. Due to their superparamagnetic properties, IONPs as potential drug carriers offer the additional advantages of being traceable within the body, using magnetic resonance imaging (MRI), as well as being targetable to selected tissues with application of magnetic fields. The latter property is of particular interest to overcome obstacles, such as off-target toxicity due to accumulation of nanoparticles in nontarget tissue and suboptimal therapeutic response due to inadequate concentrations of nanoparticles at the target site. However, a major liability in using uncoated IONPs is the tendency for aggregation when placed in an aqueous environment. Furthermore, these aggregation problems observed with uncoated IONPs are accentuated in the presence of an external magnetic field[7]. In addition, uncoated IONPs lack functional groups on the surface of the nanoparticles that limit the extent to which surface modifications can be made to enhance cellular uptake or colloidal drug stability. Thus, surface modification of IONPs is necessary to prevent aggregation and allow the addition of specific functionalities to IONPs, including polymer coating, ligand-targeting specific protein, and fluorescent dye.

As central nervous system (CNS) applications for IONP drug delivery and imaging platforms are of growing interest, the potential toxicity of these nanoparticles in the CNS is a concern. High levels of iron have been found in autopsy section from patients with neurodegenerative disease, for example, Alzheimer's disease, Huntington's disease, and Parkinson's disease[222,223], leading to the suggestion that elevated iron concentrations within the brain contribute to the development of neurodegenerative disease. However, it is not clear whether the imbalanced iron homeostasis in the brain is the cause of the disease state or the

consequence of the disease process[224]. Similar arguments can be made about the current debate concerning beta amyloid plaques being an important component of Alzheimer's disease or a late stage disease marker. Such issues are inherently difficult to assess.

The use of IONPs to track and monitor grafted stem cells during stroke and traumatic brain injury and image various inflammatory CNS pathologies in both preclinical and clinical trials speaks to the general safety profile[225,226]. However, the amount of IONPs actually delivered to the brain is much reduced in comparison to applications involving CNS drug delivery. Ultimately, toxicity will likely be dependent on both the amount of IONPs in the brain and the composition of the IONP. Maghemite ($Fe_2O_3$) and magnetite ($Fe_3O_4$) are the most common core components of IONPs. Exposure to these core components could lead to the production of free radicals via Fenton and/or Haber–Weiss reactions[25]. Oxidative toxicity associated with both maghemite and magnetite species of IONPs has been reported[30,227]. It has been shown that the generation of reactive oxygen species and increased oxidative stress contribute to IONP toxicity in murine macrophages[228]. However, little is known about potential toxicity of IONPs in brain-specific cells. Studies by Rivet and colleagues reported neuronal cell death following exposure to polydimethylamine functionalized IONPs; however, other surface coatings of the IONPs, such as aminosilane and dextran coating, produced minimal toxicity[229]. Potential toxicity in other CNS cells, such as astroctyes and cerebral vascular endothelial cells, have not been evaluated. Information concerning IONP toxicity in astrocytes is of particular interest given the role of astrocytes in propagating inflammatory signals within the brain[230]. Furthermore, the variety of cell types found in the brain and the diversity of chemical constructs of IONPs make it difficult to translate toxicity data obtained in one particular cell type with a specific IONP composition.

Several surface modification methods using different silane constructs have been explored[231,232]. However, little is known about the effect of surface charge on biocompatibility of aminosilane-coated IONPs (AmS-IONPs) for brain-related drug delivery applications. To this end, the aim of this study was to investigate and compare the cytotoxicity and uptake profile of positive- and negative-charged AmS-IONPs in CNS- relevant cell culture models (ie, brain endothelial cells, neurons, and astrocytes). It was hypothesized that toxicity would be a function of cellular accumulation and the modifications that enhanced uptake, such as changes in surface charge or the application of a magnetic field, would directly affect toxicity. To test this we examined cellular accumulation and toxicity of AmS-IONPs with positive surface charges due to the presence of amine functional groups and COOH-AmS-IONPs with negative surface charges due to COOH functional groups in the presence and absence of a magnetic field.

## 2.2 Material and methods

### 2.2.1 Materials

All reagents were purchased from Sigma–Aldrich (St. Louis, MO) and cell culture reagents from Invitrogen Canada Inc (Burlington, ON, Canada) unless otherwise specified.

### 2.2.2 Nanoparticle synthesis and characterization

Iron-oxide nanoparticles were prepared under mild conditions of solvent and temperature as previously described[233]. Aminosilane coating of the IONPs was performed by rapidly adding 3-aminopropyltriethoxysilane (APTES, 17 mmol) to the IONPs in a reaction vessel and stirring continuously overnight at room temperature. The crude product was purified by dialysis (molecular weight cut-off 30,000) against deionzed (DI) water over 48 hours and was stored in DI water until further studies or chemical modifications. The resulting AmS-IONPs had a magnetite core and aminosilane outer shell with free amine functional groups. The COOH-AmS-IONPs were prepared by one additional step in which bromoacetic acid (BAA, dissolved in DI water) was titrated dropwise into the AmS-IONPs dispersion, followed by mechanical stirring at room temperature overnight. This resulted in the displacement of bromide groups on the α-carbon of BAA by amine functional groups of AmS-IONPs. Excess BAA was then removed by dialysis to yield COOH-AmS-IONPs with negatively charged surface properties. Both AmS-IONP and COOH-AmS-IONP compositions formed colloidal dispersions in water that were stable over at least a 2-month period. Hydrodynamic diameter and zeta potential of the IONP dispersions were measured using a Nano-partica SZ-100 series instrument (Horiba Scientific, Kyoto, Japan) with a diode-pumped solid-state (DPSS) 532 nm, 10 mW Class 1 laser, real refractive index of 2.42. The medium viscosity at 20°C was 1.002 cp. The dielectric constant was 80.100. The dielectric constant is 80.100. The scattering angle in both cases was set at 90°.

### 2.2.3 Cell culture

A mouse brain-derived microvessel endothelial cell line, bEnd.3 (American type tissue culture collection, Manassas, VA), was used as a cell culture model of the blood–brain barrier (BBB). The bEnd.3 cells (passage number 15–30) were cultured in Dulbecco's Modified Eagle Medium (DMEM) (Hyclone, Logan, UT) supplemented with 10% heat-inactivated fetal bovine serum (FBS; Hyclone), 50 U/mL penicillin and streptomycin (MP Biomedicals, Solon, OH) at 37°C and 5% $CO_2$. Cells were expanded in T-75 tissue culture flasks and seeded at $2 \times 10^4$ cells per $cm^2$ on six- or twelve-well plates for uptake and cytotoxicity studies, respectively. Culture medium was changed every 2 days. All experiments were performed on confluent monolayers (typically 4–5 days post seeding). Primary neurons and astrocytes were isolated from cortices of wild-type mice (CD1 neuron and C57BL6 astrocyte) as described previously[234]. Isolated neurons were plated at 15,000 cells/$cm^2$ on six- or twelve-well plates coated with poly-D-lysine with neurobasal media supplemented with B-27. Astrocytes were seeded at 50,000 cells/$cm^2$ on six- or twelve-well plates in DMEM-F12 media containing 10% FBS. Neurons were used between 11 and 15 days in culture, while astrocytes were used between 7 and 15 days in culture.

### 2.2.4 Cellular uptake of IONP compositions

Confluent monolayers of bEnd.3 cells grown on six-well culture plates (Costar, Lowell, MA) were treated with culture media containing either positively or negatively charged aminosilane-coated IONP compositions (1 μg/mL–50 μg/mL of Fe). After treatment with IONPs, cells were placed in a humidified $CO_2$ incubator maintained at 37°C. At various time points (0–5 hours), the IONP solutions were removed and the cell monolayers were washed 3X with ice cold phosphate-buffered saline (PBS) to remove unbound nanoparticles. Cells were lysed by the addition of 500 μL of 0.2 N NaOH, and IONP content was determined based on the ferrozine

assay described below. Cellular accumulation was examined in both the presence and absence of a static magnetic field created by placing the cells over a platform containing cylindrical rare earth magnets (19 mm diameter, 3 mm height) (Lee Valley, Winnipeg, MB, Canada). Cells remained in the magnetic field for the duration of the experiment. Cellular accumulation in astrocyte and neuronal cell cultures were performed under similar conditions except that the COOH-AmS-IONP accumulation in primary neuronal cultures was obtained by subtracting the amount of COOH-AmS-IONP adsorbed to the poly-D-lysine-coated plates without cells. This was necessary to account for the potential interaction of COOH-AmS-IONPs with the poly-D-lysine coating on the plates.

### 2.2.5 Cell viability studies

Cells were grown in twelve-well plates (Costar, Lowell, MA) and treated with various concentrations (0.1–224 μg/mL) of AmS-IONPs or COOH-AmS-IONPs for 24 hours at 37°C. Cell viability was determined using the 3-(4,5-dimethylthiazol-2-yl)-2,5-diphenyltetrazolium bromide (MTT) assay as previously reported[233]. Briefly, MTT dye (5 mg/mL in PBS) was added to each well and incubated for 3 hours at 37°C. Cells were solubilized in dimethylsulfoxide, and the formazan product resulting from mitochondrial metabolism in viable cells was measured by absorbance at 567 nm using a Synergy HT plate reader (BioTek, Winooski, VT). Absorbance readings following IONP exposure with and without magnetic field to that in cells receiving only media (control) were compared. Cell viability was expressed as a percentage of the absorbance levels observed in the control cells.

### 2.2.6 Analytical assay for measuring IONPs

Quantitative determination of IONP content in cell and media samples was performed using the ferrozine assay. As the ferrozine assay is an absorbance-based assay for determining

soluble iron concentrations, IONPs in the cell lysate and media samples were first solubilized by adding 500 μL of concentrated HCl (~12 M) to 500 μL of cell lysate or media samples. This mixture was incubated for 1 hour at room temperature with gentle shaking and then neutralized with 500 μL of 12 M NaOH. Once the samples were neutralized, 120 μL of hydroxylamine hydrochloride (2.8 M) in 4 M HCl was added and the samples incubated for 60 minutes at room temperature with gentle shaking. Following this incubation, 50 μL of 10 M ammonium acetate solution (pH 9.5) and 300 μL of 10 mM ferrozine in 0.1 M ammion acetate solution was added to each sample. Absorbance was measured at 562 nm using a Synergy HT plate reader. Quantitative assessment of IONP concentration was based on a standard curve prepared using 1000 ppm iron atomic absorption standard (Fisher Scientific, Ottawa, ON, Canada). Samples from the cell lysates were normalized for protein content using the bicinchoninic acid assay kit (Pierce, Rockford, IL).

### 2.2.7 Electron microscopy

The cellular localization of AmS-IONP and COOH-AmS-IONP compositions was examined using transmission electron microscopy. For these studies, bEnd.3 cells were incubated with IONPs at a 50 μg/mL concentration in media for 2 hours. After incubation cells were washed 3X with PBS and collected using 0.25% trypsin EDTA (Hyclone). After centrifugation the cell pellets where fixed in 3% glutaraldehyde in 0.1 M phosphate buffer (pH 7.3), followed by postfixation in 1% osmium tetroxide in 0.1 M phosphate buffer (pH 7.3). Cells were then dehydrated and embedded in Epon 812 using standard techniques[235]. Thin sections were stained with uranyl acetate and lead citrate, viewed, and photographed in a Philips CM 10 electron microscope (FEI, Hillsboro, OR, USA). In order to eliminate observer bias, sections were examined without foreknowledge of their source.

### 2.2.8 Statistical analysis

All data were expressed as mean ± standard error of the mean. All values were obtained from at least three independent experiments. Statistical significance was evaluated using one-way analysis of variance followed by post hoc comparison of the means using the Fisher's least significant difference test.

# 2.3 Results

## 2.3.1 Physicochemical characterization of IONPs

The properties and schematic representation of the IONPs used in the present study are provided in Figure 2.1. The uncoated IONP form a quasi-spherical (polyhedral) nanoparticle, which is maintained following aminosilane coating[233]. The average hydrodynamic size of both the AmS-IONP and COOH-AmS-IONP compositions were approximately 27 nm as determined using dynamic light scattering in water (Figure 2.1). While the sizes of the IONPs were similar, surface charge characteristics were substantially different, with the AmS-IONPs having a zeta potential of +23.9 mV compared to the –17.0 mV observed in the COOH-AmS-IONP compositions.

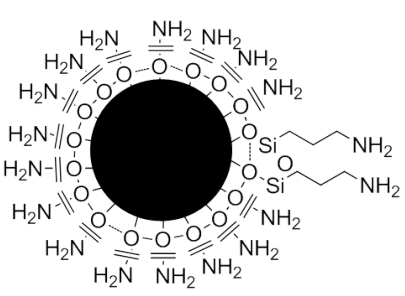

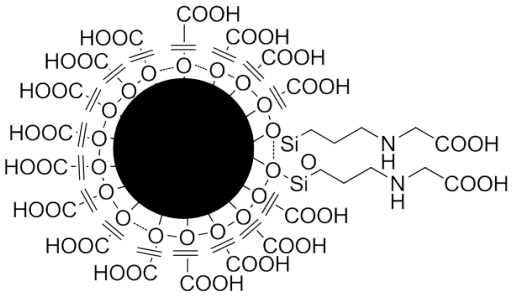

| | AmS-IONP | COOH-AmS-IONP |
|---|---|---|
| Charge | +23.9 ± 1.2mV | -17.0± 3.9mV |
| Size | 26.95 ± 3.2 nm | 26.8 ± 8.9nm |

**Figure 2.1 Schematic of positively charged (AmS-IONPs) and negatively charged (COOH-AmS-IONPs) nanoparticles and their physical properties. Measurements were performed in triplicate samples using a Nano-partica SZ-100 series instrument from Horiba. Values represent the mean ± standard error of the mean (n = 3).**

## 2.3.2 Cytotoxicity of AmS-IONPs

The MTT assay, which measures mitochondrial metabolic activity, is a common method used to measure toxicity mediated by nanoparticles. In these experiments the viability of bEnd.3 cells, mouse primary astrocytes, and neurons was evaluated after 24 hours incubation in the absence and presence of a magnetic field (Figure 2.2). No significant toxicity was observed in bEnd.3 cells at any concentration examined. Significant toxicity resulting in a 25% reduction in cell viability was observed in astrocytes at the highest concentration (224 μg/mL) of AmS-IONPs examined but only in the presence of a magnetic field (Figure 2.2). Neurons displayed an even greater decrease in viability (approximately 50%) following exposure to 224 μg/mL AmS-IONPs, and this was observed with or without the presence of a magnetic field (Figure 2.2).

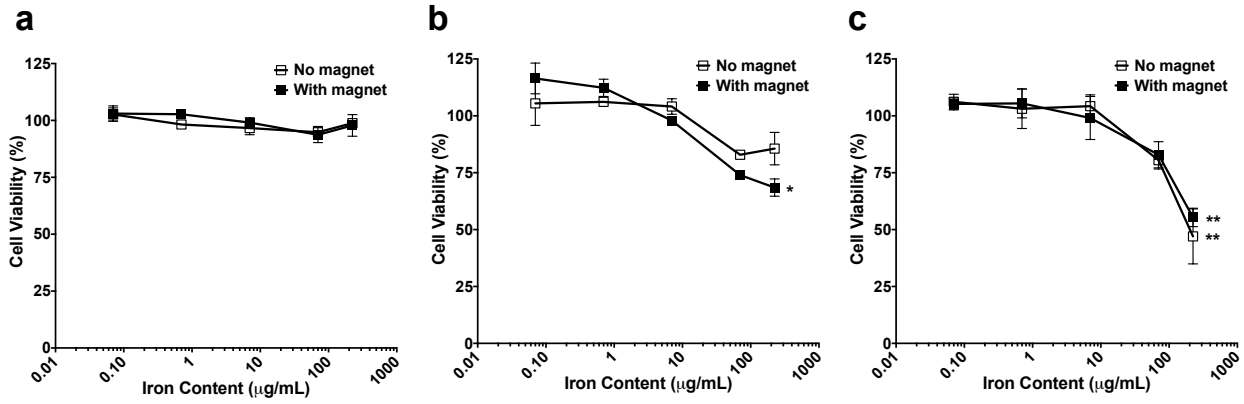


**Figure 2.2 bEnd.3 cell (a), astrocyte (b), and neuron (c) viability following a 24-hour exposure to various concentrations of AmS-IONPs. Iron content was used to normalize the concentration of various formulated IONPs. Values represent the mean ± standard error of the mean of three samples per treatment group. * indicates 0.01 < P < 0.05 compared to control, ** indicates P < 0.01.**

## 2.3.3 Cytotoxicity of COOH-AmS-IONPs

While there was no toxicity observed in the endothelial cell culture model at any concentration examined, exposure of COOH-AmS-IONPs exhibited significant toxicity at high concentrations (ie, >100 μg/mL) for astrocytes and neurons (Figure 2.3). Significant decreases in cell viability in astrocyte cultures were observed at concentrations of COOH-AmS-IONP of 100

μg/mL compared with the control group ($P < 0.001$). Further decreases in viability were observed at concentrations of 150 μg/mL with only 65% of astrocytes being viable after 24 hours of exposure to COOH-AmS-IONP. The presence of a magnetic field increased cytotoxicity to the COOH-AmS-IONP at higher concentrations (ie, >100 μg/mL) in astrocytes (Figure 2.3). In contrast, negatively charged COOH-AmS-IONP produced no toxicity in cultured neurons at concentrations below 150 μg/mL. However, at concentrations above this level an approximately 25% loss of viability was observed. Statistical significant decreases in viability were observed following application of a magnetic field at the 100 μg/mL concentration of COOH-AmS-IONPs compared to the control group; however, there was no significant difference in viability without a magnetic field at the same concentration.

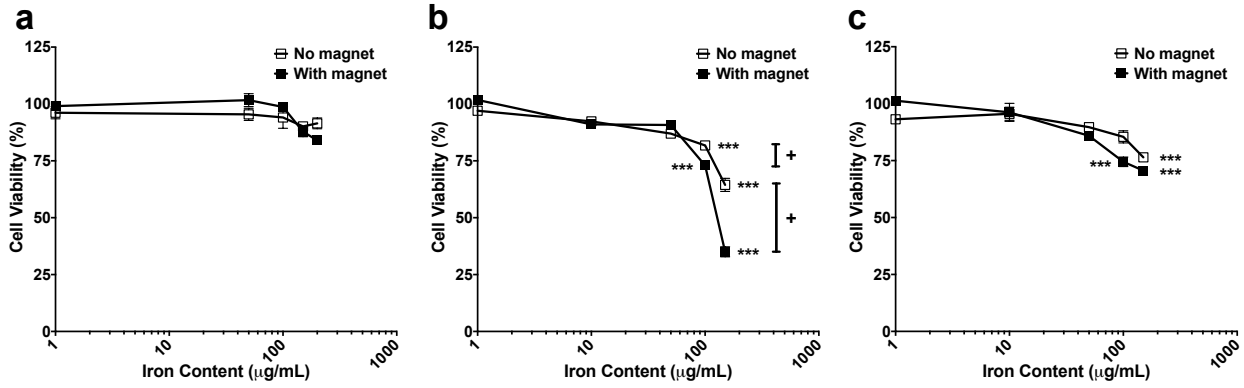


**Figure 2.3 MTT assay of COOH-AmS-IONPs to bEnd.3 cells (a), astrocytes (b), and neurons (c). Iron content was used to normalize the concentration of various formulated IONPs. Values represent the mean ± standard error of the mean of three samples per treatment group. *** indicates P < 0.001 compared to control; + indicates P < 0.05 compared to the same concentration without a magnet.**

### 2.3.4 Cellular uptake of AmS-IONPs and COOH-AmS-IONPs

The initial parameters for examining cellular accumulation of the aminosilane-coated IONPs were determined in bEnd.3 cell monolayers. Accumulation of AmS-IONPs in bEnd.3 cells was both time and concentration dependent, with maximal uptake observed at concentrations of 10

μg /mL or greater and at the 5 hour time period (Figure 2.4a). As accumulation was maximal at concentrations of 10 μg/mL or greater at all time points examined, subsequent accumulation studies were performed at concentrations at or below 10 μg/mL. Cellular accumulation of AmS-IONPs was also dependent on temperature, with much higher accumulation observed at 37°C compared to 4°C (Figure 2.4b,c). Application of a magnetic field enhanced accumulation of AmS-IONPs at all concentrations examined and at both 37°C and 4°C (Figure 2.4b,c). The uptake difference between 37°C and 4°C upon exposure to a magnetic field was also increased at various concentrations.

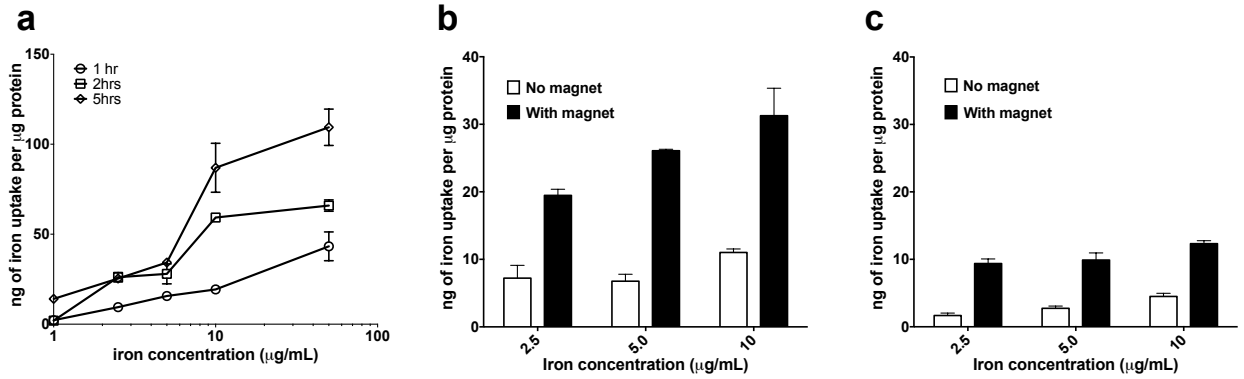


**Figure 2.4 Cellular uptake of AmS-IONPs in bEnd.3 cells. Amount of iron accumulation in the cells normalized to protein in time- and concentration-dependent manner (a). The cells were incubated with AmS-IONPs for 1.5 hours at 37°C (b) or 4°C (c). Values represent the mean ± standard error of the mean of three samples per treatment group.**

A similar cellular accumulation profile for AmS-IONP was observed in cultured bEnd.3 and primary cultured astrocytes and neurons (Figure 2.5). Application of a magnetic field enhanced the amount of cell-associated AmS-IONPs at all concentrations examined. The effects of a magnetic field were most apparent in the 5 μg/mL treatment group in bEnd.3 cells (Figure 2.5a). In contrast, the effects of a magnetic field were most apparent in the 10 μg/mL treatment group for neurons and 2.5 μg/mL treatment group for astrocytes (Figure 2.5b,c). There was a threefold increase in cellular accumulation of AmS-IONPs in astrocytes compared to neurons.

The rank order of accumulation with the AmS-IONPs was astrocytes > endothelial cells > neurons.

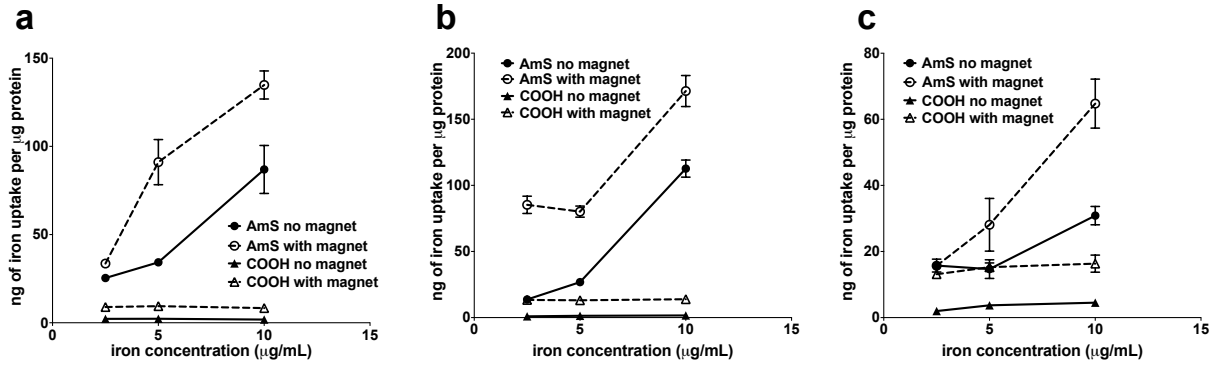


**Figure 2.5 Cellular uptake of AmS-IONPs and COOH-AmS-IONPs in bEnd.3 cells (a), astrocytes (b), and neurons (c) at 37°C. Values represent the mean ± standard error of the mean of three samples per treatment group.**

Compared to the AmS-IONP uptake profile, cellular accumulation of COOH-AmS-IONPs was significantly reduced at all concentrations examined. In contrast to the AmS-IONP compositions, which displayed concentration-dependent uptake, the accumulation of COOH-AmS-IONPs was similar at all concentrations examined. The negatively charged COOH-AmS-IONPs showed the same low uptake profile in both neurons and astrocytes, with less than 5 ng of iron per μg of protein accumulation in the cells. Magnetic field exposure increased uptake of COOH-AmS-IONPs to 15 ng of iron per μg of protein. Electron micrographs of bEnd.3 cells further support the differences in cellular uptake of the various IONP compositions (Figure 2.6). While bEnd.3 cells exposed to AmS-IONPs displayed many intracellular vesicles containing nanoparticles, cells exposed to COOH-IONPs had substantially fewer intracellular organelles containing nanoparticles (Figure 2.6).

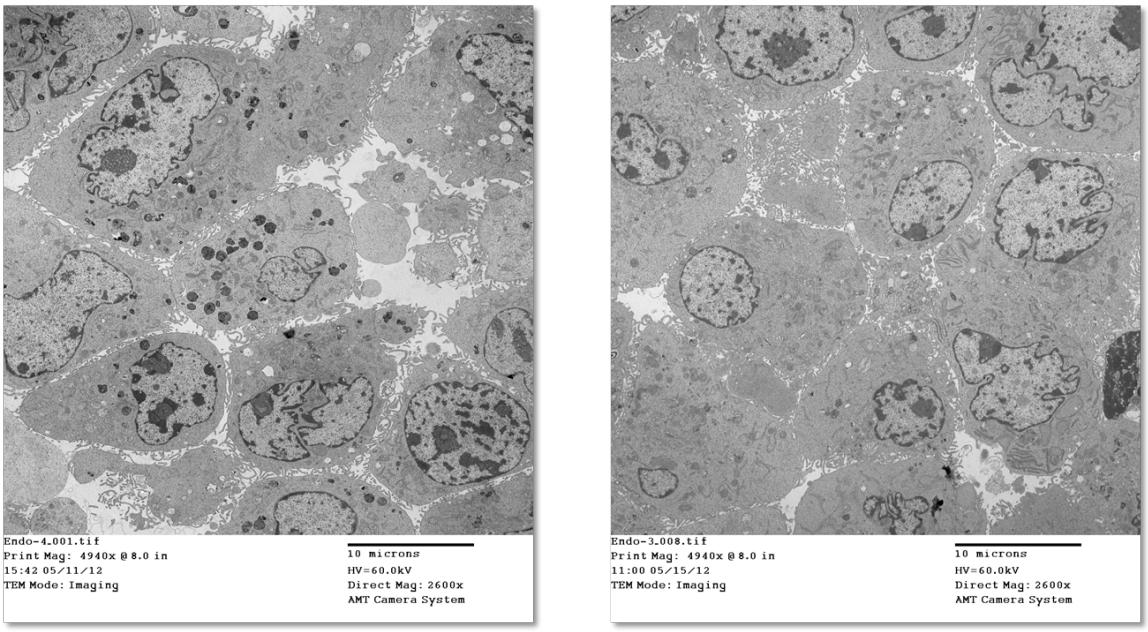


**Figure 2.6 TEM images of bEnd.3 cells that were incubated with AmS-IONPs (left) or COOH-AmS-IONPs (right). Electron-dense particles are visible in intracellular vesicles.**

## 2.4 Disscussion

This study is concerned with the biocompatibility of AmS-IONPs formulations and the influence that surface charge has on both cellular accumulation and toxicity in cells within the brain. While additional nanoparticle modifications will undoubtedly be required for enhancing brain delivery and drug release, AmS- and COOH-AmS-IONPs represent the building blocks from which a variety of functionalized IONP compositions will be created. Thus, establishing the cellular uptake and toxicity of AmS- and COOH-AmS-IONPs represents a baseline from which additional surface modifications can be evaluated for potential CNS drug delivery applications. As the IONPs in the present study have the same core and aminosilane coating but are at two different ends of the surface charge spectrum, these studies provide an excellent opportunity to probe the influence of surface charge on cell accumulation and toxicity in brain-relevant cells.

There are several different strategies that have been examined for enhancing BBB permeability of nanoparticles. One involves various surface modifications using specific ligands to overcome the BBB by receptor-mediated transcytosis[236,237]. For example, apolipoprotein E-modified human serum albumin nanoparticles cross the BBB via low-density lipoprotein-mediated endocytosis[238]. Another strategy involves magnetic targeting of long circulating magnetic nanoparticles and disruption of the BBB[239]. For example, magnetic targeting and the BBB disruption by focused ultrasound synergistically enhanced delivery of magnetic nanoparticles into the brain[212]. We demonstrated that the positively charged AmS-IONPs favor an endocytosis pathway and therefore may be useful starting material for combining with ligands to enhance the transcytosis route. In contrast, the negatively charged COOH-AmS-IONPs showed minimal uptake by cells, so these particles, and derivatives thereof, may be good candidates for magnetic targeting through a transiently disrupted BBB.

The results of the present study indicate that both AmS- and COOH-AmS-IONPs were well tolerated by neurons, astrocytes, and brain microvessel endothelial cells. Toxicity, when present, was only observed at relatively high concentrations. This is different from other metal-based nanoparticles, including zinc and titanium oxide nanoparticles, that have substantial toxicity in neurons and astrocytes[240-242]. Compared to these other metal nanoparticles, the IONP-based compositions used in the present study appear to have good biocompatibility with concentrations required to produce toxicity being rather large and not likely to be obtained in vivo or in clinical applications[30,243].

We had hypothesized that the extent of nanoparticle accumulation in cells would have important implications in the extent of potential toxicity produced. In the current study there was an approximately threefold increase in the accumulation of AmS-IONPs in astrocytes and bEnd.3 cells compared to neurons. However, of the three cell types examined, neurons showed the greatest toxicity to the AmS-IONP compositions. Conversely, cellular accumulation of COOH-AmS-IONPs was substantially less than that observed with AmS-IONPs in astrocytes and yet the COOH-AmS-IONP produced greater toxicity than the AmS-IONPs. Taken together, these observations suggest it may be the surface coating that is the primary factor in determining the toxicity response observed.

In support of the surface coating and its influence on toxicity, it has been noted that cationic hydrogels produce significant decreases in neuron cell viability, whereas neutral hydrogels show no toxicity[244]. This is consistent with the findings in the present study that positively charged surface coatings affect neuronal function to a greater extent than the negatively charged nanoparticles. While the exact mechanism explaining the toxicity observed with high concentrations of negatively charged COOH-AmS-IONPs in astrocytes is unknown, it

may be related to the potential responses to reactive oxygen species in astrocytes and neurons. Studies using a hippocampal slice culture model reported astrocytes exhibited a significantly higher sensitivity to reactive oxygen species than neurons[245]. The recent studies of Haase and colleagues support this possibility as astrocytes were found to be more sensitive to silver oxide nanoparticles compared to neurons due to the oxidative stress responses produced in the astrocytes[246].

Previous studies using a human neuroblastoma cell line reported 60% cell viability at a 2.25 mM concentration of AmS-IONPs[247]. The toxicity was correlated with the upregulation of genes associated with cell growth arrest and apoptosis in the case of AmS-IONPs, while genes associated with cell proliferation response were upregulated upon negatively charged IONPs due to its reactive oxygen species generation properties[247]. The present study used primary cultured neurons and astrocytes to more accurately reflect potential toxicity within the brain. We found that both AmS- and COOH-AmS-IONPs were well tolerated in primary neuron and astrocyte preparations, with toxicity observed only at high concentrations. Studies to identify potential cellular pathways influenced by IONP exposure and potential cell-specific differences are currently ongoing.

As the brain endothelial cells that form the BBB have restricted paracellular permeability under normal conditions, the cellular accumulation of the AmS- and COOH-AmS-IONPs has important implications in the potential passage of IONPs across the BBB. Based on the present study, there is a clear preference for positively charged AmS-IONPs in regards to both attachment to the plasma membrane and vesicular internalization within brain endothelial cells. The positively charged AmS-IONPs displayed a higher rate of endocytic activity, which was concentration dependent. In this regard our results are in accordance with a previous report

conducted using various mammalian cell lines[53]. The present studies showing increased cellular accumulation of the positively charged AmS-IONP are consistent with the enhanced adsorptive endocytosis observed following cationization of albumin in brain endothelial cells[248]. The negatively charged COOH-AmS-IONPs were less likely to interact with the cell membrane, resulting in decreased uptake and a lack of concentration dependency. Such characteristics are consistent with nonspecific, fluid-phase, endocytosis mechanisms for the COOH-AmS-IONPs. Applying a magnetic field resulted in increased amounts of IONPs associated with the cells. This was expected as in the presence of a magnetic field the IONPs dispersed in the media will move toward a high-gradient magnetic field at the bottom of the culture plate, increasing the interactions with the cells. However, even in the presence of a magnetic field the cellular uptake of COOH-AmS-IONPs was fourfold less than AmS-IONPs in neurons and tenfold less in bEnd.3 cells and astrocytes.

Nanoparticles in contact with cells can either be adsorbed on the cellular membranes or internalized into membrane-bounded endocytic compartments[249]. Uptake studies in bEnd.3 cells performed both at 4°C and at 37°C allowed us to distinguish between the adsorbed and internalized AmS-IONPs. Because endocytosis processes are strongly temperature dependent and internalization of NPs was inhibited at 4°C[250], the amount of iron detected at 4°C represents AmS-IONPs adsorbed on the plasma membrane of the cell. Furthermore, the difference in the AmS-IONP uptake profile at 37°C and 4°C represents internalized NPs. Similar temperature-dependent uptake of IONPs has been reported in astrocytes[250]. Of note, the presence of a magnetic field greatly increased both intracellular and extracellular accumulation of IONPs, suggesting a nonspecific AmS-IONP interaction with the cell that may be exploited for drug delivery purpose. Such effects of a magnetic field on cellular accumulation of IONPs have been

reported in other cells and are postulated to be a result of the physical pulling of AmS-IONPs toward cell membranes down the magnetic gradient[251]. Studies to determine optimal magnetic field strength for both AmS-IONPs and COOH-AmS-IONPs are currently ongoing.

## 2.5 Conclusion

This study evaluated the toxicity and cellular accumulation of differently charged aminosilane-coated IONPs in brain endothelial cells, neurons, and astrocytes. There was no toxicity observed with either the positively charged AmS-IONPs or the negatively charged COOH-AmS-IONPs in cultured brain microvessel endothelial cells. High concentrations of positively charged AmS-IONPs displayed toxicity to neurons and the astrocytes appeared more vulnerable to the negatively charged COOH-AmS-IONPs. The IONP toxicity did not correlate with the magnitude of accumulation as the COOH-AmS-IONPs had the lowest accumulation in all cell types but caused greater toxicity in astrocytes than the AmS-IONP compositions. This suggests toxicity is dependent on surface coating more than the IONP core. AmS-IONPs displayed the highest cell accumulation in all cell types tested. Application of a magnetic field had a minimal impact on the cytotoxicity but significantly enhanced uptake of both IONP formulations in all cell types examined. These studies establish the baseline parameters for aminosilane-coated IONP uptake and biocompatibility and will help facilitate the design of more complex IONP compositions for CNS drug delivery applications.

# Chapter 3 Magnetic field enhanced convective diffusion (MFECD) of iron oxide nanoparticles in an osmotically disrupted cell culture model of the blood-brain barrier

This chapter was published: Sun Z, Worden M, Wroczynskyj Y, Yathindranath V, van Lierop J, Hegmann T, Miller DW. Magnetic field enhanced convective diffusion of iron oxide nanoparticles in an osmotically disrupted cell culture model of the blood-brain barrier. Int J Nanomedicine 2014;9:3013-26. Zhizhi Sun performed cell culture, uptake of IONPs, quantification of IONPs, permeability studies and wrote majority of the manuscript. IONP synthesis and characterization was carried out by Matthew Worden, Yaroslav Wroczynskyj, and Vinith Yathindranath.

# 3.1 Introduction

CNS drug candidates have the lowest approval rate compared to other drug categories during drug development process[252]. A principle challenge to develop CNS drugs is obtaining sufficient permeability across the BBB to achieve adequate therapeutic concentrations in the brain. The brain capillary endothelial layer is morphologically distinct compared to other vascular beds because it lacks fenestrations, has reduced pinocytic activity and contains complex tight junctions[253]. In addition to the restricted paracellular diffusion of solutes, the expression of P-gp, MRP, BCRP, and various other drug efflux transporters in brain microvessel endothelial cells limit the transcellular diffusion of a wide variety of solutes and drugs[160,254-256]. While it is generally accepted that large molecules have limited BBB permeability, smaller molecules also face restricted BBB permeability with an estimated 95% of traditional small molecule compounds in drug discovery libraries unable to penetrate the BBB in pharmacologically relevant amounts[257]. Therefore, the effective treatment of CNS diseases requires an understanding of both the pharmacological target and the BBB permeability properties of a drug.

The applications of IONPs as potential drug carriers have been explored actively over the last few years[218,258-261]. To date, the application of IONPs for imaging and therapeutic interventions of CNS disorders remains a great challenge. Under normal conditions, the permeability of IONPs across the BBB is restricted with little to no detectable penetration of IONPs reported with *in vitro* and *in vivo* models[221,262]. Indeed, the majority of studies reporting IONP delivery to the brain have been under conditions where the BBB is compromised, such as in brain tumor models where the EPR effect contributes to the accumulation of IONPs to tumors[263,264]. However, as the extent of BBB disruption observed in brain tumor models is

variable and dependent on the stage of tumor development[265], other methods of delivery to the brain are required

An additional concern with nanoparticles is distribution in non-target tissue. Non-specific uptake of IONPs in the body will lead to systemic distribution and potential toxicity. The reticuloendothelial system (RES) consists of monocytes and macrophages in the liver, spleen, and blood efficiently eliminate the majority of intravenously administered IONPs preventing delivery to the target tissue site. One way to circumvent this problem is to modify the surface chemistry of the IONPs as nanoparticle-cell interactions depend on the physiochemical properties of the NPs. Recently, we have established the biocompatibility and cell accumulation of both positively and negatively charged IONPs in a variety of different CNS relevant cell systems[266]. While these studies showed a high degree of biocompatibility with all cell types examined, there was a substantial difference in the cellular accumulation, with the positively charged IONPs having much greater uptake in brain microvessel endothelial cells compared to the negatively charged IONPs of similar size[266].

The present study extends these initial observations by evaluating the impact of IONP surface charge on permeability across an *in vitro* cell culture model of the BBB. Based on our previous study, it was hypothesized that negatively charged IONPs would favor paracellular diffusion routes while the positively charged IONPs would primarily undergo transcellular vesicular transport. Further, it was postulated that while the paracellular route would normally be insufficient to support IONP delivery, MFECD approach could be used to enhance BBB penetration.

## 3.2 Materials and methods

### 3.2.1 Materials

All chemical reagents were purchased from Sigma Aldrich (St. Louis, MO) and cell culture reagents from Invitrogen Canada Inc. (Burlington, ON) unless otherwise specified.

### 3.2.2 Nanoparticle synthesis and characterization

Iron oxide nanoparticles were prepared under mild conditions at room temperature as previously described[233]. Aminosilane coating of the IONPs was performed by rapidly adding 3-aminopropyltriethoxysilane (APTES, 17 mmol) to the IONPs in a reaction vessel and stirring continuously overnight at room temperature. The crude product was purified by dialysis (MWCO 30000) against deionized (DI) water over 48 hours and was stored in DI water until further studies or chemical modifications. The resulting AmS-IONPs had a magnetite ($Fe_3O_4$) core and aminosilane outer shell with free amine functional groups. The EDT-IONPs were prepared by adding N-(trimethoxysilylpropyl)ethylenediaminetriacetate trisodium salt (EDT, 3 mmol, from a solution concentration of 45% in water) (Gelest, Morrisville, PA) directly to a reaction vessel containing IONPs. The mixture was allowed to react overnight with stirring and the final product was purified by dialysis as described for AmS-IONPs. Both NPs are filtered through 0.2μm nylon filter before experiments.

The IONP size distribution in DI water was determined initially through photon correlation spectroscopy (PCS) at a fixed scattering angle (90°) using a Horiba Nano-Partica SZ-100 series instrument (Horiba Instruments Inc., Irvine, CA). The same instrument allowed for the assessment of particle surface charge (zeta potential) by the measurement of IONP electrophoretic mobilities using phase analysis light scattering. Further characterization of IONP hydrodynamic size distribution was performed by PCS using a Photocor Complex (Photocor

Instruments Inc., College Park, MD) allowing for measurements over a range of scattering angles.

### 3.2.3 Cell culture

A mouse brain derived microvessel endothelial cell line, bEnd.3 (American type tissue culture collection, Manassas, VA), was used as a cell culture model of the BBB. The bEnd.3 cells (passage number 30-50) were cultured in DMEM (Hyclone, Logan, UT) supplemented with 10% heat-inactivated fetal bovine serum (Hyclone, Logan, UT), 50 Units/mL penicillin and streptomycin (MP Biomedicals, Solon, OH) at 37°C and 5% $CO_2$. Cells were expanded in T-75 tissue culture flasks, and then passaged and seeded at $2x10^5$ cells per well on six well plates and six well inserts for uptake and permeability studies, respectively. Culture medium was changed every two days. All experiments were performed on confluent monolayers on typically day four or five post seeding.

### 3.2.4 Cellular Uptake of IONP compositions

Confluent monolayers of bEnd.3 cells grown on six well culture plates (Costar, Lowell, MA) were treated with culture media or culture media with 1.4M mannitol containing various IONP concentrations (2.5 μg/mL – 50 μg/mL of Fe). After treatment with IONPs, the cells were placed in a humidified $CO_2$ incubator maintained at 37°C. After five hours, the culture media was removed and the cell monolayers were washed three times with ice cold PBS to remove the unbound NPs. Cells were lysed with 500 μL of 0.2 M NaOH, and the IONP content was determined from the Ferrozine assay described previously[266]. Cellular accumulation was examined in both the presence and absence of a static magnetic field. For studies involving a magnetic field, the cells were placed over a platform containing commercial cylindrical rare-earth magnets (Nd-Fe-B, 19 mm diameter, 3 mm height). Under these conditions, the cell

monolayer was positioned approximately 1mm above the magnets (field strength of 0.13T). Cells with IONPs remained exposed to the magnetic field for the duration of the experiment.

### 3.2.5 Permeability studies

Permeability studies were performed on confluent monolayers of bEnd.3 cells grown on semi-permeable polycarbonate membrane inserts (3 μm pore size; 24 mm diameter) (Corning Incorporated, Corning, NY) and maintained with DMEM. Permeability was assessed by adding 1.5mL of 50 μg/mL of either AmS-IONPs or EDT-IONPs to the apical (luminal) compartment. Permeability studies were performed at 37°C in a $CO_2$ incubator in the presence and absence of a static magnetic field as described above. Under these conditions, the cell monolayer was positioned approximately 3 mm above the magnets (magnetic field strength of 0.06T). To determine the integrity of the cell monolayers, 70 000 molecular weight fluorescein labeled dextran (FDX; 250 μg/mL) (Life Technologies, Burlington, ON) was also added to the apical compartment of each monolayer at the beginning of the permeability study and its appearance in the basolateral compartment was determined using a Biotek Synergy HT plate reader (excitation 488 nm and emission 510 nm) (BioTek Instruments Inc., Winooski, VT). At various times, the IONP concentration in the basolateral compartment was determined by the Ferrozine assay. Quantitative assessments of IONP permeability were determined by the fraction of Fe in the basolateral compartment relative to the amount of Fe loaded in the apical compartment. The apparent permeability coefficients P for FDX and IONPs were calculated using the following equation:

$$P = \frac{\Delta Q/\Delta t}{AC_o}$$

Where $\Delta Q/\Delta t$ is the linear appearance rate of the compounds on the receiver, A is the membrane surface area, and $C_o$ is the initial concentration in the donor chamber.

In separate studies, permeability of the IONP compositions was examined in bEnd.3 monolayers in DMEM containing 1.4M mannitol to disrupt the tight junctions and reduce monolayer integrity.

### 3.2.6 Analytical assay for measuring IONPs

Quantitative determination of IONPs content in cell and media samples was performed using the Ferrozine assay[266]. As the Ferrozine assay is an absorbance based assay for determining ionic iron concentrations, IONPs in the cell lysate and media samples were first solubilized by adding 500 μL of concentrated HCl (~12M) to 500 μL of cell lysate or media samples. This mixture was incubated for one hour at room temperature with gentle shaking and then neutralized with 500 μL of 12M NaOH. Upon neutralization, 120 μL of hydroxylamine hydrochloride (2.8M) in 4M HCl was added and the samples were incubated for 60 minutes at room temperature with gentle shaking. Following this incubation, 50 μL of 10M ammonium acetate solution (pH 9.5) and 300 μL of 10mM ferrozine in 0.1M ammonium acetate solution was added to each sample. Absorbance was measured at 562 nm using a Synergy HT plate reader (BioTek, Winooski, VT). Quantitative assessment of IONPs concentration was based on a standard curve prepared using 1000 ppm iron atomic absorption standard (Fisher Scientific, Ottawa, ON). Samples from the cell lysates were normalized for protein content using BCA protein assay kit (Pierce, Rockford, IL).

### 3.2.7 Statistical analysis

All data were expressed as mean ± SEM. All values were obtained from at least three independent experiments. Statistical significance was evaluated using one-way ANOVA followed by post-hoc comparison of the means using the Fisher's least significant difference test.

# 3.3 Results

## 3.3.1 Physico-chemical characterization of IONPs

Characterization of AmS-IONPs by Transmission electron microscopy (TEM), X-ray powder diffraction (XRD), thermogravimetric analysis (TGA) and Fourier transform infrared spectroscopy (FTIR) spectroscopy have been recently published[267]. Specific data concerning EDT-IONPs can be found in the supplementary information. A schematic drawing of the IONPs used in the present study is provided in Figure 3.1. The mean hydrodynamic diameter of the AmS-IONPs and EDT-IONPs suspended in water were 25 ± 1 nm and 29 ± 1 nm, respectively, as determined by PCS at a fixed scattering angle (Figure 3.1). While the sizes of the IONPs were similar, surface charge characteristics were substantially different, with the AmS-IONP having a positive zeta potential of +21 ± 4 mV compared to -39 ± 3 mV observed with the EDT-IONP composition. As the AmS and EDT coated IONPs have effectively the same hydrodynamic size in DI water, the selected coatings provided a platform for analyzing the influence of surface charge in uptake and permeability in bEnd3 monolayers.

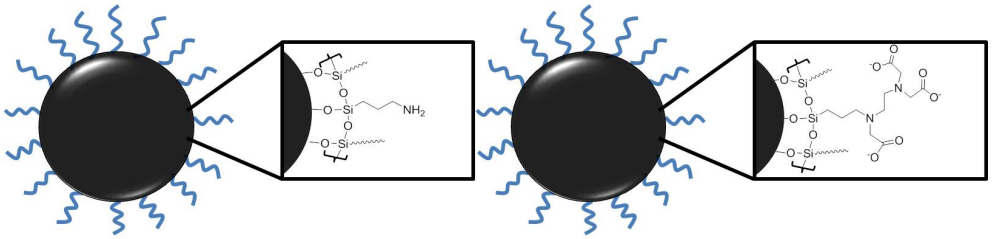

| | AmS-IONPs | EDT-IONPs |
|---|---|---|
| Charge | +21 ± 4 mV | -39 ± 3 mV |
| Size | 25 ± 1 nm | 29 ± 1 nm |

**Figure 3.1 Schematic drawing of the positively charged AmS-IONPs and negatively charged EDT-IONPs and their physical properties. Measurements were performed in triplicate samples using a Nano-partica SZ-100 series instrument from Horiba. Values represent the mean ± SEM (n=3).**

### 3.3.2 Permeability studies of AmS-IONPs and EDT-IONPs

Permeability of IONPs across an intact model of the BBB were assessed using confluent monolayers of mouse bEnd.3 cells grown on polycarbonate (PC) membrane inserts (3μm pore size) in the presence and absence of an external magnetic field. In the absence of IONPs, 2 and 5% of FDX-70000 crossed confluent bEnd.3 monolayers at 8- and 24-hour time points, respectively (Figures 3.2A and 3.2C). The resulting permeability coefficients for FDX-70000 in intact bEnd.3 cells monolayer (Table 1) is consistent with literature reports[268]. Treatment of the monolayers with either AmS-IONPs or EDT-IONPs (50 μg/ml) had no effect on the magnitude of FDX-70000 permeability, suggesting that neither of the nanoparticle preparations compromised monolayer integrity (Figures 3.2A and 3.2C; Table 1). In the intact cell monolayers, the permeability of AmS-IONPs was minimal with less than 1% of the AmS-IONPs in the basolateral compartment after 24 hours (Figure 3.2B). The presence of a magnetic field did not enhance the permeability of the AmS-IONPs in the intact bEnd.3 monolayers. A similar low permeability profile was observed with EDT-IONPs in either the presence or absence of an external magnetic field (Figure 3.2D).

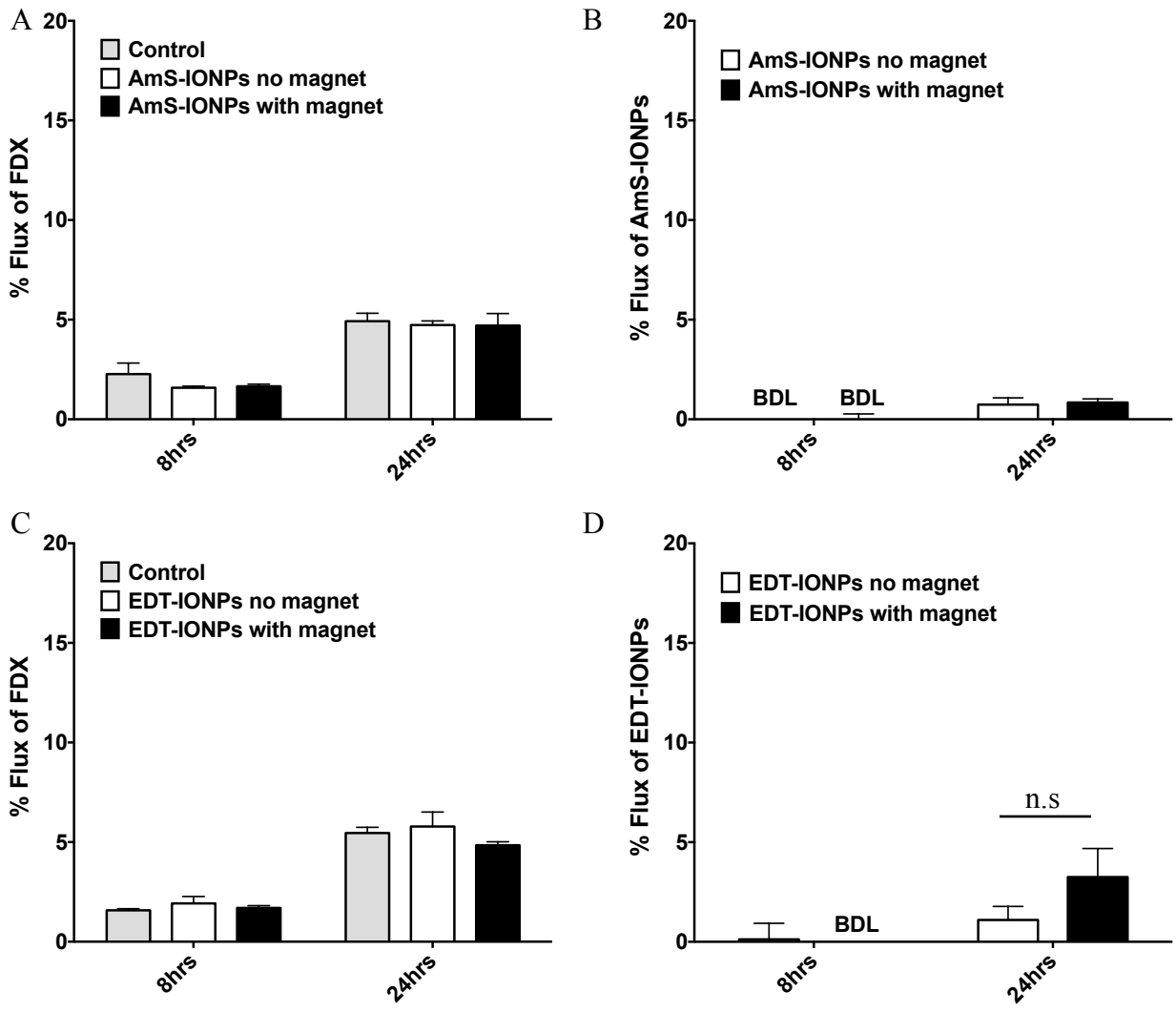


**Figure 3.2 Permeability of FDX-70000 and IONPs in confluent bEnd.3 cells monolayers in the presence and absence of a magnetic field. FDX-70000 flux was determined in control monolayers and monolayers treated with AmS-IONPs (A) and EDT-IONPs (C). The permeability of AmS-IONPs (B) and EDT-IONPs (D) was determined at 8 and 24-hours. Quantitative determination of IONP permeability was based on the amount of Fe in basolateral compartment divided by the amount of Fe loaded in apical compartment and recorded as a percentage. Values represent the mean ± SEM of 3 samples per treatment group. n.s indicate not significant**

Osmotic disruption of the BBB has been extensively studied and is a clinically proven method for enhancing the brain delivery of poorly permeable compounds. As expected, treatment of the cells with 1.4M mannitol significantly enhanced FDX-70000 permeability compared to the

intact BBB model (Figures 3.3A and 3.3C). However, it should be noted that the apparent permeability coefficients of FDX and both IONP formulations were higher in blank membrane than disrupted BBB model, suggesting some cellular resistance to passage of solutes remained even in disrupted state (Table 3.1). Under high osmotic conditions, permeability of the positively charged AmS-IONPs was found to be less than 5% in absence of a magnetic field and no significant change was observed with the application of a magnetic field (Figure 3.3B). This was in contrast to the negatively charged EDT-IONPs that displayed a 30% flux after 24 hours (Figure 3.3D) in the mannitol treatment group. In addition, the application of an external magnetic field further enhanced the permeability of EDT-IONPs in the mannitol treated monolayers, which significantly exceeded the flux observed with the FDX permeability marker at the 24 hour time point (Figures 3.3C and 3.3D). These results support our conclusion that MFECD may improve IONP based drug delivery to the brain.

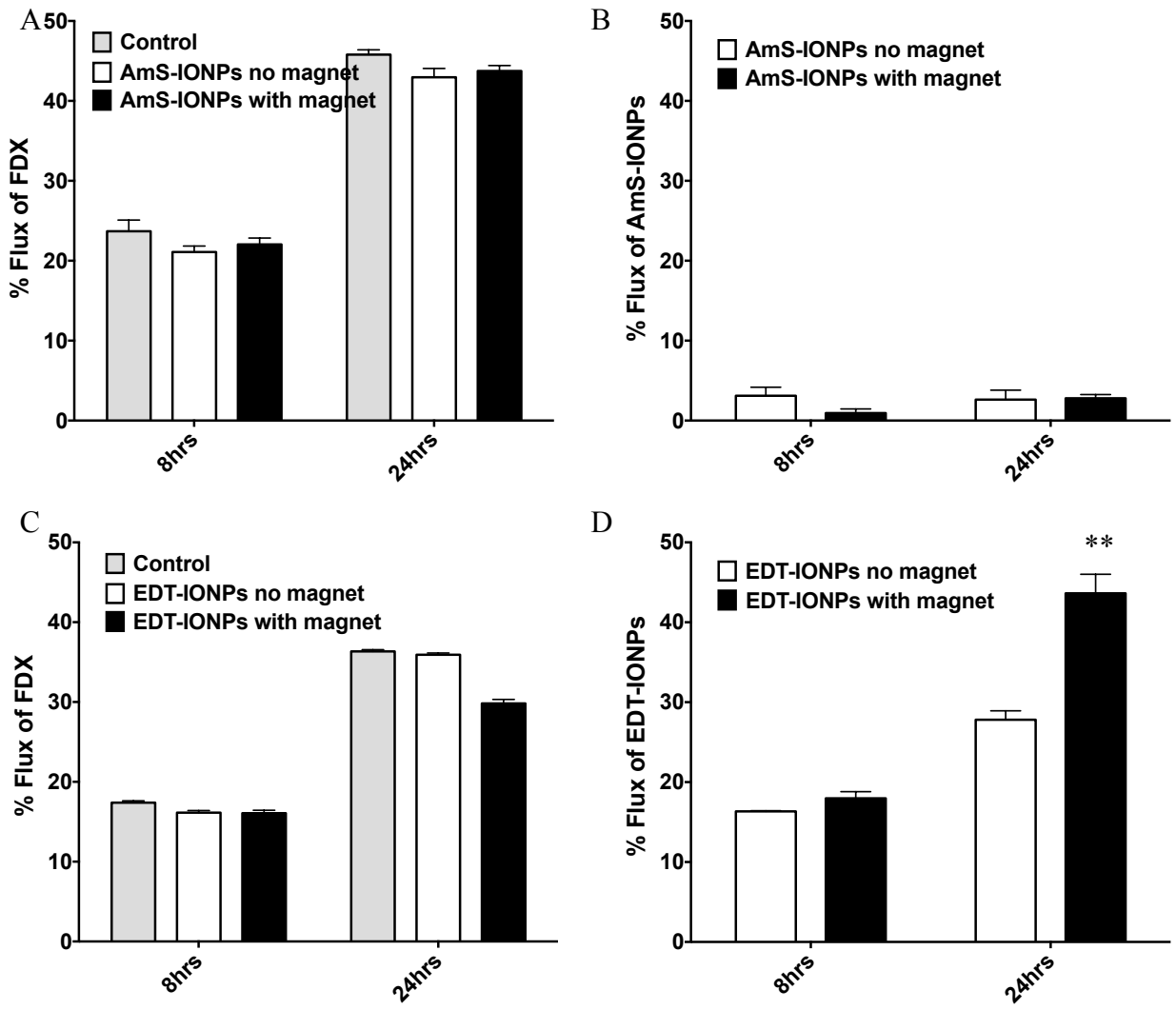


**Figure 3.3 Permeability of FDX-70000 and IONPs across osmotically disrupted bEnd.3 cell monolayers in presence and absence of a magnetic field. FDX-70000 flux was determined in control monolayers and monolayers treated with AmS-IONPs (A) and EDT-IONPs (C). The permeability of AmS-IONPs (B) and EDT-IONPs (D) was determined at 8 and 24 hours. Quantitative determination of IONP permeability was based on the amount of Fe in basolateral compartment over the amount of Fe loaded in apical compartment expressed as a percentage. Values represent the mean ± SEM of 3 samples per treatment group. ** indicates $p < 0.01$ compared to the same treatment group but without magnetic field.**

**Table 3.1 Permeability coefficient obtained in blank membrane, intact and disrupted BBB model for paracellular marker FDX 70000 MWT, AmS-IONPs, and EDT-IONP with or without magnet. The unit is $10^{-6}$ cm/s. Values represent the mean ± SEM of 3 samples per treatment group. ** indicates $p < 0.01$ compared to FDX-70000; *** indicates $p < 0.001$ compared to FDX-70000; † indicates $p < 0.001$ compared to same group in absence of magnetic field.**

| | Blank membrane | Intact BBB | Disrupted BBB |
|---|---|---|---|
| FDX 70k no magnet | 11.3 ± 0.1 | 0.20 ± 0.02 | 1.25 ± 0.04 |
| FDX 70k with magnet | N/A | 0.18 ± 0.02 | 1.11 ± 0.03 |
| AmS-IONP no magnet | 2.4 ± 0.2 | 0.03 ± 0.01** | 0.10 ± 0.04 *** |
| AmS-IONP with magnet | N/A | 0.03 ± 0.01** | 0.11 ± 0.02*** |
| EDT-IONP no magnet | 11.1 ± 0.3 | 0.04 ± 0.02** | 1.03 ± 0.05 |
| EDT-IONP with magnet | N/A | 0.12 ± 0.04 | 1.62 ± 0.15*** † |

To examine potential factors that could be responsible for the limited AmS-IONPs permeability in the osmotically disrupted BBB model, the permeability of the IONP formulations were determined across blank PC membranes (Figure 3.4A). Both IONPs showed similar trends with rapid flux to the basolateral compartment observed within 4-hours of incubation. The AmS-IONPs reached 10% flux at 4 hours and a steady-state permeability of 19% within 24 hours compared to less than 5% permeability in the disrupted cell culture model (Figure 3.4B). This suggests that the bEnd3 cells, regardless of monolayer integrity, act to reduce the permeability of the AmS-IONPs. In contrast, the EDT-IONPs reached 30% flux at 4 hours and continued to increase to 47% flux after 24 hours across the blank PC membranes. Compared to osmotically disrupted model of the BBB, no significant difference was found in the EDT-IONPs permeability (Figure 3.4B) indicating the cells were not a limiting factor to EDT-IONP penetration in the disrupted model of the BBB.

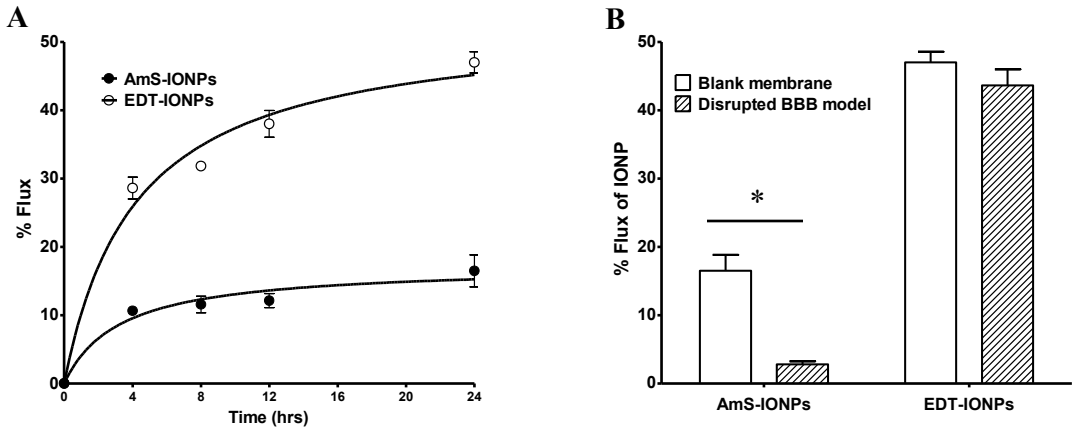


**Figure 3.4 Permeability of AmS-IONPs and EDT-IONPs across blank membrane inserts (A) and compared with NP permeability in disrupted model of the BBB at 24 hours (B). Values represent the mean ± SEM of 3 samples per treatment group. * indicate $p < 0.05$**

## 3.3.3 IONPs size distribution at physiological pH

To further understand the reduced permeability of the AmS-IONPs across the blank PC membrane, particle size distributions for the AmS- and EDT-coated IONPs were determined by PCS in water (pH 7.8 as measured before particles were dispersed) with the addition of NaOH to simulate more closely the pH conditions used in the permeability studies. Auto-correlation functions of the AmS- and EDT-IONP suspensions were measured at different times after sample preparation (Figure 3.5) and showed clearly the formation of AmS-IONP aggregates over time. EDT-IONPs did not show aggregation with time, consistent with a stable suspension. The average aggregate diameter of AmS-IONPs was 300 nm, and was observed to vary with scattering angle, indicating non-spherical aggregates[269]. The fraction of the IONP population displaying aggregation was determined from the relative contributions to the scattered light intensity and was observed to increase during the first few hours after sample preparation, after which it remained constant (Figure 3.6). Similar results were also found in DMEM cell culture media. As PCS measures only particles in suspension, it is likely that the aggregates grew in size

until thermal fluctuations were insufficient to keep the aggregates in suspension. A collection of several aggregates with average sizes of 300 nm could obstruct the 3 μm pores of the PC membrane leading to the observed reduced permeability of the AmS-IONPs.

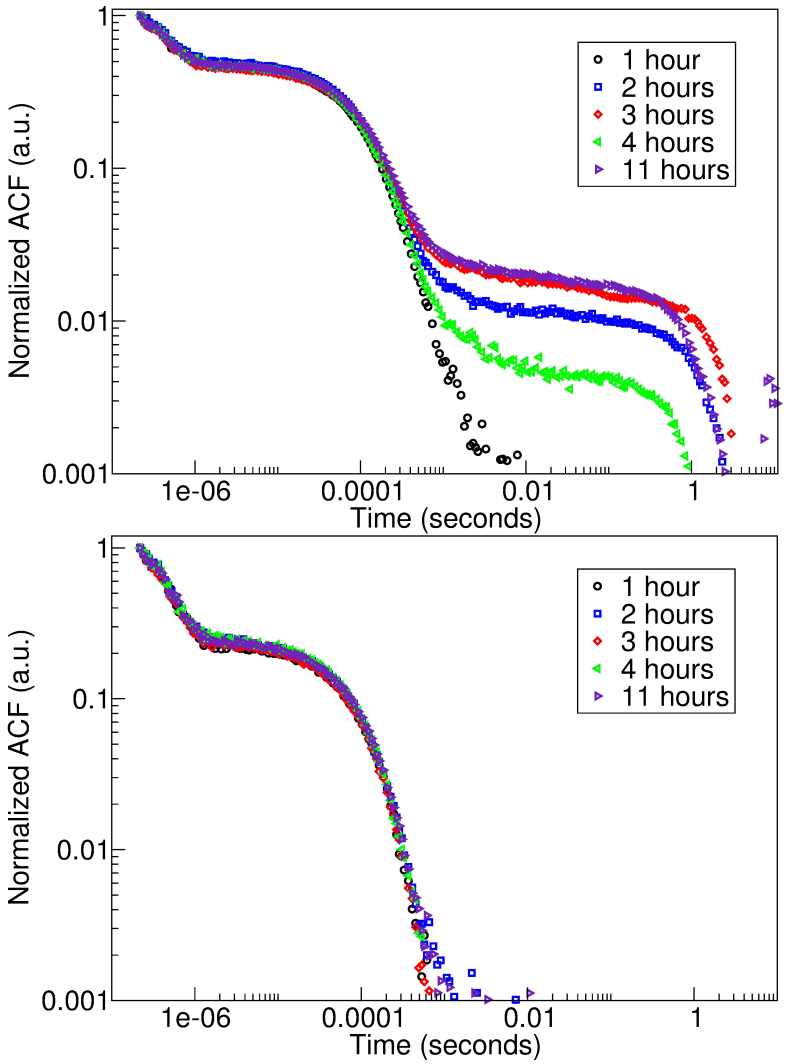


**Figure 3.5 Auto-correlation functions obtained by PCS for AmS-IONPs (top) and EDT-IONPs (bottom) in water at a scattering angle of 90 degrees. Symbols indicate time of measurement after suspension. Correlation at larger time scales is indicative of the presence of second, aggregated size distribution as seen only in the AmS-IONPs.**

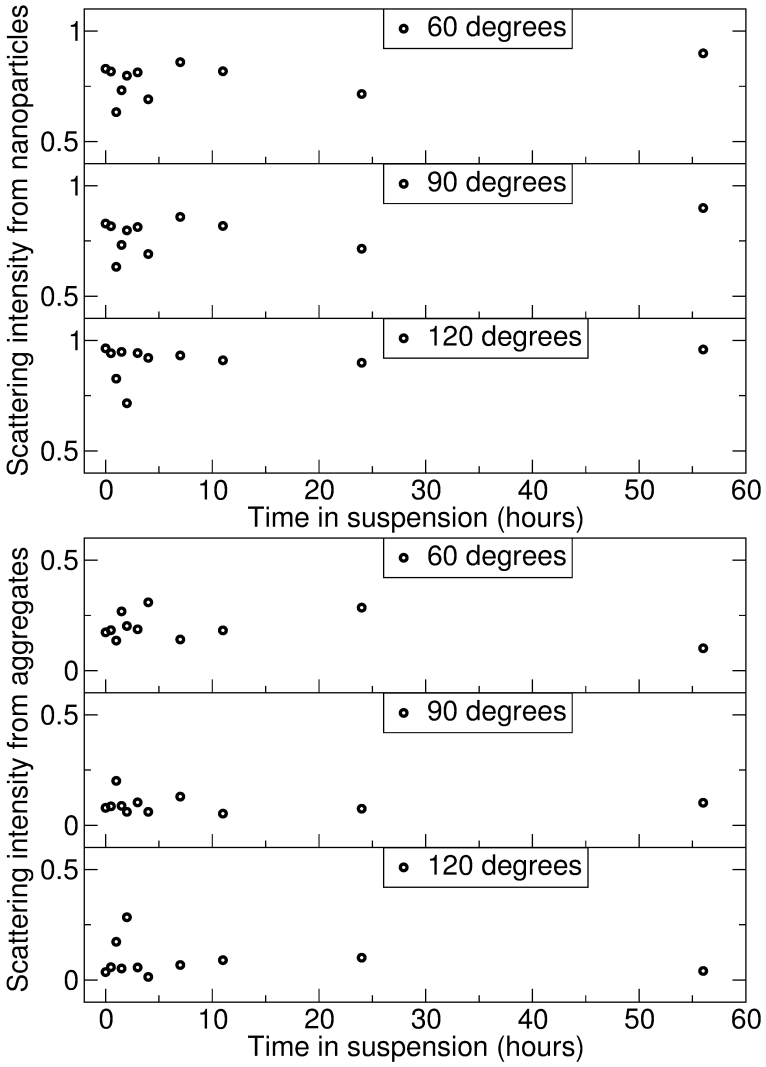


**Figure 3.6 Contributions to the scattered light intensity from AmS-coated NPs (top) and NP aggregates population (bottom) in water with physiological pH as a function of time from sample preparation. Scattering intensities are reported as the ratio of scattered light from a particular population to the total scattered light intensity. An increase in the relative population of aggregates is observed at small times (< 3 hours). The aggregates continue to grow in size past the point of stability and fall out of suspension, no longer contributing to the scattered light intensity**

## 3.3.4 Cellular uptake of AmS-IONP and EDT-IONP in bEnd.3 monolayers

To investigate if the endocytic transport of IONPs was altered by hyperosmotic conditions, the cellular accumulation of both IONPs in bEnd.3 monolayer were examined (Figure 3.7). The uptake of AmS-IONPs was found to be concentration dependent with

maximum of 30 ng of Fe accumulation per µg protein observed with the 50 µg/mL concentration of AmS-IONPs. Application of a magnetic field enhanced the accumulation of AmS-IONPs in the bEnd.3 cells by 5-fold at all concentrations tested (Figure 3.7). Similar studies performed with the EDT-IONPs resulted in substantially lower magnitude of cellular uptake compared to AmS-IONPs (Figure 3.7). In contrast to the AmS-IONPs, application of a magnetic field did not enhance the cell accumulation of EDT-IONPs (Figure 3.7). Furthermore, using hyperosmotic media had no significant impact on the cellular accumulation of either the AmS-IONP or EDT-IONP formulation (Figure 3.7).

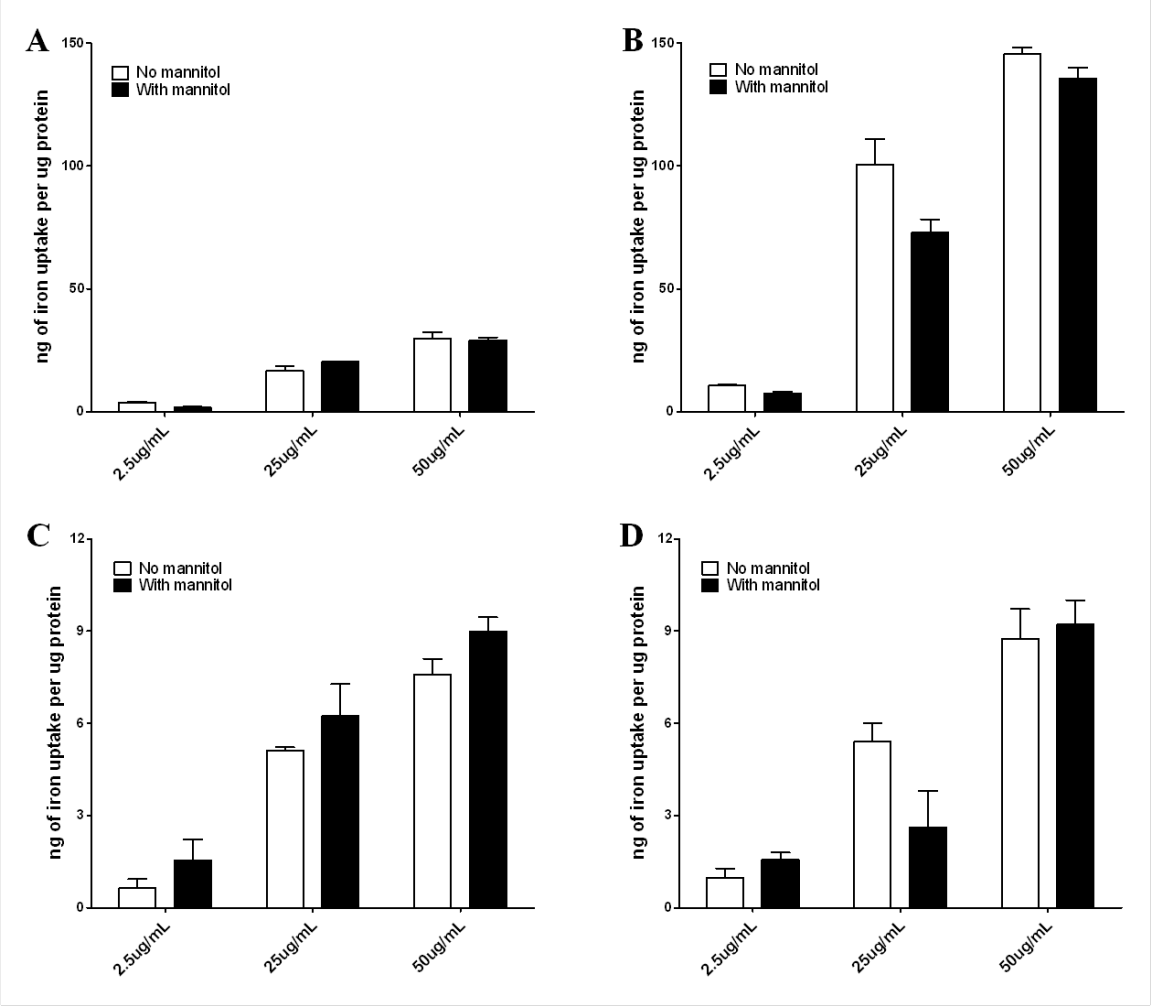


**Figure 3.7 Cell accumulation of AmS-IONPs in absence (A) and presence (B) of a magnetic field as well as EDT-IONPs uptake in absence (C) and presence (D) of a magnetic field.**

**Values represent the mean ± SEM of 3 samples per treatment group. No significant difference was found between the D-mannitol treated and the control group.**

## 3.4 Discussion

The present studies describe the potential application of MFECD as an approach for increasing IONPs delivery to the brain. While NP-based drug delivery is a rapidly progressing field, drug delivery applications in the CNS are severely limited due to the inability of most NPs to cross the BBB. Indeed, few publications have demonstrated transport of the NPs across the BBB[270-272]. It has been shown that uncoated, oleic acid-coated, and polyvinylamine-coated IONPs were impermeable across an endothelial cell culture model of the BBB, even in presence of a magnetic field[221]. In contrast, a size dependent permeation of polyethylene glycol (PEG) functionalized (non-magnetic) gold NPs was reported using rat brain microvessel endothelial cell culture model[273]. However, as these previous studies did not examine monolayer integrity with a permeability marker, the permeability observed may be attributable to the intrinsic leakage of the modeling system used.

This study utilized the magnetic properties of the IONPs to improve permeability through a MFECD process. With this technique, a magnetic field is used to enhance the bulk flow movement of IONPs. While there was a tendency for increased permeability of the EDT-IONP across intact bEnd.3 monolayers in the presence of a magnetic field, such effects were not statistically significant with the magnetic field strengths achieved in the present. This was expected, as tight junctions between the endothelial cells would restrict the bulk flow movement of the IONPs. However, enhancement of IONP permeability with MFECD was observed in the bEnd.3 monolayers following osmotic disruption of the tight junctions using 1.4 M mannitol. The extent of EDT-IONP permeability with MFECD following hyperosmotic disruption of the tight junctions surpassed that of the FDX 70000 permeability marker which has roughly the same size as albumin. Transient disruption of the BBB has been used to enhance chemotherapy

delivery in both preclinical and clinical treatment of brain tumors[195]. Several disruption methods have been developed. These include pharmacological disruption via the administration of compounds such as cadherin peptides[274], and phospholipids[275], infusion of hyperosmotic agents such as mannitol[276], and physical disruption via the application of techniques such as ultrasound[277]. Transient opening of the BBB with either osmotic disruption[278] or focused ultrasound (FUS)[212] has been used previously to increase IONP deposition in the brain. The development of FUS has attracted much attention as a non-invasive method for BBB disruption. When combined with microbubbles, FUS causes localized and reversible disruption of the BBB[279]. While the current study used osmotic disruption to remove water from the cell and break the tight junction complexes, MFECD as an approach to increase delivery of IONPs to the brain would work with any transient disruption technique. The key factors to consider in choosing a disruption protocol are the magnitude and duration of BBB opening since prolonged disruption of the BBB can result in pathological conditions such as extravasation of plasma components, edema formation, and neuroinflammation. The present studies provide the initial proof-of-concept for MFECD as a means to increase IONP delivery to the brain.

While the present studies demonstrate the utility of MFECD when combined with disruption of the tight junctions, it is important to note that not all IONPs formulations benefit equally from MFECD. The IONPs used in the present study possess the same core structure and size with surface chemistry modifications leading to different charges. As such the two IONP formulations examined provide an excellent platform from which to examine the effect of surface charge on MFECD of IONPs across the BBB. Our results confirmed that differently charged IONPs do not pass across the intact endothelial cell layer; however, in osmotic disrupted model of the BBB, the permeability of EDT-IONP increased substantially and was further

enhanced by the presence of a magnetic field. The observed permeability with the EDT-IONP in the absence of a magnetic field was comparable to that of the FDX permeability marker. After a 24 hour exposure to a static magnetic field, the EDT-IONP permeability (44%) was substantially greater than that observed with FDX (30%), and essentially of similar magnitude to that observed in blank membranes without cells. In contrast, AmS-IONPs displayed much lower permeability (less than 5%) in the osmotic disrupted model of the BBB compared to blank membrane permeability (19%). This suggests that even in its disrupted state, the bEnd.3 cells remain a barrier to positively charged AmS-IONPs. The effect of MFECD was most apparent after 24 hour with the EDT-IONPs having significantly greater permeability than the FDX permeability marker. While this study examined the effects of MFECD following a relatively long duration of barrier disruption, it is expected that increasing the magnetic field would allow for MFECD under less extensive BBB disruption conditions. Indeed, studies examining the influence of magnetic field strength are currently ongoing.

*In vivo* application of an external magnetic field for targeting of IONP to the brain is certainly more difficult than the current proof-of-concept studies *in vitro*. Pre-clinical studies in mice have used Nd-Fe-B magnets placed either on the outside skull or implanted intracranially to apply a local magnetic field[280,281]. These studies show a greater accumulate of the IONPs in the cortex near the magnet, with progressively lower accumulation in brain tissue farther from the magnetic field. Another group implanted tumor between the poles of an electromagnet[282,283], and demonstrated at least a 5 fold increase in magnetic targeting efficiency compared to non-targeted ones[284]. While this is the current state of the art, and has some limitations, it is not out of the question to consider the use of devices for generating “on/off” magnetic fields in discrete brain regions. Such system would provide even greater application for this technology.

Besides magnetic targeting, physio-chemical properties of IONPs such as surface charge are of great importance to application of MFECD. One reason for this may be the greater cellular uptake profile of the positive charged AmS-IONP. As reported previously, the negatively charged EDT-IONPs have a lower cellular uptake compared to positively charged AmS-IONPs Furthermore, the differences in EDT-IONP and AmS-IONP accumulation profiles in the bEnd.3 cells were unaffected by hyperosmotic conditions, suggesting endocytotic activity was not altered by hyperosmotic conditions. These findings, together with the increased permeability of EDT-IONPs in hyperosmotic conditions suggest the negatively charged IONP are more likely to favor the paracellular route and thus are more suitable for applications with MFECD.

An additional consideration for the differences in permeability of the IONP is the influence of surface charge on colloidal stability. The stability of a colloidal suspension is estimated by the magnitude of the surface (zeta) potential ($\zeta$) with $|\zeta| > 20$ mV corresponding to a well dispersed suspension[285]. NP surface charge is affected strongly by the properties of the suspension medium (e.g. pH, ionic strength, presence of plasma protein). At physiological pH there is a slight excess of hydroxide ions in solution. The positive surface charge of the AmS-IONPs attracts electro-statically a fraction of the excess hydroxide ions, effectively lowering the zeta-potential by means of charge cancellation. It is possible that at physiological pH, there are sufficient counter-ions in solution to reduce the surface charge of the AmS-IONPs below the point of stability, leading to aggregation. This is seen clearly in the PCS results collected for AmS- and EDT- IONPs. As demonstrated in previous studies he aggregation observed with the AmS-IONP may be further enhanced through interactions (e.g. electrostatic and friction) between NPs and the various proteins present in the cell culture media[249,286-288]. The combination of these effects leads ultimately to the reduced permeability of the AmS-IONPs across the blank

PC membrane when compared with the EDT-IONPs. Aggregation of the positively charged AmS-IONPs along with their high uptake in endothelial cell monolayers comprising the BBB suggest that IONPs with negative surface charge benefit most greatly from MFECD. Our results suggest that in order to maximize the effectiveness of MFECD on NP permeability, great care must be exercised in the design of NP coating to ensure long term colloidal stability at physiological pH.

The use of MFECD together with transient disruption of BBB permeability as a method for enhancing IONP delivery to the brain represents a substantial departure from vesicular transport pathways commonly examined. Multifunctional NPs have been developed by grafting BBB targeting moieties such as Angiopep-2 targeting low density lipoprotein receptor related protein (LRP) receptor and transferin antibodies targeting transferrin receptor to improve the BBB penetration via receptor mediated transcytosis[170,289]. Besides active targeting, adsorptive mediated transcytosis triggered by electrostatic interactions between the positively charged moiety on the NPs and negatively charged cell membrane of nanoparticles has also been evaluated for BBB delivery[290]. Although NP delivery to the brain via receptor mediated and adsorptive transcytosis has been reported, there are significant hurdles that remain. For example, the physiochemical properties of the particles can be altered by the covalent attachment of ligands resulting in reduced circulation times, which offset the potential benefits of active targeting[291]. Most importantly, the delivery efficiency via transcytosis as a percentage of the injected dose is rather limited. Only 0.25% of an injected dose of angiopep conjugated polyamidoamine dendrimer NPs per gram of brain tissue two hours after tail vein injection in Balb/c mice has been reported[180]. Even lower brain delivery efficiency was obtained using NPs coated with 29-amino-acid peptide derived from the rabies virus glycoprotein 4 hours after

intravenous injection in mice[292]. In addition, several *in vivo* studies have reported low efficiencies for brain delivery using the transcytosis route[181,293]. Examination of transcytosis in cell culture models of the BBB show relatively low permeability with prion labeled NPs (i.e. 6% flux) and cationic polyethyleneimine (PEI) coated NPs (i.e. 3.4% flux) following 18 hour permeability studies[294]. These permeability rates are consistent with the low permeability observed for the positively charged AmS-IONP in the present study.

## 3.5 Conclusion

This proof-of-concept study is concerned with feasibility of using MFECD to enhance the permeability of charged IONPs for potential brain targeted drug delivery. These studies show that MFECD when paired with disruption of tight junctions can significantly enhance IONP permeability in an *in vitro* model of the BBB. The effects of MFECD were most apparent with the negatively charged EDT-IONPs consistent with enhanced bulk flow permeability of IONP across transiently disrupted brain microvessel endothelial cells. The MFECD of EDT-IONPs provided higher delivery efficiency compared to either passive or active targeting of BBB vesicular transport processes. The use of MFECD in combination with methods for transient disruption of BBB permeability represents a potential method for enhancing drug delivery to the brain.

# Chapter 4 Biodistribution of negatively charged iron oxide nanoparticles (IONPs) in mouse and enhanced brain delivery using lysophosphatidic acid (LPA)

This chapter was submitted to Nanomedicine: Nanotechnology, Biology and Medicine and currently under review. Zhizhi Sun performed pharmacokinetic and biodistribution studies, brain capillary depletion, near infrared fluorescence imaging, and wrote the manuscript. IONPs synthesis and characterization was carried out by Matthew Worden, Histopathological and immunofluorescence analysis was carried out by Dr. Sabine Hombach-Klonisch. Electron microscopy was conducted by Dr. James A. Thliveris

# 4.1 Introduction

Iron oxide nanoparticles (IONPs) have attracted a great deal of attention as a potential drug delivery platform to treat cancer[295]. The deposition of NPs into a tumor through the so-called EPR effect relies on a leaky tumor vasculature. However, a heterogeneous tumor vasculature and low permeability at the early stages of tumor development limits this approach[265,295,296]. This is especially true in case of a brain tumor due to the presence of tight junctions between the endothelial cells and multiple efflux transporters, including P-gp, BCRP, and MRP on the brain endothelium[160]. To overcome these challenges, NPs have been grafted with ligands to improve transcytosis capacity by targeting specific receptors on the BBB. For examples, angiopep, a ligand targeting low-density lipoprotein receptor related protein 1 (LRP1), mediate cellular internalization of NPs and transport across the BBB[297]. Besides the LRP1 receptor, transferrin, insulin, and Diphtheria toxin receptors have also been utilized as "Trojan Horse" approaches for brain targeted drug delivery[176,178].

Transient disruption of BBB presents an alternative approach for delivering NPs into the brain. While there are several approaches for transient modulation of BBB using either pharmacological[203], osmotic[298] or ultrasound mechanisms[207], our laboratory has recently demonstrated that the phospholipid lysophosphatidic acid (LPA) induced rapid disruption of tight junction complexes in brain capillary endothelial cells, resulting in increased BBB permeability for both small and large molecules[192]. Importantly from a toxicity standpoint, the short circulation half-life of LPA provided rapid restoration of BBB integrity[299]. As the BBB permeability effects of LPA are similar across all areas of the brain[192], this agent appears to be an ideal way to provide a proof-of-concept for the delivery of IONP to the brain.

An additional advantage of transient disruption of the BBB as a method to increase the delivery of IONPs to the brain is the potential for magnetic targeting of IONPs to the brain. Our previous work introduced the concept of magnetic field enhanced convective diffusion (MFECD) *in vitro*[298]. We have shown that combining disruption of the tight junctions of brain endothelial cells coupled with an external magnetic field enhanced the permeability of negatively charged ethylenediaminetriacetate coated IONPs (EDT-IONPs) in a cell culture model of BBB. The purpose of the present study was to evaluate the feasibility of such an approach in an *in vivo* mouse model. Using systemically administered LPA to transiently open the BBB, we report a significant increase in the brain deposition of EDT-IONPs. The potential biocompatibility of this approach was also examined. Using activation of microglia and astrocytes as a measure of inflammation, neither LPA nor LPA in combination with EDT-IONPs produced any adverse effects. Our findings suggest that the transient disruption of the BBB by LPA is a safe and effective method for increasing IONP delivery to the brain.

## 4.2 Materials and Methods

### 4.2.1 Nanoparticle synthesis and characterization

Iron oxide nanoparticles were prepared under mild conditions at room temperature as previously described[233,267,298]. The EDT-IONPs were prepared by adding N-(trimethoxysilylpropyl)ethylenediaminetriacetate trisodium salt (EDT, 3 mmol, from a solution concentration of 45% in water) (Gelest, Morrisville, PA) directly to a reaction vessel containing IONPs. The mixture was allowed to react overnight with stirring and the final product was purified by dialysis (MWCO 30,000) against deionized (DI) water over 48 hours, and was freeze dried and resuspended in sterile PBS immediately prior to the experiments. The resulting nanoparticles had a magnetite ($Fe_3O_4$) core with a negatively charged surface coating. The IONP size distribution in DI water was determined initially through photon correlation spectroscopy (PCS) at a fixed scattering angle (90°) using a Horiba Nano-Partica SZ-100 series instrument (Horiba Instruments Inc., Irvine, CA). The same instrument allowed for the assessment of particle surface charge (zeta potential) by the measurement of IONP electrophoretic mobility using phase analysis light scattering.

### 4.2.2 Pharmacokinetic and biodistribution studies

The study was approved by the University of Manitoba Animal Care Committee on Animal Research, and was performed in accordance with the Canadian Council on Animal Care guidelines. Female Balb/c mice weighing 20 ± 5 g were obtained from the University of Manitoba breeding colony and maintained in the Central Animal Care Facility. Upon arrival, the animals were allowed to acclimatize for at least one week before the start of the experiment. The animals had access to food and water *ad libitum*, and were kept at a facility with a 12-hour light/dark cycle; controlled humidity (55% ± 5%), and controlled temperature (21°C ± 2°C).

Mice were injected intravenously with EDT-IONPs at dose of 5mg Fe/kg via the tail vein using a mouse restrainer. Control mice were injected with normal saline. For BBB disruption, LPA (1mg/kg) was injected along with the EDT-IONPs via tail vein. For magnetic targeting, animals were anesthetized using ketamine/xylazine mixture (87/13 mg/kg) and a Nd–Fe–B disk-shaped magnet (9mm diameter × 2mm thickness) was placed outside of the mouse skull on the surface of mouse skin following injection of EDT-IONPs. At various time points (2, 5, 15, 30 min), blood and tissue samples were collected. Tissue was weighed, and stored at –80° C before inductively coupled plasma (ICP) analysis and serum fractions were immediately separated by centrifugation (15 min at 2000 g) and stored at −80 °C.

For ICP analysis, all dilutions were done using in-house deionized water (≥18 MΩ-cm) obtained from a Millipore water purification system. The samples were weighed and digested overnight with 2 mL of 70% nitric acid: 36% hydrochloric acid (1:1 v/v) at 70 °C. The solution was diluted with deionized water to a final volume of 10 mL and filtered through 0.2 μm polyethersulfone (PES) filter. The samples were analyzed for 238.204 nm and 259.940 nm using an Elan 6100 ICP-MS (Perkin Elmer, Shelton, CT, USA) at the Manitoba Chemical Analysis Laboratory, University of Manitoba, Department of Chemistry, Winnipeg, MB, Canada.

Plasma data were subjected to non-compartmental pharmacokinetic analysis using Excel and pharmacokinetic parameters were calculated. The initial serum concentration ($Cp_0$) of IONPs was obtained directly from the concentration - time curves (log scale). The elimination rate constant (ke) was calculated by linear regression of the initial linear part of plasma concentration (log scale) against time. The elimination half- life ($T_{1/2}$) was calculated from the formula $T_{1/2}$ = 0.693/ke. Volume of distribution (Vd) and clearance (Cl) was calculated by formula Vd = dose/ $Cp_0$ and Cl = ke x Vd, respectively.

### 4.2.3 Brain capillary depletion

To accurately measure the EDT-IONPs in brain parenchyma, capillary deletion was performed as described by Triguero D et al., 1990[300]. Brain buffer solution (10 mmol/L HEPES, 141 mmol/L NaCl, 4 mmol/L KCl, 2.8 mmol/L $CaCl_2$, 1 mmol/L $MgSO_4$, and 1 mmol/L $NaH_2PO_4$, 10 mmol/L D-glucose at a physiologic pH of 7.4) was added at a volume of 5 times the weight of the brain tissue and the brain tissue was homogenized with a glass homogenizer for a total of eight strokes. An equal volume of 26% dextran solution was added and the resulting homogenate was then centrifuged at 5400 × g for 15minutes at 4°C. The supernatant fractions were collected for ICP analysis of the iron content in brain parenchyma.

### 4.2.4 BBB integrity assessment using near infrared fluorescence imaging

Confirmation of LPA-induced increases in BBB permeability was examined using NIRF. For these studies, mice received IRdye800cwPEG (0.01 μmol/kg), a pegylated dye of approximately 25 kDa used previously for assessing BBB permeability to large macromolecules[192]. The IRdye 800cwPEG was administered either alone or in combination with LPA (1 mg/kg) via tail vein injection. The mice were killed 15 minutes after treatment via cardiac perfusion with PBS solution. The brain was removed and the accumulation of NIRF dyes examined *ex vivo* using an Odyssey near infrared imaging system (Licor, Lincoln, NE, USA).

### 4.2.5 Histopathological and Immunofluorescence analysis

The expression of GFAP and Iba-1 in mice brain was examined using immunofluorescence at day 2 and day 7 following exposure to vehicle, LPA or LPA with IONPs. The mice were anesthetized and cardiac perfusion was done with 15mL of PBS followed by 40mL of 10% formalin. Whole brains were collected with the right hemisphere being used for ICP quantification of IONP accumulation, and the left hemisphere being used for histopathology

assessments. The left hemispheres were post-fixed, paraffin embedded, sagittal sectioned at 10 μm thickness and stained by H&E. For analysis of GFAP and Iba-1 expression, sections were de-paraffinated and antigen retrieved using a citrate buffer followed by 5% normal goat serum used as a blocking buffer. Slides were incubated with rabbit anti-mouse GFAP (Abcam, Toronto, ON) or rabbit anti-mouse Iba-1 (Wako Chemicals USA, Richmond, VA) or isotype-matched control antibodies followed by a secondary Dylight 594 goat anti-rabbit IgG (Thermo Fisher Scientific, Rockford, IL). The slides were washed with TBST three times for 45 min prior to DAPI counterstain for 2 min. Slides were mounted using Fluoromount G (eBioscience, San Diego, CA) and fluorescence microscopy imaging was performed using a ZEISS HB050 inverted microscope system and images were processed by Image-Pro Plus 6.0 software (Media Cybernetics, USA).

### 4.2.6 Western blot analysis

Brain samples were homogenized at 4 °C in lysis buffer [50 mM Tris–HCl, 150 mM NaCl, 10 mM EDTA, 10 mM NaF, 1 mM sodium orthovanadate, 1% NP-40, 10 mM sodium pyrophosphate decahydrate, 0.5 mM DTT, 0.2 mM PMSF and Complete Mini Protease Inhibitor Cocktail (Roche Diagnostics, Laval, QC, Canada); pH 7.4]. The lysates were centrifuged twice at 10,000 × g for 10 min. The protein concentration of the supernatant was determined using a BCA protein assay kit (Pierce, Rockford, IL, USA). Protein samples were denatured in a protein-loading buffer, separated on a 15% polyacrylamide gel, and subsequently transferred to polyvinylidene difluoride membranes (Biorad, Hercules, CA, USA). Anti-GFAP mouse mAb (Abcam, Toronto, ON, Canada) at 1:50,000, anti-Iba1 mouse mAb (Wako Chemicals USA, Richmond, VA, USA) at 1.5μg/mL were used to blot membranes at 4 °C overnight. These membranes were then incubated with HRP-conjugated anti-mouse or anti-rabbit secondary antibody for 1 h at room temperature. Blots were visualized by enhanced chemoluminescence

(Biorad, Hercules, CA, USA) according to the manufacturer's instruction. As an internal control, anti-β-actin (Santa Cruz, CA, USA) at 1:1000 was used to re-blot minimally stripped membranes. The bands were scanned and their densities were quantified using the Bio-Rad Laboratories Quantity One Software (Hercules, CA, USA). All target proteins were quantified by normalizing to β-actin on the same membrane, and then standardized to the corresponding control group.

### 4.2.7 Electron microscopy

The tissue localization of IONPs was also examined using transmission electron microscopy (TEM). For these studies, mice were perfused with 15 mL of PBS followed by 3% glutaraldehyde in 0.1 M phosphate buffer (pH 7.4). Brain, liver, spleen, kidney, and lung tissues were cut into 1-2 mm pieces and immersed in 3% glutaraldehyde in 0.1 M phosphate buffer for 3 hours. The tissues were then immersed over night in 0.1 M phosphate buffer containing 5% sucrose (pH 7.4) Tissues were then post-fixed in 1% osmium tetroxide in 0.1 M phosphate buffer (pH 7.4) for two hours. The tissues were dehydrated and embedded in Epon 812 using standard techniques[235]. Thin sections were prepared from the fixed tissue and stained with uranyl acetate and lead citrate. The resulting sections were viewed and photographed in a Philips CM 10 electron microscope. In order to eliminate observer bias, sections were examined without foreknowledge of their source.

### 4.2.8 Statistical analysis

All data were expressed as mean ± SEM. All values were obtained from at least three independent experiments. Statistical significance was evaluated using one-way ANOVA followed by post-hoc comparison of the means using the Fisher's least significant difference test.

# 4.3 Results

## 4.3.1 Physico-chemical characterization of IONPs

The physicochemical parameters of EDT-IONPs are provided in Table 4.1. The EDT-IONPs showed a narrow size distribution with a polydispersity index of 0.2. The mean hydrodynamic diameter of the EDT-IONPs suspended in water was 29 ± 1 nm as determined by PCS at 90° scattering angle. EDT-IONPs were silanized and had free carboxylic acid functional groups on their surfaces, resulting in a zeta potentials of approximately –39 mV. A more detailed description of the nanoparticles' characterization, including TEM images has been reported previously[298].

**Table 4.1 Characterization of EDT-IONPs**

| | Hydrodynamic size | Polydispersity Index | Zeta Potential |
|---|---|---|---|
| EDT-IONPs | 29 ± 1 nm | 0.215 ± 0.002 | -39 ± 3 mV |

## 4.3.2 Pharmacokinetic and biodistribution of EDT-IONPs

EDT-IONPs (dose: 5 mg Fe /kg) were injected into mice via tail vein. The serum and tissue distribution of EDT-IONPs were quantified by ICP (Figure 4.1). Mice receiving saline served as control, and provided background iron content for the tissue and serum samples. Volume of distribution, half-life, and clearance were calculated to be 1.4 mL, 5.9 minutes and 0.16 mL/min, respectively. The EDT-IONPs were quickly cleared from the blood compartment within 30 minutes following i.v. injection (Figure 4.1). Tissue deposition of EDT-IONPs indicated that the liver and spleen were the primary organs of deposition (Figure 4.1b-f). While the accumulation of IONPs in the liver increased over the time period examined, the spleen maintained a constant level of EDT-IONPs throughout all time points examined. At the 30

minute time point, 80% of the injected dose of EDT-IONPs was taken up by liver, and 10% had accumulated in the spleen. Electron microscopy confirmed the accumulation of IONPs in both the liver and spleen (Figure 4.2). Macrophages with IONPs were found in both white and red pulp of the spleen (Figure 4.2). IONPs were also found in Kupffer cells that are numerous in liver (Figure 4.2). EDT-IONPs were also found to a lesser degree in the kidney, with the amount of Fe in the kidney reaching a maximum of about 15% of the injected dose at 5 minute and quickly diminishing to 3% at 15 minute. Minimal amounts of EDT-IONPs were found in lung and brain parenchyma (Figure 4.1b, c). Electron microscopy confirmed that no IONPs were found in the brain (Figure 4.2).

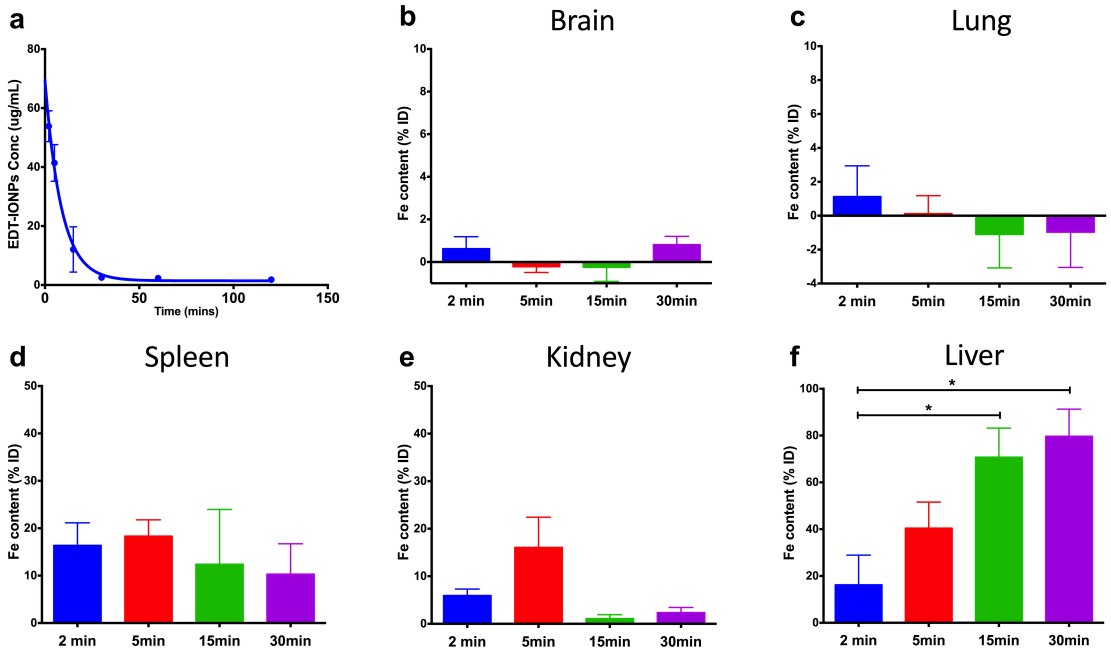


**Figure 4.1 Pharmacokinetic properties of EDT-IONPs. The presence of EDT-IONPs in serum (a), brain parenchyma (b), lung (c), spleen (d), kidney (e), and liver (f). Values were expressed as percentage of ID of Fe. Data are mean ± SEM, n = 4 mice.**

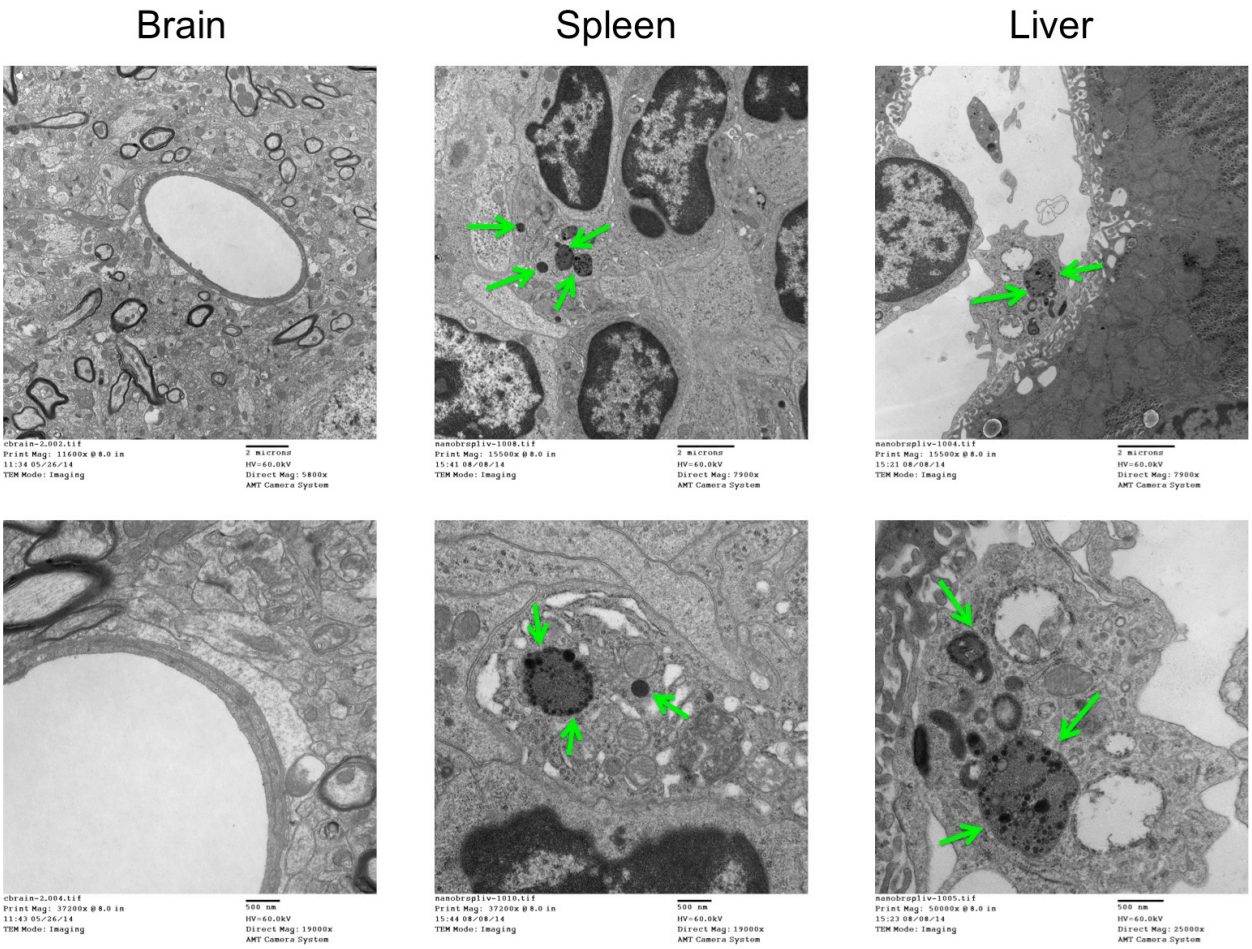


**Figure 4.2 Transmission electron micrographs of the brain, spleen, and liver in mice treated with EDT-IONPs alone. Top panel represents low magnification and bottom panel represents high magnification images; arrows point towards IONPs. There is no IONPs were found in lumen of the brain, endothelial cells, or brain parenchyma. IONPs were present in macrophages in spleen and Kupffer cells in liver.**

### 4.3.3 Effects of LPA on tissue distribution of EDT-IONPs

Previous studies have demonstrated LPA can transiently modulate BBB permeability allowing the movement of both small and large molecular weight contrast agents from the vasculature to the brain[192]. In the present study, LPA (1mg/kg) was co-administered with EDT-IONPs via tail vein injection in the presence and absence of an external magnetic field. To confirm that LPA increased BBB permeability, IRdye 800CW PEG, a 25,000 MW PEGlyated

IRdye was co-administered with or without LPA (Figure 4.3). Under control conditions, there was little if any appreciable dye accumulation in the brain. By contrast, exposure to LPA significantly enhanced the penetration of IRdye800, suggesting that LPA disrupted the tight junctions and enhanced paracellular diffusion within the cerebral microvasculature.

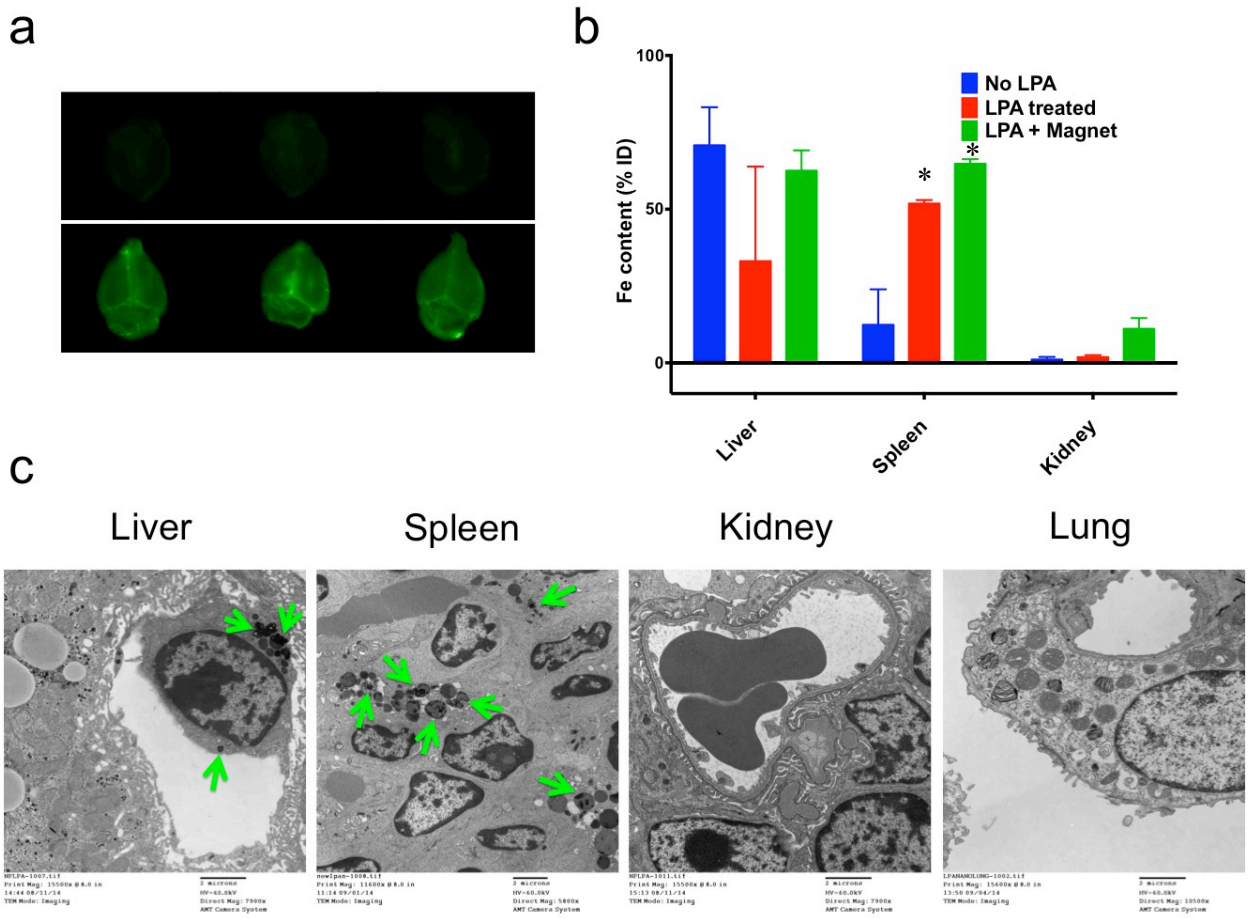


**Figure 4.3 Effect of LPA on BBB permeability as well as tissue accumulation of EDT-IONPs. Assessment of IRdye800cw PEG accumulation in the brain following intravenous bolus injections of control 2.5% bovine serum albumin in phosphate-buffered saline (top panel) or LPA (1 mg/kg) (bottom panel) (a). Effect of LPA and magnetic field on biodistribution of EDT-IONPs in liver, spleen, and kidney (b). TEM images showing EDT-IONPs in liver, spleen, kidney, and lung following LPA treatment (c). Green arrows point toward EDT-IONPs. * indicate $P < 0.05$ compared to control group in spleen.**

Compared to less than 1% of the injected dose of IONPs that reached the brain under normal conditions, 3.6% of the injected EDT-IONPs were found in the brain of LPA treated

mice (Figure 4.4a). Electron micrographs of brain tissue clearly demonstrated the presence of IONPs within the brain parenchyma, most likely within the microglia or astrocytes (Figure 4.4b). While transient disruption of the BBB with LPA significantly increased IONP deposition into the brain, the presence of a static external magnetic field did not further increase the accumulation of IONPs in the brain. There was also a marked increase in the accumulation of EDT-IONPs in the spleen of mice treated with LPA compared to mice treated with IONPs alone (Figure 4.3). All other tissues examined showed no differences in EDT-IONP accumulation in LPA treated mice compared to mice receiving no LPA.

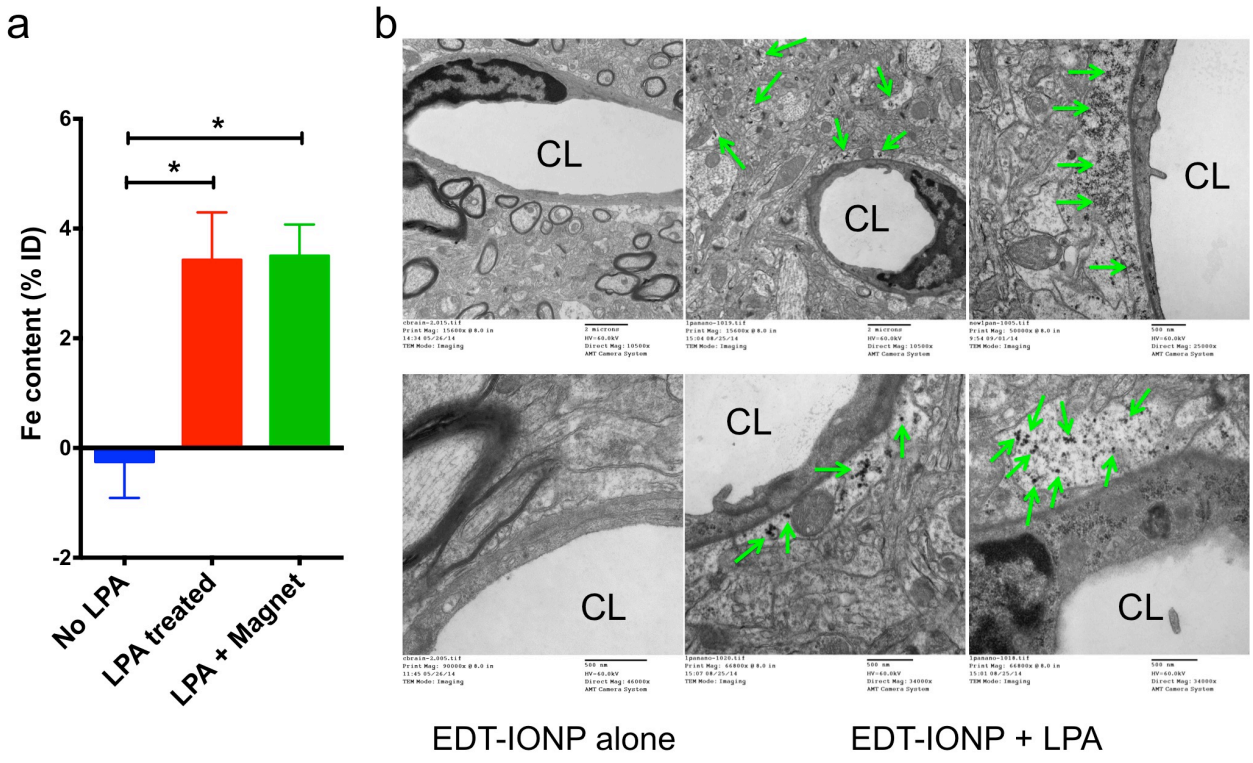


**Figure 4.4 LPA enhanced accumulation of EDT-IONPs in mice brain. The effect of LPA and magnetic field on IONP deposition in brain (a). Data are mean ± SEM, n = 4 mice. * represents $p < 0.05$. Transmission electron micrographs of EDT-IONPs in brain (b) with or without LPA treatment; arrows point towards IONPs. The capillary lumen (CL) in the brain micrographs are labeled to allow identification of capillary and surrounding cells.**

### 4.3.4 Impact of delivery approach on microglia and astrocyte activation

To determine the impact of the increased deposition of EDT-IONPs in the brain following transient disruption of the BBB with LPA, the biocompatibility of the nanoparticles and inflammation was assessed at 2 and 7 days following IONP administration. Histological examination of H&E stained brain tissue sections showed no infiltration of peripheral immune cells, and no detectable anatomical abnormalities upon treatment with LPA alone or in combination with IONPs (Figure 4.6 in supplementary material). In addition, immunofluorescence imaging of GFAP and Iba-1 in brains of mice at day 2 and day 7 following PBS, LPA, or LPA + IONPs treatment were similar in all treatment groups (Figure 4.5a,b). For comparison, immunofluorescence of GFAP and Iba-1 in brain tissue from mice with brain tumor xenografts showed significant increases in GFAP and Iba-1 staining (Figure 4.7 in supplementary material). The expression levels of GFAP and Ib-1 were also quantified using Western blot (Figure 4.5c,d). There was no significant difference in GFAP and Iba-1 expression between the various treatment groups at either time point. Examination of EDT-IONP deposition in the brain showed approximately 3% of the injected dose was retained in the brain parenchyma at 2 and 7 days post-treatment (Figure 4.8 in supplementary material). These data collectively indicate minimal activation of astrocyte and microglia following either LPA or LPA and EDT-IONP.

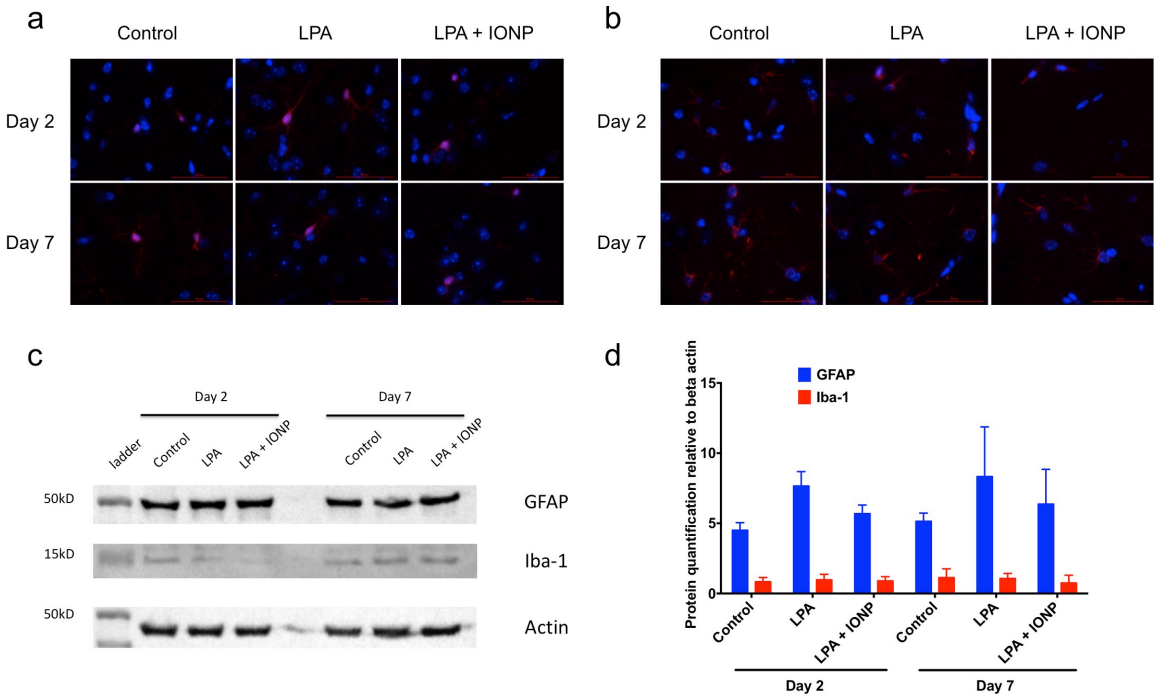


**Figure 4.5 Protein expression of Iba-1 and GFAP at day 2 and day 7 after EDT-IONPs delivery in the brain. Representative photomicrographs showed brain hippocampus immunofluorescent staining (red) for Iba-1 (a) and GFAP (b); bar 50 um. Representative western blot of GFAP and Iba-1 expression (c). Densitometry analysis of GFAP and Iba-1 expression normalized to β-actin (n=3) (d).**

## 4.4 Discussion

We report here the use of transient disruption of the BBB as a method to enhance the brain penetration of negatively charged EDT-IONPs. The selection of negatively charged IONPs in the present study is based on several previous findings. Negatively charged IONPs have improved colloidal stability compared to positively charged IONPs[298]. Negatively charged IONPs also showed lower levels of non-specific cell association compared to the positively charged IONPs[301]. Finally, in our *in vitro* cell culture models of BBB, EDT-IONPs were significantly more permeable than positively charged IONPs following osmotic disruption and magnetic field applications[298]. Thus, the negatively charged EDT-IONPs qualified as the most likely candidates for the *in vivo* proof-of-concept studies using transient opening of the BBB to enhance the delivery of IONPs to the brain.

In the current study, the half-life of negatively charged IONPs was found to be approximately 6 minutes. The main contributors to the clearance of EDT-IONPs were liver and spleen. Resident macrophages in both organs provide an active RES for efficient phagocytosis of circulating nanoparticles[302]. The TEM images from liver and spleen are consistent with the phagocytosis of EDT-IONPs. While the negative surface charge was likely involved in the reduced distribution to other tissues, cells of the macrophage linage recognize both positively and negatively charged surfaces via scavenger receptors[111,303 304].

The approach used in the current study to improve IONPs delivery to the brain involved transient disruption of the BBB using LPA to increase passage of the IONPs through paracellular diffusion routes. Previous studies demonstrated the ability of LPA to transiently modulate BBB permeability throughout all regions of the brain[192]. Systemic administration of LPA in mice lead to a 20-fold enhancement of methotrexate accumulation as well as 3-fold enhancement of a large

molecular weight contrast enhanced imaging agent in the brain[192]. While the magnitude of BBB opening was similar to that reported with osmotic disruption, the duration of LPA-mediated opening of the BBB (approximately 20 minutes) more closely correlated with the circulation time for the EDT-IONPs used in the present study.

Under normal conditions, there was minimal EDT-IONP penetration into the brain following i.v. administration. However, transient disruption of the BBB using LPA resulted in an >3-fold enhancement in brain penetration of IONPs. This is the first demonstration of nanoparticle delivery to the brain using LPA to transiently modulate BBB permeability. The amount of IONPs delivered to the brain following LPA-mediated BBB modulation was approximately 3.6% of the injected dose of EDT-IONPs. The enhanced delivery of IONP observed in the present study was greater than that reported previously, with targeted vesicular transport routes through the BBB. Furthermore, examination of inflammatory activation of microglia and astroctyes following the enhanced delivery of IONPs to the brain showed no differences compared to control animals, suggesting this method for enhancing delivery of IONPs to the brain, and EDT-IONPs delivered were safe on the brain.

It has been reported that accumulation of macromolecules in solid tumor, including primary and metastatic tumors are increased due to poor perfusion, poor lymphatic drainage, heterogeneity and leakiness of the tumor vasculature[47]. This phenomenon, the so called EPR effect, has been implicated in the increased permeability reported for various types of NPs in brain tumor models[48]. For example, Schleich and colleagues found 0.135% of injected IONPs in tumor bearing mice by passive targeting via EPR effect[305]. Application of an external magnetic field resulted in an even greater delivery of IONPs to brain tumor (approximately 8-fold larger compared to EPR effect alone)[305]. However even combined with a magnetic field, these studies

have a lower efficiency for delivery than observed in the present study, indicating that the EPR effect is most likely not sufficient to retain high concentration of IONPs within the tumor. Furthermore, the tumor microenvironment of disorganized tumor vasculature, elevated interstitial fluid pressure, and necrotic and hypoxic features limit homogenous accumulation of IONPs within the tumor and ultimately reduce therapeutic response[47,306].

Studies using osmotic disruption of the BBB have also reported increased delivery of various nanoparticles to the brain and brain tumor regions compared to non-disrupted controls[278,307]. The advantage of the osmotic disruption approach for the delivery of IONPs includes an improved delivery to tumor and non-tumor areas. Once delivered, the IONPs had a long residence time within the brain and tumor regions[308]. Although osmotic disruption has been used clinically for conventional, small molecule chemotherapeutic delivery to the brain, the disadvantage of this approach is that the extended BBB disruption allows macrophages as well as other small and large molecules to enter the CNS, inducing a transient increase in intra-cranial pressure[200,309].

The majority of studies examining the brain delivery of nanoparticles utilize receptor-mediated transport processes in the brain capillary endothelial cells (a Trojan horse approach) for enhancing transcellular permeability across the BBB. Such an approach requires the grafting of antibodies or ligands against various receptor targets on the brain endothelium, such as the transferrin receptor, insulin receptor, low-density lipoprotein receptor related protein 1 (LRP1) receptor, or diphtheria toxin receptor, to enhance drug accumulation in the brain. Although therapeutic responses have been observed with nanoparticle delivery to the brain using the Trojan horse approach, the actual amount of nanoparticle delivery in the brain was less than 1% of the injected dose. For example, transferrin modified paclitaxel-loaded polyphosphoester

hybrid micelles exhibited strong anti-glioma activity with only 0.03% injected dose per gram (ID/g) localized inside the brain[178]. Furthermore, angiopep-modified polyamidoamine dendrimer NPs showed higher brain delivery with 0.25% ID/g compared to unmodified NPs with only 0.03% ID/g entering into the brain[180]. The same group reported accumulation of 0.6% ID/g of angiopep-modified micelles in the brain[310]. These data collectively suggest that brain delivery of 0.25-0.6% of the administered dose is the upper limit for vesicular transport across the BBB. In this work, we show that LPA disruption of the BBB led to 3.6% ID of IONPs in mouse brain after 15 minutes. This represents a 5-fold increase over the receptor-mediated transcytosis approaches for the brain delivery of nanoparticles.

While the ligand targeted Trojan horse approach has demonstrated effectiveness in pre-clinical studies, translating ligand-targeted nanomedicine into the clinic practice is challenging. So far, none of the ligand-targeted nanomedicines for brain applications have made progress into phase III clinical trials[182]. The phase II clinical trial of GRN1005, a paclitaxel–angiopep-2 peptide drug conjugate, in non-small cell lung cancer patients with brain metastases is no longer recruiting participants, and it is likely not to advance into phase III due to the absence of beneficial effects. Yet, GRN1005 showed significantly improved delivery to the brain and brain metastases of breast cancer compared to free paclitaxel in animal models[168,311]. These studies suggest a disconnect between the effectiveness of the Trojan horse approach in examining brain delivery of nanoparticles in pre-clinical animal studies and human clinical trials. The present approach of using transient disruption of the BBB and an unprecedented enhancement in the delivery of IONPs to the mouse brain may provide a more suitable translation to the clinic.

Apart from demonstrating enhanced delivery of IONP to the brain, we examined the biocompatibility of the IONPs. While previous *in vitro* studies showed little toxicity to either

positive or negatively charged IONPs in various CNS-relevant cell types,[301] the absence of significant changes in either Iba-1 (microglia activation) or GFAP (astrocytosis marker) suggest minimal inflammatory effects following delivery of IONP to the brain. For metal oxide nanoparticles, factors that influence toxicity include nanoparticle composition[28,33], surface coating[27,35] and the amount and duration of exposure[39,41]. The positive expression of GFAP have been used as an indicator for astrocyte activation in mice. Aluminum oxide nanoparticles can induce astrocyte activation in the mouse hippocampus region[312]. Another study reported that titanium oxide nanoparticles can activate rat microglia, but not rat astrocytes using a proinflammatory cytokine release profiling method[313]. We confirmed that transient BBB disruption by LPA is safe without microglia or astrocyte activation, indicating minimal inflammation within the rodent brain. This may be due to the protective effect of the EDT coating since surface coating can greatly reduce microglia activation. For example, cationic amine-C12 dendrimers can lead to activation of both astrocyte and microglia following intraventricular injection. When coated with polyamidoamine dendrimers, the activatin of microglia and astrocyte were greatly reduced[314]. These "toxic" side effects are proportional to the amount of nanoparticles accumulating in the brain. Cupaioli et al., 2014 found in many experiments examining the toxic effect of nanoparticles to the brain, the amount of nanoparticles exposed is unrealistic compared to expected exposure following systemic administration, making the toxicity assessment hardly representative of real risk[315].

In addition to enhancing IONP accumulation in the brain, LPA treatment also resulted in increased IONP deposition in the spleen. While the mechanism is currently unknown, increased deposition of IONPs in the spleen following LPA treatment could be due to homing of circulating monocytes or macrophages. LPA has an important role in monocyte chemotaxis and

migration, and T cell homing to regulate immune response, which in turn might facilitate migration of IONPs containing immune cells[316,317]. There is also evidence to suggest that LPA up-regulates the scavenger receptor A in monocytes and macrophages[318]. We speculate that LPA stimulate uptake of EDT-IONPs in circulating monocytes and macrophages, and migration to spleen.

## 4.5 Conclusion

Transient modulation of the BBB by LPA achieved a significantly improved uptake of IONPs (3.6% of ID) in brain parenchyma. This amount is substantially greater than that achieved with transcytosis delivery of NPs across the BBB. The 20 minute window of opening of tight junctions by LPA aligned well with the short half-life of EDT-IONPs[192]. The phagocytic RES caused rapid uptake of EDT-IONPs. Future modifications to surface modalities of the IONPs are expected to reduce the clearance of IONP by the RES. This and our ability to extend transient BBB disruption to 1-2 hours may increase the accumulation of EDT-IONPs in the brain[319]. Under the conditions used in the present study, we recorded no significant toxicity with regard to infiltration of immune cells and no activation of microglia and astrocytes. LPA also facilitated accumulation of IONPs in the spleen, presumably through homing of immune cells to lymphoid tissues. This study has important implications in nanoparticle based drug delivery in the treatment of different brain disorders. Our strategy of delivering nanoparticles into the brain has broad applicability and, when combined with improved magnetic field enhanced drug-loaded nanoparticle technology[320], has the potential for efficient, targeted and safe delivery to the brain.

## 4.6 Supplementary Materials

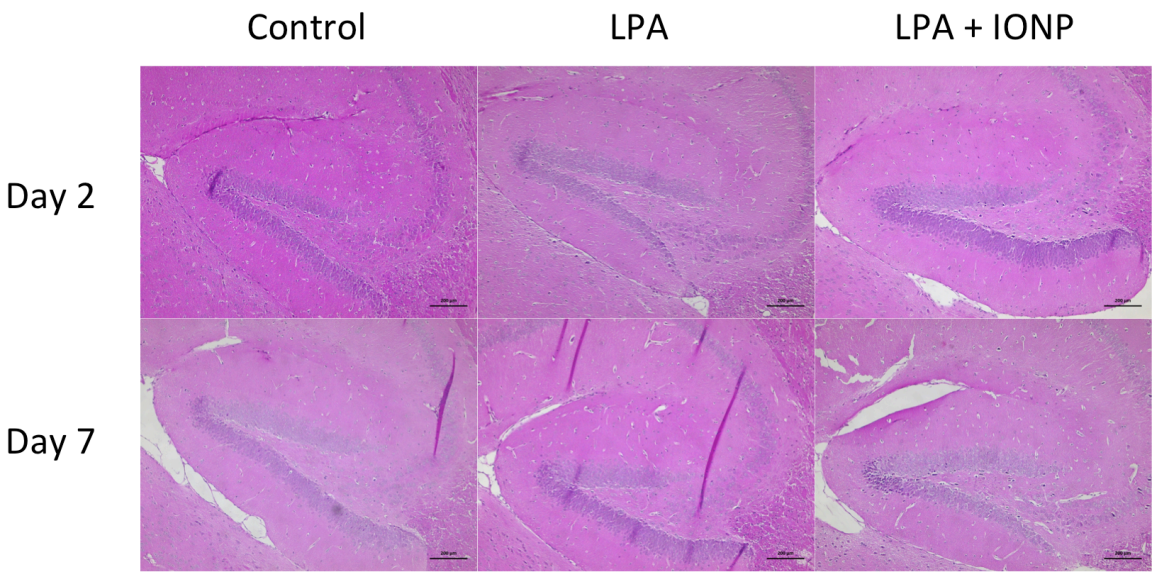


**Figure 4.6 Images of brain sagittal sections stained with hematoxylin and eosin at day 2 and day 7 following treatment of LPA or IONPs; bar 200 µm.**

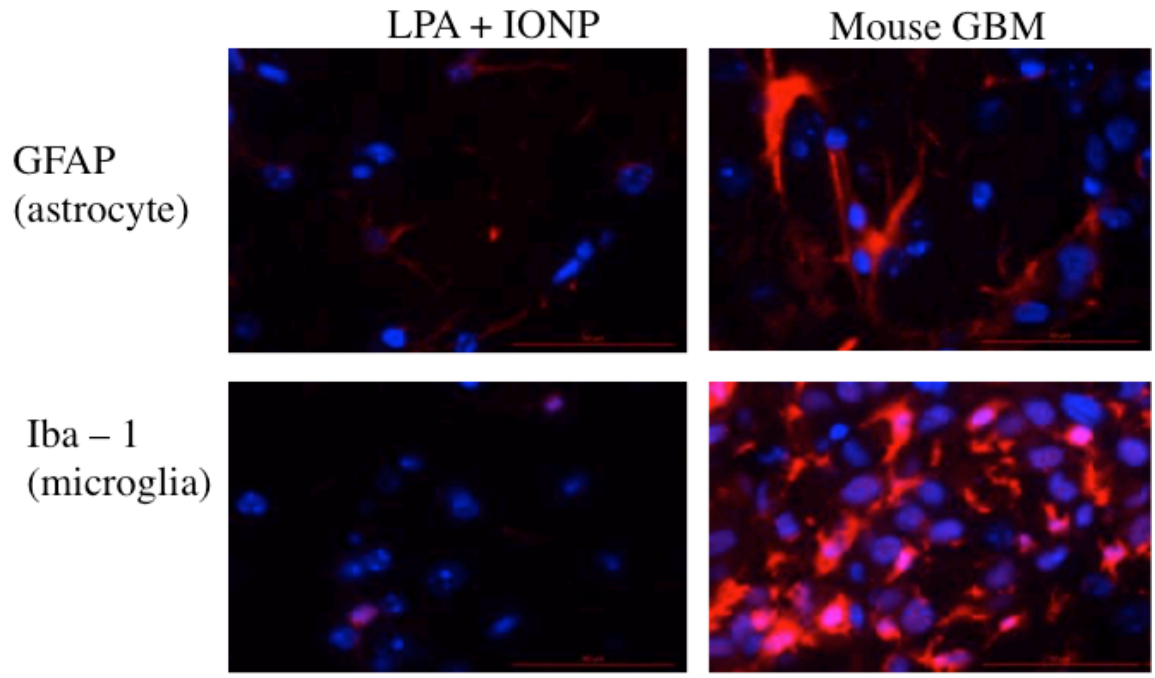


**Figure 4.7 Immunofluorescence of Iba-1 and GFAP after delivery of EDT-IONPs into the brain. We did not observe an increase in Iba-1 or GFAP immunostaining in the mouse brains exposed to LPA and EDT-IONPs. Immunofluorescence was also examined in**

**similarly fixed brain slices from human glioblastoma xenografts as positive control. Blue: DAPI stain for nucleus. Red: GFAP in astrocyte (top panel) and Iba-1 (bottom panel).**

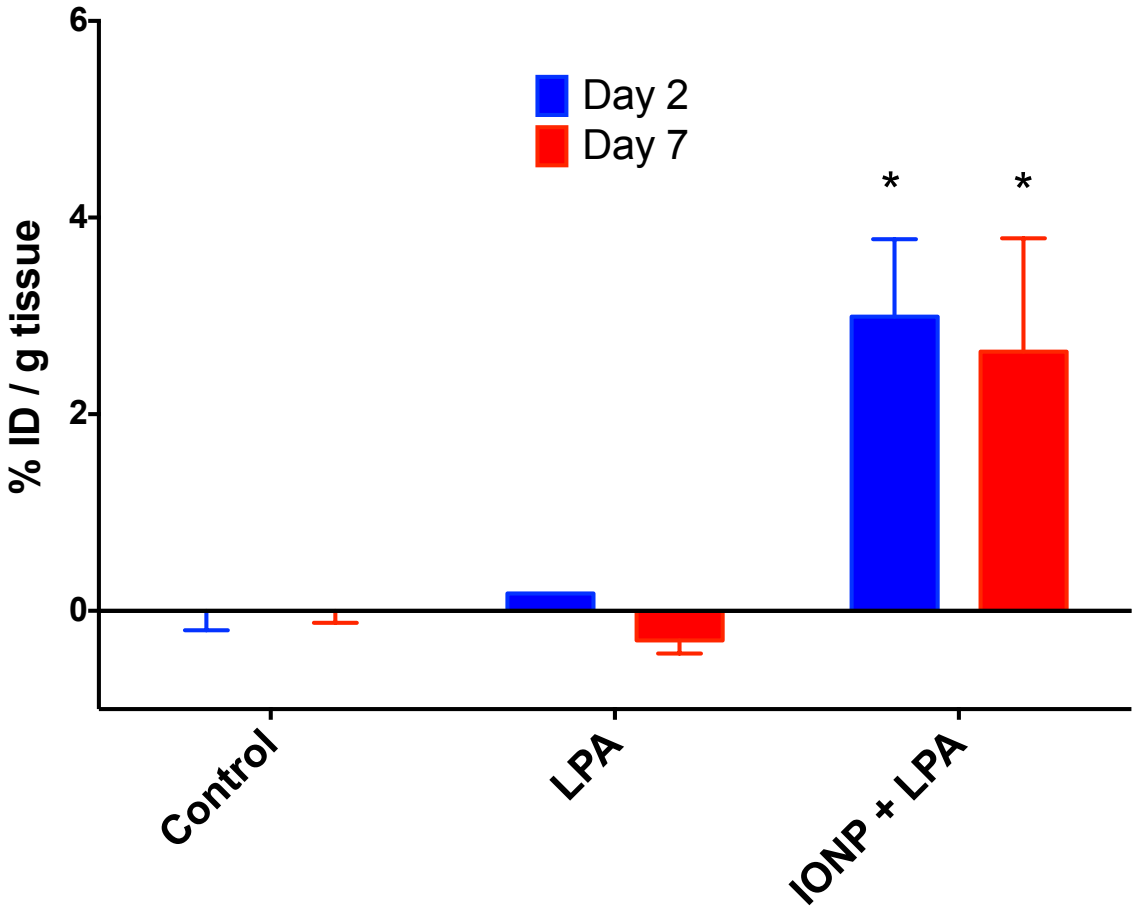


**Figure 4.8 Accumulation of EDT-IONPs in right hemisphere of mice treated with LPA and IONPs. * indicate P < 0.05 compared to mice receiving EDT-IONPs alone (control) and LPA treatment group which received no IONP. This confirmed the presence of EDT-IONPs of the left hemisphere of mice when subjecting to histopathology analysis.**

# Chapter 5 Differential Internalization of Brick Shaped Iron Oxide Nanoparticles by Endothelial Cells

This chapter was submitted to Journal of Biomedical Nanotechnology and currently under revision. Zhizhi Sun performed cell culture and the uptake of nanoparticles in various cells, quantitative determination of IONPs, prepared cells for EM and wrote majority of the manuscript. IONPs synthesis, characterization, and simulation of magnetic field profile were carried out by Matthew Worden, Yaroslav Wroczynskyj, Palash K. Manna. Electron microscopy was conducted by Dr. James A. Thliveris.

# 5.1 Introduction

There is a growing interest in developing iron oxide nanoparticles (IONPs) as platforms for drug delivery applications[321-323]. In this regard, IONPs provide several advantages: 1) The ability to target to areas of interest using externally applied magnetic field, thereby increasing local therapeutic concentration and decreasing potential toxicity related to systemic circulation. 2) Monitoring capabilities for IONPs using MRI. 3) Favorable biocompatibility profile. 4) Flexibility of surface modification to build multifunctional complexes for advanced drug delivery applications involving intracellular or plasma membrane targets. The interaction between IONPs and the cell membrane is largely determined by their physiochemical properties such as the surface coating and shape[324,325]. Our group has previously examined the effect of surface charge on the cellular uptake of IONPs[301]. We found that positively charged IONPs have a significantly higher uptake profile compared to negatively charged ones, likely due to electrostatic interaction between positively charged IONPs and the negatively charged plasma membrane of the cell. As a result, negatively charged nanoparticles appeared to be better candidates to advance in our drug delivery platform due to the potential for longer circulation times and reduced clearance. However, the charge related effects on internalization were non-specific as they were present in a variety of different cell types[301].

Various pathological conditions such as cancer, cardiovascular disease, inflammation, and oxidative stress would benefit from the preferential delivery of nanoparticles to the vascular endothelium[326-328]. To achieve the cell specific delivery, targeting ligands are often grafted onto the NPs to increase the delivery efficiency. For instance, intracellular adhesion molecule (ICAM), vascular cell adhesion molecule (VCAM), and platelet-endothelial cell adhesion molecule (PECAM-1) have been used to target endothelial cells[329-331]. However, these

approaches are often associated with variability in outcome due to different receptor expression levels between patients or heterogeneity of endothelial cells within the tumor itself[332]. Therefore, a generalized approach that preferentially target endothelial cells without ligand receptor interaction would be advantageous.

In addition to surface charge, nanoparticle shape may also play a role in cell interactions. To date, there are few reports concerning non-spherical nanoparticles. Recent work with theoretical modeling revealed the role of nanoparticle shape and membrane rigidity on cellular uptake[333]. However, only a handful of studies provide side-by-side comparison of spherical and non-spherical nanoparticle interactions with biological environments[334]. Recent advances in synthesis techniques have enabled creation of brick shaped IONPs[320]. We hypothesize that changing the IONP shape will influence both the cellular uptake in endothelial cells and the ability to augment cell uptake with application of an external magnetic field. Toward that end, the uptake profiles of iron oxide nanospheres and nanobricks in various cell types were examined. In addition, the mechanism of preferential uptake of the nanobrick IONPs in endothelial cells was determined with evidence suggesting a caveolin-dependent process. By understanding the relationship between IONP shape and cell surface domains, our work provides insight into the development of IONPs for specifically targeting endothelial cells.

## 5.2 Materials and methods

### 5.2.1 Materials

All chemical reagents were purchased from Sigma Aldrich (St. Louis, MO) and cell culture reagents from Invitrogen Canada Inc. (Burlington, ON) unless otherwise specified.

### 5.2.2 Nanoparticle synthesis and characterization

Sphere shaped iron oxide nanoparticles were prepared under mild conditions at room temperature as previously described[298]. They were prepared by adding N-(trimethoxysilylpropyl)ethylenediaminetriacetate trisodium salt (EDT, 3 mmol, from a solution concentration of 45% in water) (Gelest, Morrisville, PA) directly to a reaction vessel containing IONPs . The mixture was allowed to react overnight with stirring and the final product was purified by dialysis (MWCO 30000) against deionized (DI) water over 48 hours and was freeze dried and resuspended in sterile PBS prior to experiments. Brick shaped IONPs with EDT surface coating was synthesized and prepared as recently described[320].

Nanoparticle crystallographic properties of both the nanospheres and nanobricks were measured with powder x-ray diffraction experiments using a Brüker diffractometer (D8 Discover with Davinci; Karlsruhe, Germany). Both nanoparticle systems were identified as iron oxide through Reitveld refinement incorporating the effects of the nanocrystalline nature of the samples (e.g. Scherrer broadening effects).

The IONP size distribution in DI water was determined initially through photon correlation spectroscopy (PCS) at a fixed scattering angle (90°) using a Horiba Nano-Partica SZ-100 series instrument (Horiba Instruments Inc., Irvine, CA). The same instrument allowed for the assessment of particle surface charge (zeta potential) by the measurement of IONP electrophoretic mobilities using phase analysis light scattering. The magnetization of dry

nanoparticle powder samples were recorded at room temperature as a function of applied magnetic field (0 – 4 T) using a Quantum Design MPMS XL SQUID magnetometer (San Diego, CA).

### 5.2.3 Cell culture

A mouse brain derived microvessel endothelial cell line, bEnd.3 (American type tissue culture collection, Manassas, VA), was used as a cell culture model of the blood-brain barrier (BBB). The bEnd.3 cells (passage number 15-30) were cultured in DMEM (Hyclone, Logan, UT) supplemented with 10% heat-inactivated FBS (Hyclone, Logan, UT), 50 U/mL penicillin and streptomycin (MP Biomedicals, Solon, OH) at 37°C and 5% $CO_2$. Cells were expanded in T-75 tissue culture flasks, and seeded at $2x10^4$ cells per $cm^2$ on 6 or 12 well plates for uptake and cytotoxicity studies, respectively. Culture medium was changed every 2 days. All experiments were performed on confluent monolayers (typically 4-5 days post seeding).

### 5.2.4. Cellular Uptake of IONP compositions

Confluent monolayers of various cell types including bEnd.3 cells, primary human lung endothelial cells, primary brain endothelial cells, Madin-Darby canine kidney (MDCK) epithelial cells, human hepatocellular liver carcinoma (HepG2) cells grown on 6-well culture plates (Costar, Lowell, MA) were treated with culture media containing either nanosphere or nanobrick compositions (2.5μg/mL – 100μg/mL of Fe). After treatment with IONPs, cells were placed in a humidified $CO_2$ incubator maintained at 37°C. After 4 hours, the IONP solutions were removed and the cell monolayers were washed 3X with ice cold PBS to remove unbound nanoparticles. Cells were lysed by the addition of 500 μl of 0.2 M NaOH and IONP content determined based on the ferrozine assay described below. Cellular accumulation was examined in both the presence and absence of a static magnetic field created by placing the cells over a platform

containing cylindrical rare earth magnets (19mm diameter, 3mm height) (Lee Valley, Ottawa, ON, Canada). Cells remained in the magnetic field for the duration of the experiment.

For mechanistic studies of IONP uptake, cells were pretreated with chlorpromazine (7 μg/mL), methyl-beta-cyclodextrin (10 mM), genistein (200 μM), monensin (25 μM), or cytochalasin D (5 μg/mL) for 30 min at 37°C. Cells were exposed to the nanobricks for 1 h at 37°C in the presence of the various endocytotic inhibitors. Cell association of nanobricks was determined as described below.

Additional studies using known markers of caveolae mediated endocytosis, alexa fluor 488-labeled cholera toxin subunit B (CTB) and tetramethylrhodamine conjugated bovine serum albumin (BSA) were examined for cellular uptake. For these studies, cells were exposed to CTB (3.5 μg/mL), BSA (10 μg/mL) for 2 h either alone or following 15-min pretreatment with various concentrations of the iron-oxide nanobricks. Cells were washed and lysed and fluorescence determined using a Synergy HT plate reader (BioTek, Winooski, VT).

### 5.2.5 Analytical assay for measuring IONPs

Quantitative determination of IONP content in cell and media samples was performed using the Ferrozine assay. As the Ferrozine assay is an absorbance-based assay for determining soluble iron concentrations, IONPs in the cell lysate and media samples were first solubilized by adding 500 μL of concentrated HCl (~12M) to 500 μL of cell lysate or media samples. This mixture was incubated for 1 h at room temperature with gentle shaking and then neutralized with 500 μL of 12M NaOH. Once the samples were neutralized, 120 μL of hydroxylamine hydrochloride (2.8 M) in 4M HCl was added and the samples incubated for 60 min at room temperature with gentle shaking. Following this incubation, 50 μL of 10 M ammonium acetate solution (pH 9.5) and 300 μL of 10 mM ferrozine in 0.1M ammonium acetate solution were

added to each sample. Absorbance was measured at 562 nm using a Synergy HT plate reader (BioTek, Winooski, VT). Quantitative assessment of IONP concentration was based on a standard curve prepared by serial dilutions of 1000 ppm iron atomic absorption standard (Fisher Scientific, Ottawa, ON). Samples from the cell lysates were normalized for protein content using BCA protein assay kit (Pierce, Rockford, IL).

### 5.2.6 Electron Microscopy

The cellular localization of IONPs compositions was examined using transmission electron microscopy. For these studies, cells were incubated with IONPs at 50μg/mL concentration in media for 2 hours. After incubation, cells were washed 3X with PBS and collected using 0.25% trypsin EDTA (Hyclone, Logan, UT). After centrifugation, the cell pellets where fixed in 3% glutaraldehyde in 0.1M phosphate buffer (pH 7.3), followed by post-fixation in 1% osmium tetroxide in 0.1M phosphate buffer (pH 7.3). Cells were then dehydrated and embedded in Epon 812 using standard techniques[235]. Thin sections were stained with uranyl acetate and lead citrate, viewed and photographed in a Philips CM 10 electron microscope (FEI, Hillsboro, OR, USA). In order to eliminate observer bias, sections were examined without foreknowledge of their source.

### 5.2.7 Statistical analysis

All data were expressed as mean ± SEM. All values were obtained from at least three independent experiments. Statistical significance was evaluated using one-way ANOVA followed by post-hoc comparison of the means using the Tukey's test.

# 5.3 Results

## 5.3.1 Physico-chemical characterization of IONPs

Physico-chemical parameters of the nanobrick and nanosphere compositions are provided in Figure 5.1. Both nanobricks and nanospheres were silanized and had free carboxylic acid functional groups on their surfaces resulting in zeta potentials of approximately -40 mV. The TEM images confirming the different shapes of IONPs have previously been published[298,320]. The dimensions of IONP core for the nanobricks were approximately 15 nm x 10 nm x 5nm while the nanosphere was around 8 nm in diameter. The saturation magnetization, determined by fitting the high field magnetization to a straight line after background subtraction (diamagnetic signal from the sample holder), was 50 ± 5 A $m^2$ $kg^{-1}$ and 10 ± 2 A $m^2$ $kg^{-1}$ for the nanobricks and nanospheres, respectively. The saturation magnetization is the largest magnetization that a material can exhibit in an applied magnetic field. Samples with larger saturation magnetizations have greater magnetic response and thus are likely more useful for targeted delivery using an externally applied magnetic field. A more detailed description of the nanoparticle's characterization is provided in the Supplementary Information.

| | **Nanospheres** | **Nanobricks** |
|---|---|---|
| Surface Coating | 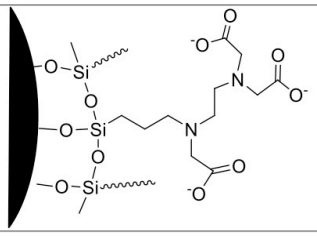 | |
| TEM Size | 8 nm | 15 x 10 x 5 nm |
| Zeta Potential | -39 ± 3 mV | -45 ± 3 mV |
| Saturation Magnetization | 10 ± 2 A $m^2$ $kg^{-1}$ | 50 ± 5 A $m^2$ $kg^{-1}$ |

**Figure 5.1 Physicochemical properties of nanosphere and nanobricks. IONP core size were determined by TEM and charge were measured in triplicate samples using a Nano-partica SZ-100 series instrument from Horiba. Values represent the mean ± SEM (n=3).**

## 5.3.2 Preferential internalization of nanobrick in endothelial cells

Quantitative uptake analysis was performed in the bEnd.3 mouse brain endothelial cell line. (Figure 5.2a) In absence of magnetic field, there was a significantly greater uptake of nanobrick compared to nanosphere compositions at all concentrations above 5 μg/mL. In the presence of external magnetic field, cell association of nanobrick was substantially increased compared to nanosphere. At the highest concentration examined (100 μg/mL), there was a 30-fold and 10-fold increase in uptake of nanobricks compared to nanospheres with and without a magnetic field, respectively. This surprising finding suggests that despite the negative surface charge, brick shaped IONPs are taken up by brain endothelial cells to a greater extent than spherical counterparts. Furthermore, the shape of IONPs affected their magnetization value and ability to interact with cells in the presence of an external magnetic field gradient.

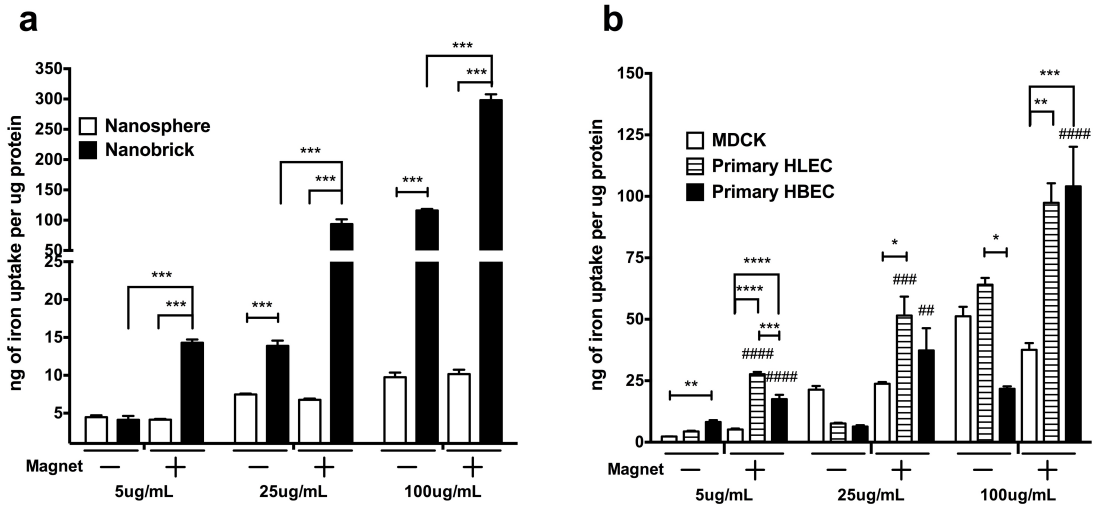


**Figure 5.2 Cellular accumulation of nanobricks and nanospheres in bEnd.3 cells (a). Uptake of nanobricks in MDCK, primary human lung and brain endothelial cells (b). Experiments were performed in the presence and absence of external magnetic field. Values are expressed as the mean ± SEM for three cell monolayers per treatment group.**

**##, ###, #### indicate p<0.01, <0.001, <0.0001 respectively compared to the same treatment group without magnetic filed exposure. *, **, *** and **** indicate p<0.5, <0.1, <0.001, and <0.0001.**

Uptake studies with the nanobrick was expanded to include primary human lung and brain endothelial cells as well as Madin-Darby canine kidney (MDCK) epithelial cell line with two fold purpose: 1) To investigate whether there was any selectivity to endothelial cells versus epithelial cells; and 2) To examine whether enhanced uptake of the nanobricks was specific to brain endothelial cells compared to other endothelial beds. External magnetic field significantly enhanced cellular uptake of nanobricks in both the lung and brain microvessel endothelial cells but not in epithelial cells (MDCK) (Figure 5.2b). While accumulation of the nanobrick IONPs in the presence of an external magnetic field was significantly greater in the endothelial cells compared to the epithelial cell line, there was no apparent differences between endothelial cells from different vascular beds (Figure 5.2b). TEM of the various cell preparations confirmed that nanospheres were loosely bound on the cell surface and not internalized by bEnd.3 cells (Figure 5.3a) or human hepatocellular liver carcinoma cell line HepG2 (Figure 5.3b). By contrast, large amounts of nanobricks were found inside the bEnd.3 endothelial cells (Figure 5.3c) but few were found inside HepG2 (Figure 5.3d) or MDCK epithelial cell lines (Figure 5.3e), confirming the finding that the nanobricks were selectively internalized in endothelial cells.

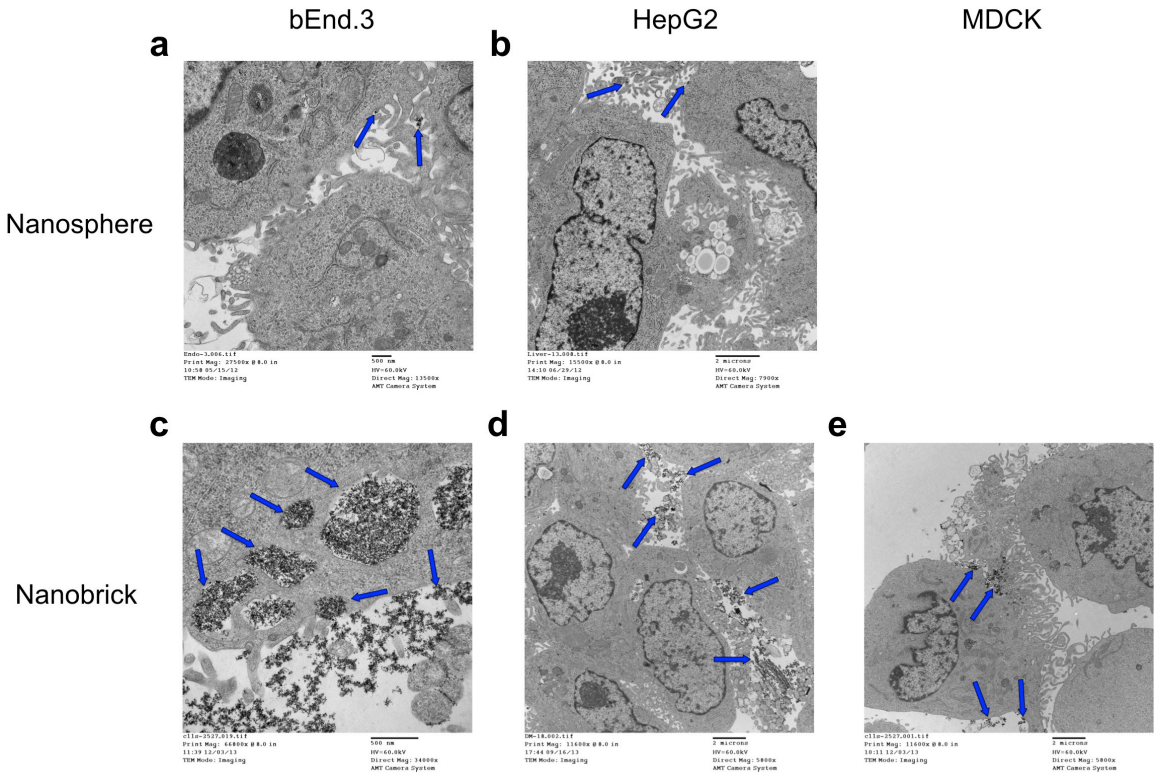


**Figure 5.3 Representative TEM images of nanospheres (a, b) and nanobricks (c, d, e) in bEnd.3 (a, c), HepG2 (b, d), and MDCK cells (e). The arrows point to nanoparticles.**

### 5.3.3 Internalization of nanobrick in bEnd.3 cells via caveolae mediated endocytosis

To understand the selectivity of nanobricks to endothelial cells, we examined the potential mechanism of internalization via endocytosis. Confluent bEnd.3 cell monolayers were pretreated with inhibitors for clathrin mediated endocytosis (chlorpromazine), caveolae mediated endocytosis (MβCD, genistein), macropinocytosis (cytochalasin D), and endosome maturation (monensin) for 30 min, and uptake of nanobricks at 100 μg/mL was determined (Figure 5.4a). There was a significant inhibition of nanobrick uptake in the MβCD and genistein treatment groups (Figure 5.4a). These findings were confirmed in TEM studies showing diminished IONP association in bEnd3 in the presence of genistein compared to controls receiving the nanobricks

alone (Figure 5.4b,c). None of the other treatment groups examined significantly impacted on nanobrick accumulation in bEnd3 cells (Figure 5.4a). This suggested that nanobrick internalization in bEnd.3 cells was mediated via a caveolae dependent endocytosis pathway.

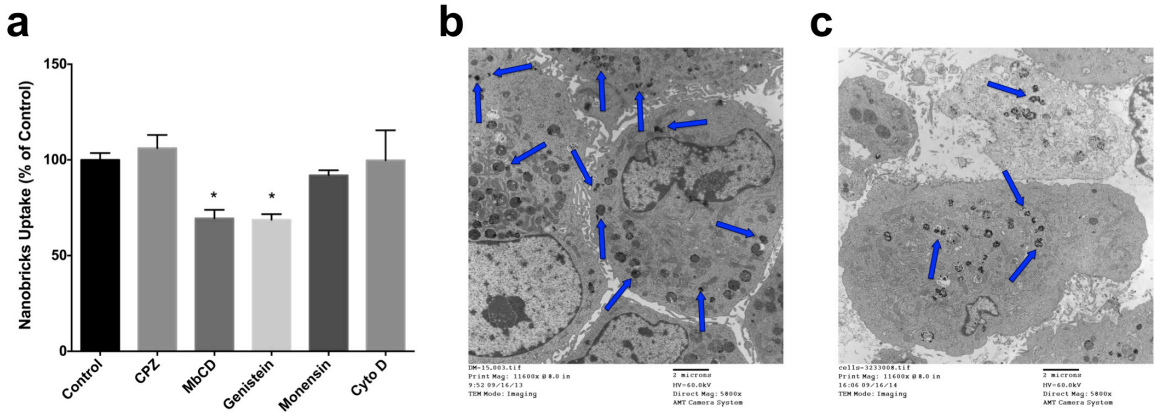


**Figure 5.4 Effect of various endocytosis inhibitors on cellular uptake of nanobricks in bEnd.3 cells. The internalization of nanobricks was significantly decreased by treatment with MβCD and Genistein, inhibitors of caveolae mediated endocytosis. This is confirmed by representative TEM that shows substantially greater internalization of nanobricks under control conditions (b) compared to cells treated with genistein (c). The arrows point to nanoparticles. Values represent the mean ± SEM for three cell monolayers per treatment group; * $p<0.05$ compared to control.**

To ascertain whether elevated caveolae mediated endocytosis in endothelial cells contributes to the selective internalization of nanobricks observed in endothelial cells, additional studies were performed with known markers of caveolae-mediated endocytosis. The uptake of CTB and BSA is 6-fold and 12-fold greater in bEnd.3 cells than MDCK cells, respectively. (Figure 5.5a) The increase in uptake of CTB and BSA in the bEnd3 was correlated with an increase in the expression of caveolin-1 compared to epithelial MDCK cell line. Expression of caveolin-1 in another endothelial cell line hCMEC/D3 was also elevated. (Data not shown) Additional evidence of potential interaction of nanobricks in caveolae-mediated endocytosis is the ability of the nanobricks to inhibit the uptake of fluorescently-labeled BSA in a concentration dependent manner. (Figure 5.5b)

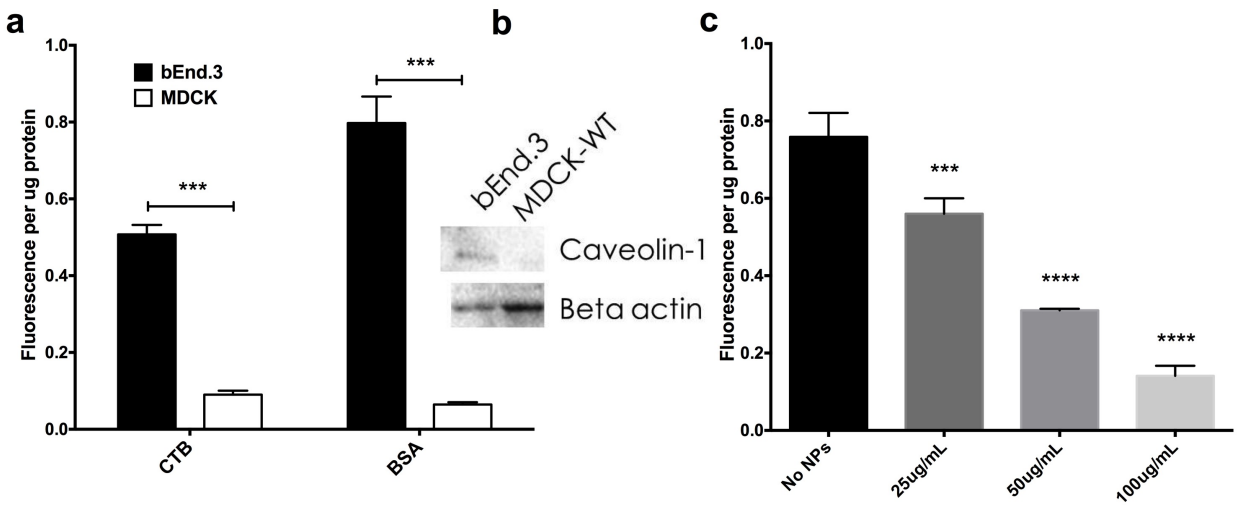


**Figure 5.5 Probing caveolae mediated endocytosis pathway in bEnd.3 and MDCK cells using fluorescently labeled BSA and CTB (markers for caveolae-mediated uptake). Caveolae-mediated pathway is prominent in bEnd.3 cells and significantly lower in MDCK cells (a). Western blot analysis shows higher level of caveolin-1 expression on bEnd.3 cells (b). The ability of nanobricks to inhibit the uptake of fluorescently labeled BSA and CTB in bEnd.3 cells suggests a competitive binding of the nanobricks to the caveolae (c). Values are expressed as the mean ± SEM for three cell monolayers per treatment group. *** indicate $p<0.001$, **** indicate $p<0.0001$.**

## 5.4 Discussion

Previous studies by our laboratory and others[53-55,266] have demonstrated the importance of surface charge of IONPs for cellular uptake. In the present study, negatively charged IONP of different shape were utilized to examine the influence of shape on cellular uptake. While there are some publications regarding the synthesis of different shaped IONPs[335,336], these methods are typically thermal decomposition based generating nanoparticles that are not directly dispersible in water and therefore not readily amenable to cell based interactions. With regards to the possible impact of IONP shape on cell uptake, to date the shape-dependent impact on the bio-based applications have been limited to macrophages[337]. The current studies are the first to demonstrate a shape related effect on IONP accumulation in endothelial cells. Our results demonstrated that brick shaped IONPs were preferentially taken up by endothelial cells compared to sphere shaped IONP with identical surface coatings. In addition, when studies were performed in the presence of a magnetic field, the endothelial sensitivity for nanobrick accumulation was even more apparent, being substantially greater than epithelial cell preparations. The selective uptake of the nanobricks by endothelial cells appears to be due to caveolae-mediated endocytosis, which is more prevalent in endothelial cells compared to epithelial cells examined.

As the nanobricks are slightly larger than the nanospheres (15 x 10 x 5nm for nanobricks vs 8nm diameter nanospheres), there is a possibility that differences in size may also contribute to the increased accumulation of IONP nanobricks in the endothelial cells. Previous studies demonstrated a size dependent effect on IONP accumulation in the Caucasian colon adenocarcinoma cell line (Caco2)[44]. However, it should be noted that those IONP had a positive surface charge and were considerably larger (30 - 100 nm core diameter) than the IONP used in

the present study. Given the EDT surface coating used in the present study, the studies of Saito et al., 2012 reporting no size dependent effect on the accumulation of negatively charged IONP in cells may be more relevant. In this study, the cellular uptake of alkali-treated dextran coated IONPs (-15mV zeta potential) with particle sizes of 28 and 74 nm, were compared to that of carboxymethyl dextran IONPs (-24mV zeta potential) of similar size in a macrophage cell line, RAW264. While there was a clear surface charge dependency in cell accumulation, with the alkali-treated dextran coated IONPs having greater accumulation than the carboxymethyl dextran coated IONPs, no significant difference was found in the cellular accumulation of the large (74 nm diameter) and small (28 nm diameter) IONPs of the same coating[58]. Taken together, these studies would suggest that for the negatively charged particles with low membrane association, size is not the predominant factor for determining cellular accumulation.

We found that brick shaped IONPs could enhance the affinity between surface coating and cell membrane modality. An increased contact area with the cell surface provides potentially more sites for interaction and has been previously identified as an important contributor to enhance nanoparticle targeting effects[338]. Our finding is in line with recent publications of shape related effect on polystyrene NPs. Barua et al., 2013 reported that rod shaped polystyrene NPs have enhanced antibody binding specificity to three breast cancer cell lines compared to spherical and disk shaped NPs[62]. Using *in silico* and *in vivo* approaches, Kohlar and colleagues demonstrated rod shaped polystyrene NPs with antibody against intracellular adhesion molecule (ICAM) or transferrin receptor exhibit higher internalization in brain and lung endothelial cells than spherical counterparts under flow conditions[339]. Hence, it is speculated that by changing the IONPs from sphere to brick, the negatively charged surface coating interacts with multiple discrete sites on the cell membrane that contributes to the selective binding of the nanobricks to

endothelial cells. This may provide advantages especially when second-generation nanobrick compositions are created that have additional endothelial ligand targeting capabilities. We further hypothesize that a low affinity ligand grafted on nanobrick surface would exhibit a stronger interaction to its receptor than grafted on nanospheres. Such studies are currently ongoing.

Of the various vesicular internalization processes, caveolae mediated endocytosis is predominantly found in endothelial cells[340]. Therefore, targeting to endothelial cells may be achieved by interacting with caveolae localized in lipid rafts within the plasma membrane. The current study certainly points to a caveolae-mediated mechanism for the endothelial selective uptake of the nanobrick IONP. The evidence in support of this is the increased expression of caveolin in endothelial cells compared to the epithelial cells and the ability of inhibitors of caveolae-mediated uptake to significantly reduce nanobrick IONP accumulation in endothelial cells. In addition, the nanobrick IONPs were able to prevent the cellular uptake of two macromolecules, CTB and BSA, which are known to enter into endothelial cells through caveolae-mediated endocytosis in a concentration dependent manner consistent with competitive inhibition of caveolae biding sites. Previous studies grafting anionic polyelectrolytes of varied hydrophobicity to nanospheres reported endothelial cell targeting of NPs via a caveolae-mediated endocytic process[341]. These findings together suggest that non-spherical nanoparticles with negative surface charges are likely to have the greatest affinity for caveolae-based uptake.

Caveolae are formed by a group of caveolin protein binding to cholesterol in the lipid raft region of the cell membrane[89]. Although surface chemistry and functional groups can influence IONP cell interaction, it has been reported that negatively charged IONPs can interact with cationic lipid domains in the lipid raft[95]. Caveolae are enriched in endothelial cells and present in muscle, fibroblast, and adipocytes[91]. Following the pinch off of caveolae from the lipid raft, the

fate of caveolae is dependent on the cell type in which endocytosis occurs. In non-endothelial cells, caveolae are subjected to endolysosomal system. In endothelial cells, caveolae may bypass the lysosome and transport cargo through vesicular processes across the endothelial cell layer[87,92]. For this reason, the nanobrick IONPs may potentially be exploited for drug and gene delivery applications to tissues underlying endothelial cells such as the brain. These studies are currently ongoing.

Compared to nanospheres, the nanobricks have an increased responsiveness in an applied magnetic field gradient. Based on the modeling and simulation data, (the nanobricks have a preferred direction of magnetization along their largest dimension (see Supplementary Information) As such, an externally applied magnetic field will act to more preferentially align the smaller dimensions of the nanobricks along the cell surface, decreasing the area of interaction and thus limiting the effect of the steric repulsion between the cell surface and nanobrick coating. The proposed behavior of the nanobricks in the externally applied magnetic field may help explain the significant increase in uptake of the nanobricks compared to the nanosphere observed in the presence of a magnetic gradient in the present study. In addition to the potential for tissue targeting using external magnetic fields, the magnetic properties of the nanobricks made them ideal candidates for magnet resonance imaging agents. Nanobricks show large and constant transverse relaxivity ($r_2$) for medium and high-field MRI compared to gadolinium based contrast agents that peaks at 20 MHz and decreases quickly with high magnetic fields[320].

The preferential uptake of nanobrick IONPs within vascular endothelial cells combined with the enhanced targeting through application of external magnetic fields has several potential therapeutic applications. The ability to target to the endothelial cells within tumor microvasculature is a prime application for this technology platform. It is generally accepted that

angiogenesis is crucial for tumor growth, evasion and metastasis[342]. The creation of new blood vessels to supply oxygen and nutrients to tumor cells is a necessary requirement for solid organ tumor growth. Thus, anti-angiogenesis therapy has emerged as a viable treatment strategy to control tumor growth. Recent studies demonstrated the potential of PEG-PLGA nanoparticles for tumor neo-vasculature and tumor cells dual-targeting drug delivery[343]. The ability to focus an external magnetic field within the tumor stroma will not only increase the local concentration of IONPs but also facilitate improved internalization of nanobrick IONPs in endothelial cells. An anticipated result of such focused targeting of the IONPs would be enhanced delivery and potential destruction of the tumor neovasculature. While current anti-angiogenic therapies have been limited in the clinic due to the development of resistance[344], the targeting of nanobrick IONPs to endothelial cells using shape and magnetic fields would make resistance to these delivery vehicles less probable.

## 5.5 Conclusion

Nanoparticle shape plays an important role in the cellular internalization process. Targeting nanoparticles to endothelial cells can be achieved by modification of shape from a sphere to a brick. Nanobricks exhibited an improved cellar uptake profile compared to nanospheres despite a negative surface charge. The larger overall magnetization of the nanobricks resulted in an enhanced uptake in the presence of an external magnetic field. The preferential uptake of nanobricks in endothelial cells was mediated via caveolae dependent endocytosis. Our results demonstrate that shape modification offers a general approach to achieve targeted delivery.

# Chapter 6 Conclusion

## 6.1 Conclusion

It has been estimated that less than 2% of the compounds in the current drug discovery pipeline have sufficient BBB permeability to actually enter the brain in therapeutically relevant amounts[345]. For example, many anticancer drugs, including paclitaxel, are ineffective in the treatment of brain tumors, mainly due to poor BBB permeability, and the inability to reach therapeutic concentrations at the tumor site[311,346]. While the newer kinase inhibitors are more selective in producing tumor cell toxicity, achieving adequate BBB permeability with these agents remains a problem and further highlights the need for improved methods for delivering therapeutics to brain tumors. Therefore, there is an urgent need to focus on ways to deliver the drugs to the brain in addition to the never ending quest for new and effective treatments for CNS diseases.

This thesis characterized and identified important properties that govern the cellular uptake, permeability and toxicity of IONPs. Such information is important to advance IONPs as a potential drug delivery platform for brain related applications. To ensure IONPs were not causing significant toxic effects on various brain related cells, we established the biocompatibility and cell accumulation of both positively and negatively charged IONPs in cultured brain endothelial cells, and primary mouse neurons and astrocytes. Acute toxicity studies showed that both IONP compositions were well tolerated at concentrations below 100μg/ml. At concentrations above 100μg/ml, neurons appeared to be more sensitive to the positively charged IONPs, while astrocytes were more sensitive to the negatively charged IONPs. Brain endothelial cells showed no signs of toxicity with either of IONPs at any

concentrations examined (0.1 – 225 ug/mL). An important observation from these studies was that positively charged IONPs have a greater uptake profile than negatively charged IONPs in all cell types tested. Application of a magnetic field enhanced the cellular uptake of both IONP compositions.

This finding, which positive surface charges lead to increased cellular uptake, became a key part of the current delivery approach involving MECD of IONPs across a transiently opened BBB. Transient opening of the BBB in conjunction with MFECD is a unique approach that is scientifically different from the most applications that are trying to boost transcellular transport of the nanoparticles. We believe that the disruption of the BBB will help to overcome the challenges when translating ligand-targeted nanomedicine to the clinical setting. Our *in vitro* proof of concept study demonstrated the feasibility of MFECD approach for enhancing IONPs across the BBB model. There was a significant increase in permeability of EDT-IONPs across the disrupted brain endothelial cells compared to a normal brain endothelial monolayer and this effect was most prominent when an external magnetic field was present.

Using a mouse model, we examined the biodistribution of EDT-IONPs and the ability to deliver them into mouse brain combining magnetic field and LPA induced BBB disruption. In this study, we found liver and spleen were the major organs of IONP deposition. There was limited distribution of IONPs in lung and brain under normal conditions. The 3.6% of injected dose of EDT-IONPs that accumulated in the mouse brain parenchyma within 20 minutes disruption window by LPA represents a 3-6 fold increase compared to various ligand targeted vesicular transport approaches reported in literature. Furthermore, immunofluorescence examination of brain slices of LPA and IONP treated mice revealed no sign of peripheral immune cell infiltration or activation of microglia and astrocytes. This suggested transient BBB

disruption and enhanced IONP delivery to the brain did not lead to inflammation or toxicity. Our findings support the potential use of MFECD approach to enhance brain delivery of EDT-IONPs via transient disruption of the BBB as a safe and effective method.

The majority of IONP research involves spherical nanoparticles. Recent advances in synthesis techniques have enabled creation of brick shaped IONPs. We studied the uptake of brick and sphere shaped EDT-IONPs in various endothelial and epithelial cells. Nanobricks showed improved cellular uptake profiles compared to nanospheres in spite of negative surface charge. The increased magnetic response of the nanobricks resulted in enhanced uptake in the presence of an applied magnetic field. Mechanism governing the increased uptake of nanobricks involves preferential utilization of caveolae dependent endocytosis pathways present within the endothelial cells. This study highlights that shape modification offers a general approach to achieve targeted delivery to endothelial cells.

## 6.2 Future directions

In chapter 4, we hypothesized that the magnetic targeting effect would enhance the brain localization of EDT-IONPs in mice. However, the presence of an external magnet did not lead to an increase in brain accumulation of IONPs. This might be due to the fact that the small size and rather low magnetic moments of IONPs requires a larger magnetic gradient than the current set-up can provide. In chapter 5, it was demonstrated that nanobricks have an increased responsiveness in an applied magnetic field gradient compared to sphere shaped EDT-IONPs. Therefore, we can extend MFECD approach to nanobricks. The disruption window of LPA is only 20 minutes. Our lab is currently investigating different cadherin peptides and their ability to modulate the BBB integrity[319,347]. The advantages of cadherin peptides include rapid onset, reversible, and controlled window of opening. There are now a number of cadherin peptides that can bind to the external domain of cadherin and open the tight junction of the BBB for periods of time that range from 1 to 4 hours. Cadherin peptides may therefore be ideal for MFECD approach with nanobricks, as the duration of BBB modulation can be adjusted to match circulating half-lifes of the next generation IONPs. More importantly, in preliminary experiments examining the permeability of nanobricks across the *in vitro* BBB model, disruption of tight junctions with a cadherin peptide followed by application of an external magnetic field greatly enhanced the permeability of the iron oxide nanobricks. (Figure 6.1) Of note, no significant differences were found between the permeability of the 70,000 MWT dextran across the disrupted monolayer compared to that of intact monolayer. This observation suggests that cadherin peptide modulate the BBB permeability in a size-controlled fashion. Furthermore, there is minimal permeability of nanobricks across the intact brain endothelial monolayer with or without magnetic field. In absence of a magnetic field, nanobricks cannot cross the cadherin

peptide disrupted BBB model. However, magnetic field was able to pull the nanobricks across to a greater extent than the macromolecule permeability marker.

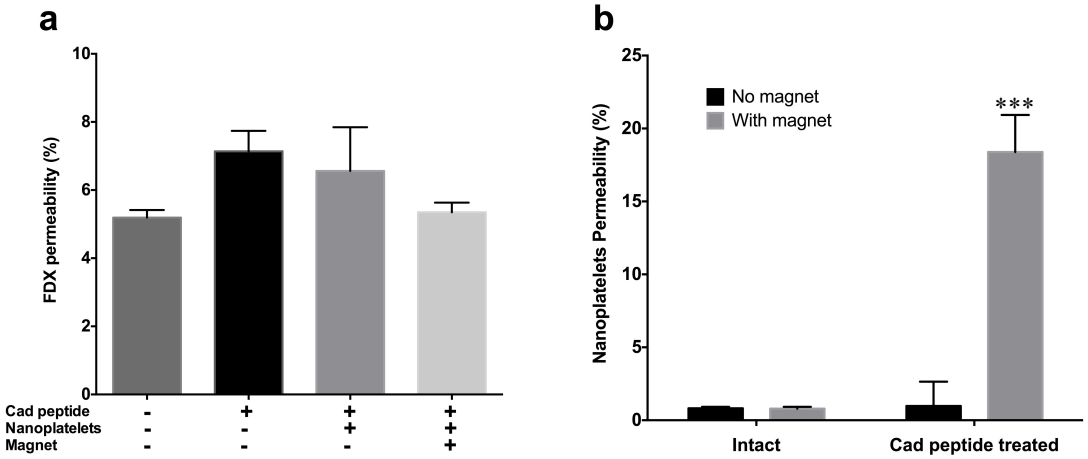


**Figure 6.1 Permeability of FDX-70000 (a) and nanobricks (b) across intact and cadherin peptide disrupted bEnd.3 cell monolayers in presence and absence of a magnetic field. *** indicate $p < 0.001$ compared to cadherin treatment group without magnetic field.**

A transcytosis approach to deliver nanobricks to mouse brain through a caveolae-mediated endocytosis process may also be feasible. It has been reported that the caveolae dependent endocytosis can be used to transport nanoparticles across the vascular endothelium[348]. It would be interesting to see if nanobricks internalized in endothelial cells would transport across the BBB.

The efficacy of using IONPs as drug delivery platform is the next step in the development of this technology. Given the relative unresponsiveness of brain tumors to most chemotherapeutic agents and limited BBB permeability, application of IONP for delivering cancer drugs to brain tumors would seem an appropriate next step. Surface modification of IONPs could also be made to allow encapsulation of a variety of drugs. An example of such surface coatings would be the Pluronic$^{TM}$ block copolymers. The wide range of hydrophobic and hydrophilic Pluronic compositions ensures that a proper balance can be identified for drug

loading and release from the IONP[349]. The Pluronic polymers have been used for enhanced delivery and improved toxicity profile of several anticancer agents including doxorubicin and paclitaxel. Proof-of-concept experiments for IONPs based anticancer drug delivery would be an application for this technology. *In vitro* studies regarding drug loading and release followed by *in vivo* studies in normal and brain tumor-bearing mice will be needed to establish the bio-distribution and biocompatibility of selected IONP compositions and to determine the effectiveness of MEFCD approach for the delivery of IONP in the treatment of tumors in a mouse brain tumor model.

# Chapter 7 Reference


1. Walter P, Welcomme E, Hallegot P, et al. Early use of PbS nanotechnology for an ancient hair dyeing formula. *Nano Lett.* Oct 2006;6(10):2215-2219.
2. Santamaria A. Historical overview of nanotechnology and nanotoxicology. *Methods Mol Biol.* 2012;926:1-12.
3. Bellusci M, La Barbera A, Padella F, et al. Biodistribution and acute toxicity of a nanofluid containing manganese iron oxide nanoparticles produced by a mechanochemical process. *Int J Nanomedicine.* 2014;9:1919-1929.
4. Horev-Azaria L, Baldi G, Beno D, et al. Predictive toxicology of cobalt ferrite nanoparticles: comparative in-vitro study of different cellular models using methods of knowledge discovery from data. *Part Fibre Toxicol.* 2013;10:32.
5. Lam T, Pouliot P, Avti PK, Lesage F, Kakkar AK. Superparamagnetic iron oxide based nanoprobes for imaging and theranostics. *Adv Colloid Interface Sci.* Nov 2013;199-200:95-113.
6. Zhang W. Nanoparticle aggregation: principles and modeling. *Adv Exp Med Biol.* 2014;811:19-43.
7. Bae JE, Huh MI, Ryu BK, et al. The effect of static magnetic fields on the aggregation and cytotoxicity of magnetic nanoparticles. *Biomaterials.* Dec 2011;32(35):9401-9414.
8. Saptarshi SR, Duschl A, Lopata AL. Interaction of nanoparticles with proteins: relation to bio-reactivity of the nanoparticle. *J Nanobiotechnology.* 2013;11:26.
9. Mahmoudi M, Shokrgozar MA, Behzadi S. Slight temperature changes affect protein affinity and cellular uptake/toxicity of nanoparticles. *Nanoscale.* Apr 21 2013;5(8):3240-3244.
10. Sakulkhu U, Mahmoudi M, Maurizi L, Salaklang J, Hofmann H. Protein corona composition of superparamagnetic iron oxide nanoparticles with various physico-chemical properties and coatings. *Sci Rep.* 2014;4:5020.
11. Ashby J, Pan S, Zhong W. Size and surface functionalization of iron oxide nanoparticles influence the composition and dynamic nature of their protein corona. *ACS Appl Mater Interfaces.* Sep 10 2014;6(17):15412-15419.
12. Torrisi V, Graillot A, Vitorazi L, et al. Preventing corona effects: multiphosphonic acid poly(ethylene glycol) copolymers for stable stealth iron oxide nanoparticles. *Biomacromolecules.* Aug 11 2014;15(8):3171-3179.
13. Amiri H, Bordonali L, Lascialfari A, et al. Protein corona affects the relaxivity and MRI contrast efficiency of magnetic nanoparticles. *Nanoscale.* Sep 21 2013;5(18):8656-8665.
14. Calatayud MP, Sanz B, Raffa V, Riggio C, Ibarra MR, Goya GF. The effect of surface charge of functionalized Fe3O4 nanoparticles on protein adsorption and cell uptake. *Biomaterials.* Aug 2014;35(24):6389-6399.
15. Mahmoudi M, Sheibani S, Milani AS, et al. Crucial role of the protein corona for the specific targeting of nanoparticles. *Nanomedicine (Lond).* Jan 2015;10(2):215-226.
16. Couto D, Freitas M, Carvalho F, Fernandes E. Iron Oxide Nanoparticles: an Insight into their Biomedical Applications. *Curr Med Chem.* Mar 11 2015.
17. Frohlich E. Cellular targets and mechanisms in the cytotoxic action of non-biodegradable engineered nanoparticles. *Curr Drug Metab.* Nov 2013;14(9):976-988.

18. Jahn MR, Nawroth T, Futterer S, Wolfrum U, Kolb U, Langguth P. Iron oxide/hydroxide nanoparticles with negatively charged shells show increased uptake in Caco-2 cells. *Mol Pharm.* Jun 4 2012;9(6):1628-1637.
19. Arosio P, Ingrassia R, Cavadini P. Ferritins: a family of molecules for iron storage, antioxidation and more. *Biochim Biophys Acta.* Jul 2009;1790(7):589-599.
20. Laskar A, Ghosh M, Khattak SI, Li W, Yuan XM. Degradation of superparamagnetic iron oxide nanoparticle-induced ferritin by lysosomal cathepsins and related immune response. *Nanomedicine (Lond).* May 2012;7(5):705-717.
21. Hohnholt MC, Geppert M, Dringen R. Treatment with iron oxide nanoparticles induces ferritin synthesis but not oxidative stress in oligodendroglial cells. *Acta Biomater.* Nov 2011;7(11):3946-3954.
22. Lopez-Castro JD, Maraloiu AV, Delgado JJ, et al. From synthetic to natural nanoparticles: monitoring the biodegradation of SPIO (P904) into ferritin by electron microscopy. *Nanoscale.* Nov 2011;3(11):4597-4599.
23. Hohnholt MC, Geppert M, Luther EM, Petters C, Bulcke F, Dringen R. Handling of iron oxide and silver nanoparticles by astrocytes. *Neurochem Res.* Feb 2013;38(2):227-239.
24. Hohnholt MC, Dringen R. Uptake and metabolism of iron and iron oxide nanoparticles in brain astrocytes. *Biochem Soc Trans.* Dec 2013;41(6):1588-1592.
25. Voinov MA, Sosa Pagan JO, Morrison E, Smirnova TI, Smirnov AI. Surface-mediated production of hydroxyl radicals as a mechanism of iron oxide nanoparticle biotoxicity. *J Am Chem Soc.* Jan 12 2011;133(1):35-41.
26. Luo C, Li Y, Yang L, Wang X, Long J, Liu J. Superparamagnetic iron oxide nanoparticles exacerbate the risks of reactive oxygen species-mediated external stresses. *Arch Toxicol.* Mar 2015;89(3):357-369.
27. Mesarosova M, Kozics K, Babelova A, et al. The role of reactive oxygen species in the genotoxicity of surface-modified magnetite nanoparticles. *Toxicol Lett.* May 2 2014;226(3):303-313.
28. Park EJ, Umh HN, Choi DH, et al. Magnetite- and maghemite-induced different toxicity in murine alveolar macrophage cells. *Arch Toxicol.* Aug 2014;88(8):1607-1618.
29. Muller K, Skepper JN, Posfai M, et al. Effect of ultrasmall superparamagnetic iron oxide nanoparticles (Ferumoxtran-10) on human monocyte-macrophages in vitro. *Biomaterials.* Mar 2007;28(9):1629-1642.
30. Hanini A, Schmitt A, Kacem K, Chau F, Ammar S, Gavard J. Evaluation of iron oxide nanoparticle biocompatibility. *Int J Nanomedicine.* 2011;6:787-794.
31. Amna T, Van Ba H, Vaseem M, et al. Apoptosis induced by copper oxide quantum dots in cultured C2C12 cells via caspase 3 and caspase 7: a study on cytotoxicity assessment. *Appl Microbiol Biotechnol.* Jun 2013;97(12):5545-5553.
32. Zhang XQ, Yin LH, Tang M, Pu YP. ZnO, TiO(2), SiO(2,) and Al(2)O(3) nanoparticles-induced toxic effects on human fetal lung fibroblasts. *Biomed Environ Sci.* Dec 2011;24(6):661-669.
33. Sun J, Wang S, Zhao D, Hun FH, Weng L, Liu H. Cytotoxicity, permeability, and inflammation of metal oxide nanoparticles in human cardiac microvascular endothelial cells: cytotoxicity, permeability, and inflammation of metal oxide nanoparticles. *Cell Biol Toxicol.* Oct 2011;27(5):333-342.

34. Lai JC, Lai MB, Jandhyam S, et al. Exposure to titanium dioxide and other metallic oxide nanoparticles induces cytotoxicity on human neural cells and fibroblasts. *Int J Nanomedicine.* 2008;3(4):533-545.
35. Yu M, Huang S, Yu KJ, Clyne AM. Dextran and polymer polyethylene glycol (PEG) coating reduce both 5 and 30 nm iron oxide nanoparticle cytotoxicity in 2D and 3D cell culture. *Int J Mol Sci.* 2012;13(5):5554-5570.
36. Lindemann A, Ludtke-Buzug K, Fraderich BM, Grafe K, Pries R, Wollenberg B. Biological impact of superparamagnetic iron oxide nanoparticles for magnetic particle imaging of head and neck cancer cells. *Int J Nanomedicine.* 2014;9:5025-5040.
37. Kim JS, Yoon TJ, Yu KN, et al. Toxicity and tissue distribution of magnetic nanoparticles in mice. *Toxicol Sci.* Jan 2006;89(1):338-347.
38. Yang L, Kuang H, Zhang W, et al. Size dependent biodistribution and toxicokinetics of iron oxide magnetic nanoparticles in mice. *Nanoscale.* Jan 14 2015;7(2):625-636.
39. Magdolenova Z, Drlickova M, Henjum K, et al. Coating-dependent induction of cytotoxicity and genotoxicity of iron oxide nanoparticles. *Nanotoxicology.* May 2015;9 Suppl 1:44-56.
40. Hoskins C, Cuschieri A, Wang L. The cytotoxicity of polycationic iron oxide nanoparticles: common endpoint assays and alternative approaches for improved understanding of cellular response mechanism. *J Nanobiotechnology.* 2012;10:15.
41. Hong SC, Lee JH, Lee J, et al. Subtle cytotoxicity and genotoxicity differences in superparamagnetic iron oxide nanoparticles coated with various functional groups. *Int J Nanomedicine.* 2011;6:3219-3231.
42. Di Bona KR, Xu Y, Ramirez PA, et al. Surface charge and dosage dependent potential developmental toxicity and biodistribution of iron oxide nanoparticles in pregnant CD-1 mice. *Reprod Toxicol.* Dec 2014;50:36-42.
43. Guadagnini R, Moreau K, Hussain S, Marano F, Boland S. Toxicity evaluation of engineered nanoparticles for medical applications using pulmonary epithelial cells. *Nanotoxicology.* May 2015;9 Suppl 1:25-32.
44. Zhang W, Kalive M, Capco DG, Chen Y. Adsorption of hematite nanoparticles onto Caco-2 cells and the cellular impairments: effect of particle size. *Nanotechnology.* Sep 3 2010;21(35):355103.
45. Yu SS, Lau CM, Thomas SN, et al. Size- and charge-dependent non-specific uptake of PEGylated nanoparticles by macrophages. *Int J Nanomedicine.* 2012;7:799-813.
46. Roohi F, Lohrke J, Ide A, Schutz G, Dassler K. Studying the effect of particle size and coating type on the blood kinetics of superparamagnetic iron oxide nanoparticles. *Int J Nanomedicine.* 2012;7:4447-4458.
47. Nakamura H, Jun F, Maeda H. Development of next-generation macromolecular drugs based on the EPR effect: challenges and pitfalls. *Expert Opin Drug Deliv.* Jan 2015;12(1):53-64.
48. Maeda H. Vascular permeability in cancer and infection as related to macromolecular drug delivery, with emphasis on the EPR effect for tumor-selective drug targeting. *Proc Jpn Acad Ser B Phys Biol Sci.* 2012;88(3):53-71.
49. C ND, Tate JA, Kett WC, et al. Tumor cell targeting by iron oxide nanoparticles is dominated by different factors in vitro versus in vivo. *PLoS ONE.* 2015;10(2):e0115636.

50. Mori Y, Umeda M, Fukunaga M, Ogasawara K, Yoshioka Y. MR contrast in mouse lymph nodes with subcutaneous administration of iron oxide particles: size dependency. *Magn Reson Med Sci.* 2011;10(4):219-227.
51. Kjellman P, in 't Zandt R, Fredriksson S, Strand SE. Optimizing retention of multimodal imaging nanostructures in sentinel lymph nodes by nanoscale size tailoring. *Nanomed.* Jul 2014;10(5):1089-1095.
52. Pouw JJ, Ahmed M, Anninga B, et al. Comparison of three magnetic nanoparticle tracers for sentinel lymph node biopsy in an in vivo porcine model. *Int J Nanomedicine.* 2015;10:1235-1243.
53. Zhu XM, Wang YX, Leung KC, et al. Enhanced cellular uptake of aminosilane-coated superparamagnetic iron oxide nanoparticles in mammalian cell lines. *Int J Nanomedicine.* 2012;7:953-964.
54. Ge Y, Zhang Y, Xia J, et al. Effect of surface charge and agglomerate degree of magnetic iron oxide nanoparticles on KB cellular uptake in vitro. *Colloids Surf B Biointerfaces.* Oct 15 2009;73(2):294-301.
55. Villanueva A, Canete M, Roca AG, et al. The influence of surface functionalization on the enhanced internalization of magnetic nanoparticles in cancer cells. *Nanotechnology.* Mar 18 2009;20(11):115103.
56. Schweiger C, Hartmann R, Zhang F, Parak WJ, Kissel TH, Rivera Gil P. Quantification of the internalization patterns of superparamagnetic iron oxide nanoparticles with opposite charge. *J Nanobiotechnology.* 2012;10:28.
57. Ayala V, Herrera AP, Latorre-Esteves M, Torres-Lugo M, Rinaldi C. Effect of surface charge on the colloidal stability and in vitro uptake of carboxymethyl dextran-coated iron oxide nanoparticles. *J Nanopart Res.* Aug 1 2013;15(8):1874.
58. Saito S, Tsugeno M, Koto D, et al. Impact of surface coating and particle size on the uptake of small and ultrasmall superparamagnetic iron oxide nanoparticles by macrophages. *Int J Nanomedicine.* 2012;7:5415-5421.
59. Elias DR, Poloukhtine A, Popik V, Tsourkas A. Effect of ligand density, receptor density, and nanoparticle size on cell targeting. *Nanomed.* Feb 2013;9(2):194-201.
60. Fiandra L, Mazzucchelli S, De Palma C, et al. Assessing the in vivo targeting efficiency of multifunctional nanoconstructs bearing antibody-derived ligands. *ACS Nano.* Jul 23 2013;7(7):6092-6102.
61. Chauhan VP, Popovic Z, Chen O, et al. Fluorescent nanorods and nanospheres for real-time in vivo probing of nanoparticle shape-dependent tumor penetration. *Angew Chem Int Ed Engl.* Nov 25 2011;50(48):11417-11420.
62. Barua S, Yoo JW, Kolhar P, Wakankar A, Gokarn YR, Mitragotri S. Particle shape enhances specificity of antibody-displaying nanoparticles. *Proc Natl Acad Sci U S A.* Feb 26 2013;110(9):3270-3275.
63. Shah S, Liu Y, Hu W, Gao J. Modeling particle shape-dependent dynamics in nanomedicine. *J Nanosci Nanotechnol.* Feb 2011;11(2):919-928.
64. Huang X, Teng X, Chen D, Tang F, He J. The effect of the shape of mesoporous silica nanoparticles on cellular uptake and cell function. *Biomaterials.* Jan 2010;31(3):438-448.
65. Arnida, Janat-Amsbury MM, Ray A, Peterson CM, Ghandehari H. Geometry and surface characteristics of gold nanoparticles influence their biodistribution and uptake by macrophages. *Eur J Pharm Biopharm.* Apr 2011;77(3):417-423.

66. Huang X, Li L, Liu T, et al. The shape effect of mesoporous silica nanoparticles on biodistribution, clearance, and biocompatibility in vivo. *ACS Nano.* Jul 26 2011;5(7):5390-5399.
67. Decuzzi P, Godin B, Tanaka T, et al. Size and shape effects in the biodistribution of intravascularly injected particles. *J Control Release.* Feb 15 2010;141(3):320-327.
68. Levy M, Luciani N, Alloyeau D, et al. Long term in vivo biotransformation of iron oxide nanoparticles. *Biomaterials.* Jun 2011;32(16):3988-3999.
69. Guarnieri D, Sabella S, Muscetti O, et al. Transport across the cell-membrane dictates nanoparticle fate and toxicity: a new paradigm in nanotoxicology. *Nanoscale.* Sep 7 2014;6(17):10264-10273.
70. Beddoes CM, Case CP, Briscoe WH. Understanding nanoparticle cellular entry: A physicochemical perspective. *Adv Colloid Interface Sci.* Apr 2015;218:48-68.
71. Xu H, Dai W, Han Y, et al. Differential internalization of superparamagnetic iron oxide nanoparticles in different types of cells. *J Nanosci Nanotechnol.* Nov 2010;10(11):7406-7410.
72. Cleal K, He L, Watson PD, Jones AT. Endocytosis, intracellular traffic and fate of cell penetrating peptide based conjugates and nanoparticles. *Curr Pharm Des.* 2013;19(16):2878-2894.
73. Militello RD, Colombo MI. A membrane is born: origin of the autophagosomal compartment. *Curr Mol Med.* Apr 2011;11(3):197-203.
74. Murugan K, Choonara YE, Kumar P, Bijukumar D, du Toit LC, Pillay V. Parameters and characteristics governing cellular internalization and trans-barrier trafficking of nanostructures. *Int J Nanomedicine.* 2015;10:2191-2206.
75. Sahay G, Alakhova DY, Kabanov AV. Endocytosis of nanomedicines. *J Control Release.* Aug 3 2010;145(3):182-195.
76. Lojk J, Bregar VB, Rajh M, et al. Cell type-specific response to high intracellular loading of polyacrylic acid-coated magnetic nanoparticles. *Int J Nanomedicine.* 2015;10:1449-1462.
77. Bohmer N, Jordan A. Caveolin-1 and CDC42 mediated endocytosis of silica-coated iron oxide nanoparticles in HeLa cells. *Beilstein J Nanotechnol.* 2015;6:167-176.
78. Nichols BJ. GM1-containing lipid rafts are depleted within clathrin-coated pits. *Curr Biol.* Apr 15 2003;13(8):686-690.
79. Vercauteren D, Piest M, van der Aa LJ, et al. Flotillin-dependent endocytosis and a phagocytosis-like mechanism for cellular internalization of disulfide-based poly(amido amine)/DNA polyplexes. *Biomaterials.* Apr 2011;32(11):3072-3084.
80. McMahon HT, Boucrot E. Molecular mechanism and physiological functions of clathrin-mediated endocytosis. *Nat Rev Mol Cell Biol.* Aug 2011;12(8):517-533.
81. Zuhorn IS, Kalicharan R, Hoekstra D. Lipoplex-mediated transfection of mammalian cells occurs through the cholesterol-dependent clathrin-mediated pathway of endocytosis. *J Biol Chem.* May 17 2002;277(20):18021-18028.
82. Barysch SV, Aggarwal S, Jahn R, Rizzoli SO. Sorting in early endosomes reveals connections to docking- and fusion-associated factors. *Proc Natl Acad Sci U S A.* Jun 16 2009;106(24):9697-9702.
83. Lu JJ, Langer R, Chen J. A novel mechanism is involved in cationic lipid-mediated functional siRNA delivery. *Mol Pharm.* May-Jun 2009;6(3):763-771.

84. Huth S, Lausier J, Gersting SW, et al. Insights into the mechanism of magnetofection using PEI-based magnetofectins for gene transfer. *J Gene Med.* Aug 2004;6(8):923-936.
85. Arsianti M, Lim M, Marquis CP, Amal R. Polyethylenimine based magnetic iron-oxide vector: the effect of vector component assembly on cellular entry mechanism, intracellular localization, and cellular viability. *Biomacromolecules.* Sep 13 2010;11(9):2521-2531.
86. Petters C, Dringen R. Accumulation of iron oxide nanoparticles by cultured primary neurons. *Neurochem Int.* Feb 2015;81:1-9.
87. El-Sayed A, Harashima H. Endocytosis of gene delivery vectors: from clathrin-dependent to lipid raft-mediated endocytosis. *Mol Ther.* Jun 2013;21(6):1118-1130.
88. Staubach S, Hanisch FG. Lipid rafts: signaling and sorting platforms of cells and their roles in cancer. *Expert Rev Proteomics.* Apr 2011;8(2):263-277.
89. Murata M, Peranen J, Schreiner R, Wieland F, Kurzchalia TV, Simons K. VIP21/caveolin is a cholesterol-binding protein. *Proc Natl Acad Sci U S A.* Oct 24 1995;92(22):10339-10343.
90. Wang Z, Tiruppathi C, Minshall RD, Malik AB. Size and dynamics of caveolae studied using nanoparticles in living endothelial cells. *ACS Nano.* Dec 22 2009;3(12):4110-4116.
91. Smart EJ, Graf GA, McNiven MA, et al. Caveolins, liquid-ordered domains, and signal transduction. *Mol Cell Biol.* Nov 1999;19(11):7289-7304.
92. Simionescu M, Popov D, Sima A. Endothelial transcytosis in health and disease. *Cell Tissue Res.* Jan 2009;335(1):27-40.
93. Duchardt F, Fotin-Mleczek M, Schwarz H, Fischer R, Brock R. A comprehensive model for the cellular uptake of cationic cell-penetrating peptides. *Traffic.* Jul 2007;8(7):848-866.
94. Kunzmann A, Andersson B, Thurnherr T, Krug H, Scheynius A, Fadeel B. Toxicology of engineered nanomaterials: focus on biocompatibility, biodistribution and biodegradation. *Biochim Biophys Acta.* Mar 2011;1810(3):361-373.
95. Adjei IM, Sharma B, Labhasetwar V. Nanoparticles: cellular uptake and cytotoxicity. *Adv Exp Med Biol.* 2014;811:73-91.
96. Hsu SH, Ho TT, Tseng TC. Nanoparticle uptake and gene transfer efficiency for MSCs on chitosan and chitosan-hyaluronan substrates. *Biomaterials.* May 2012;33(14):3639-3650.
97. Kerr MC, Teasdale RD. Defining macropinocytosis. *Traffic.* Apr 2009;10(4):364-371.
98. Panariti A, Lettiero B, Alexandrescu R, et al. Dynamic investigation of interaction of biocompatible iron oxide nanoparticles with epithelial cells for biomedical applications. *J Biomed Nanotechnol.* Sep 2013;9(9):1556-1569.
99. Hofmann D, Tenzer S, Bannwarth MB, et al. Mass spectrometry and imaging analysis of nanoparticle-containing vesicles provide a mechanistic insight into cellular trafficking. *ACS Nano.* Oct 28 2014;8(10):10077-10088.
100. Radhakrishna H, Donaldson JG. ADP-ribosylation factor 6 regulates a novel plasma membrane recycling pathway. *J Cell Biol.* Oct 6 1997;139(1):49-61.
101. Kang YS, Zhao X, Lovaas J, Eisenberg E, Greene LE. Clathrin-independent internalization of normal cellular prion protein in neuroblastoma cells is associated with the Arf6 pathway. *J Cell Sci.* Nov 15 2009;122(Pt 22):4062-4069.

102. Paterson AD, Parton RG, Ferguson C, Stow JL, Yap AS. Characterization of E-cadherin endocytosis in isolated MCF-7 and chinese hamster ovary cells: the initial fate of unbound E-cadherin. *J Biol Chem.* Jun 6 2003;278(23):21050-21057.
103. Brown FD, Rozelle AL, Yin HL, Balla T, Donaldson JG. Phosphatidylinositol 4,5-bisphosphate and Arf6-regulated membrane traffic. *J Cell Biol.* Sep 3 2001;154(5):1007-1017.
104. Chadda R, Howes MT, Plowman SJ, Hancock JF, Parton RG, Mayor S. Cholesterol-sensitive Cdc42 activation regulates actin polymerization for endocytosis via the GEEC pathway. *Traffic.* Jun 2007;8(6):702-717.
105. Sabharanjak S, Sharma P, Parton RG, Mayor S. GPI-anchored proteins are delivered to recycling endosomes via a distinct cdc42-regulated, clathrin-independent pinocytic pathway. *Dev Cell.* Apr 2002;2(4):411-423.
106. Pelish HE, Peterson JR, Salvarezza SB, et al. Secramine inhibits Cdc42-dependent functions in cells and Cdc42 activation in vitro. *Nat Chem Biol.* Jan 2006;2(1):39-46.
107. Lamaze C, Dujeancourt A, Baba T, Lo CG, Benmerah A, Dautry-Varsat A. Interleukin 2 receptors and detergent-resistant membrane domains define a clathrin-independent endocytic pathway. *Mol Cell.* Mar 2001;7(3):661-671.
108. Cheng ZJ, Singh RD, Sharma DK, et al. Distinct mechanisms of clathrin-independent endocytosis have unique sphingolipid requirements. *Mol Biol Cell.* Jul 2006;17(7):3197-3210.
109. Underhill DM, Goodridge HS. Information processing during phagocytosis. *Nat Rev Immunol.* Jul 2012;12(7):492-502.
110. Flannagan RS, Jaumouille V, Grinstein S. The cell biology of phagocytosis. *Annu Rev Pathol.* 2012;7:61-98.
111. Raynal I, Prigent P, Peyramaure S, Najid A, Rebuzzi C, Corot C. Macrophage endocytosis of superparamagnetic iron oxide nanoparticles: mechanisms and comparison of ferumoxides and ferumoxtran-10. *Invest Radiol.* Jan 2004;39(1):56-63.
112. Ribatti D, Nico B, Crivellato E, Artico M. Development of the blood-brain barrier: a historical point of view. *Anat Rec B New Anat.* Jan 2006;289(1):3-8.
113. Ueno M. Molecular anatomy of the brain endothelial barrier: an overview of the distributional features. *Curr Med Chem.* 2007;14(11):1199-1206.
114. Liddelow SA. Development of the choroid plexus and blood-CSF barrier. *Front Neurosci.* 2015;9:32.
115. Spector R, Keep RF, Robert Snodgrass S, Smith QR, Johanson CE. A balanced view of choroid plexus structure and function: Focus on adult humans. *Exp Neurol.* May 2015;267:78-86.
116. van Deurs B, Koehler JK. Tight junctions in the choroid plexus epithelium. A freeze-fracture study including complementary replicas. *J Cell Biol.* Mar 1979;80(3):662-673.
117. Strazielle N, Ghersi-Egea JF. Physiology of blood-brain interfaces in relation to brain disposition of small compounds and macromolecules. *Mol Pharm.* May 6 2013;10(5):1473-1491.
118. Neuwelt EA, Bauer B, Fahlke C, et al. Engaging neuroscience to advance translational research in brain barrier biology. *Nat Rev Neurosci.* Mar 2011;12(3):169-182.
119. Spector R. Nutrient transport systems in brain: 40 years of progress. *J Neurochem.* Oct 2009;111(2):315-320.

120. Thomas SA, Preston JE, Wilson MR, Farrell CL, Segal MB. Leptin transport at the blood--cerebrospinal fluid barrier using the perfused sheep choroid plexus model. *Brain Res.* Mar 23 2001;895(1-2):283-290.
121. Cornford EM, Varesi JB, Hyman S, Damian RT, Raleigh MJ. Mitochondrial content of choroid plexus epithelium. *Exp Brain Res.* Oct 1997;116(3):399-405.
122. Hawkins BT, Davis TP. The blood-brain barrier/neurovascular unit in health and disease. *Pharmacol Rev.* Jun 2005;57(2):173-185.
123. Igarashi Y, Utsumi H, Chiba H, et al. Glial cell line-derived neurotrophic factor induces barrier function of endothelial cells forming the blood-brain barrier. *Biochem Biophys Res Commun.* Jul 22 1999;261(1):108-112.
124. Stewart PA, Wiley MJ. Developing nervous tissue induces formation of blood-brain barrier characteristics in invading endothelial cells: a study using quail--chick transplantation chimeras. *Dev Biol.* May 1981;84(1):183-192.
125. Stanness KA, Westrum LE, Fornaciari E, et al. Morphological and functional characterization of an in vitro blood-brain barrier model. *Brain Res.* Oct 17 1997;771(2):329-342.
126. Hayashi Y, Nomura M, Yamagishi S, Harada S, Yamashita J, Yamamoto H. Induction of various blood-brain barrier properties in non-neural endothelial cells by close apposition to co-cultured astrocytes. *Glia.* Jan 1997;19(1):13-26.
127. Shepro D, Morel NM. Pericyte physiology. *FASEB J.* Aug 1993;7(11):1031-1038.
128. Kutcher ME, Herman IM. The pericyte: cellular regulator of microvascular blood flow. *Microvasc Res.* May 2009;77(3):235-246.
129. Armulik A, Genove G, Mae M, et al. Pericytes regulate the blood-brain barrier. *Nature.* Nov 25 2010;468(7323):557-561.
130. Neuwelt E, Abbott NJ, Abrey L, et al. Strategies to advance translational research into brain barriers. *Lancet Neurol.* Jan 2008;7(1):84-96.
131. Tajes M, Ramos-Fernandez E, Weng-Jiang X, et al. The blood-brain barrier: structure, function and therapeutic approaches to cross it. *Mol Membr Biol.* Aug 2014;31(5):152-167.
132. Reese TS, Karnovsky MJ. Fine structural localization of a blood-brain barrier to exogenous peroxidase. *J Cell Biol.* Jul 1967;34(1):207-217.
133. Lu CT, Zhao YZ, Wong HL, Cai J, Peng L, Tian XQ. Current approaches to enhance CNS delivery of drugs across the brain barriers. *Int J Nanomedicine.* 2014;9:2241-2257.
134. Crone C, Christensen O. Electrical resistance of a capillary endothelium. *J Gen Physiol.* Apr 1981;77(4):349-371.
135. Nusrat A, Brown GT, Tom J, et al. Multiple protein interactions involving proposed extracellular loop domains of the tight junction protein occludin. *Mol Biol Cell.* Apr 2005;16(4):1725-1734.
136. Rubin LL, Staddon JM. The cell biology of the blood-brain barrier. *Annu Rev Neurosci.* 1999;22:11-28.
137. Lampugnani MG, Corada M, Caveda L, et al. The molecular organization of endothelial cell to cell junctions: differential association of plakoglobin, beta-catenin, and alpha-catenin with vascular endothelial cadherin (VE-cadherin). *J Cell Biol.* Apr 1995;129(1):203-217.
138. Matter K, Balda MS. Holey barrier: claudins and the regulation of brain endothelial permeability. *J Cell Biol.* May 12 2003;161(3):459-460.

139. Wolburg H, Lippoldt A. Tight junctions of the blood-brain barrier: development, composition and regulation. *Vascul Pharmacol.* Jun 2002;38(6):323-337.
140. Inai T, Kobayashi J, Shibata Y. Claudin-1 contributes to the epithelial barrier function in MDCK cells. *Eur J Cell Biol.* Dec 1999;78(12):849-855.
141. Haseloff RF, Dithmer S, Winkler L, Wolburg H, Blasig IE. Transmembrane proteins of the tight junctions at the blood-brain barrier: structural and functional aspects. *Semin Cell Dev Biol.* Feb 2015;38:16-25.
142. Daneman R, Zhou L, Agalliu D, Cahoy JD, Kaushal A, Barres BA. The mouse blood-brain barrier transcriptome: a new resource for understanding the development and function of brain endothelial cells. *PLoS One.* 2010;5(10):e13741.
143. Ohtsuki S, Yamaguchi H, Katsukura Y, Asashima T, Terasaki T. mRNA expression levels of tight junction protein genes in mouse brain capillary endothelial cells highly purified by magnetic cell sorting. *J Neurochem.* Jan 2008;104(1):147-154.
144. Ohtsuki S, Sato S, Yamaguchi H, Kamoi M, Asashima T, Terasaki T. Exogenous expression of claudin-5 induces barrier properties in cultured rat brain capillary endothelial cells. *J Cell Physiol.* Jan 2007;210(1):81-86.
145. Nitta T, Hata M, Gotoh S, et al. Size-selective loosening of the blood-brain barrier in claudin-5-deficient mice. *J Cell Biol.* May 12 2003;161(3):653-660.
146. Lamagna C, Meda P, Mandicourt G, et al. Dual interaction of JAM-C with JAM-B and alpha(M)beta2 integrin: function in junctional complexes and leukocyte adhesion. *Mol Biol Cell.* Oct 2005;16(10):4992-5003.
147. Ebnet K, Suzuki A, Ohno S, Vestweber D. Junctional adhesion molecules (JAMs): more molecules with dual functions? *J Cell Sci.* Jan 1 2004;117(Pt 1):19-29.
148. Palmeri D, van Zante A, Huang CC, Hemmerich S, Rosen SD. Vascular endothelial junction-associated molecule, a novel member of the immunoglobulin superfamily, is localized to intercellular boundaries of endothelial cells. *J Biol Chem.* Jun 23 2000;275(25):19139-19145.
149. Petty MA, Lo EH. Junctional complexes of the blood-brain barrier: permeability changes in neuroinflammation. *Prog Neurobiol.* Dec 2002;68(5):311-323.
150. Taddei A, Giampietro C, Conti A, et al. Endothelial adherens junctions control tight junctions by VE-cadherin-mediated upregulation of claudin-5. *Nat Cell Biol.* Aug 2008;10(8):923-934.
151. Graesser D, Solowiej A, Bruckner M, et al. Altered vascular permeability and early onset of experimental autoimmune encephalomyelitis in PECAM-1-deficient mice. *J Clin Invest.* Feb 2002;109(3):383-392.
152. On NH, Miller DW. Transporter-based delivery of anticancer drugs to the brain: improving brain penetration by minimizing drug efflux at the blood-brain barrier. *Curr Pharm Des.* 2014;20(10):1499-1509.
153. Miller DS, Bauer B, Hartz AM. Modulation of P-glycoprotein at the blood-brain barrier: opportunities to improve central nervous system pharmacotherapy. *Pharmacol Rev.* Jun 2008;60(2):196-209.
154. Pahnke J, Wolkenhauer O, Krohn M, Walker LC. Clinico-pathologic function of cerebral ABC transporters - implications for the pathogenesis of Alzheimer's disease. *Curr Alzheimer Res.* Aug 2008;5(4):396-405.
155. Seelig A, Landwojtowicz E. Structure-activity relationship of P-glycoprotein substrates and modifiers. *Eur J Pharm Sci.* Nov 2000;12(1):31-40.

156. Kania KD, Wijesuriya HC, Hladky SB, Barrand MA. Beta amyloid effects on expression of multidrug efflux transporters in brain endothelial cells. *Brain Res.* Oct 18 2011;1418:1-11.
157. Wijesuriya HC, Bullock JY, Faull RL, Hladky SB, Barrand MA. ABC efflux transporters in brain vasculature of Alzheimer's subjects. *Brain Res.* Oct 28 2010;1358:228-238.
158. Cole SP, Bhardwaj G, Gerlach JH, et al. Overexpression of a transporter gene in a multidrug-resistant human lung cancer cell line. *Science.* Dec 4 1992;258(5088):1650-1654.
159. Keppler D. Multidrug resistance proteins (MRPs, ABCCs): importance for pathophysiology and drug therapy. *Handb Exp Pharmacol.* 2011(201):299-323.
160. Zhang Y, Schuetz JD, Elmquist WF, Miller DW. Plasma membrane localization of multidrug resistance-associated protein homologs in brain capillary endothelial cells. *J Pharmacol Exp Ther.* Nov 2004;311(2):449-455.
161. de Lange EC. Potential role of ABC transporters as a detoxification system at the blood-CSF barrier. *Adv Drug Deliv Rev.* Oct 14 2004;56(12):1793-1809.
162. Nicolazzo JA, Katneni K. Drug transport across the blood-brain barrier and the impact of breast cancer resistance protein (ABCG2). *Curr Top Med Chem.* 2009;9(2):130-147.
163. Imai Y, Asada S, Tsukahara S, Ishikawa E, Tsuruo T, Sugimoto Y. Breast cancer resistance protein exports sulfated estrogens but not free estrogens. *Mol Pharmacol.* Sep 2003;64(3):610-618.
164. Suzuki M, Suzuki H, Sugimoto Y, Sugiyama Y. ABCG2 transports sulfated conjugates of steroids and xenobiotics. *J Biol Chem.* Jun 20 2003;278(25):22644-22649.
165. Ueno M, Nakagawa T, Wu B, et al. Transporters in the brain endothelial barrier. *Curr Med Chem.* 2010;17(12):1125-1138.
166. Sagare AP, Deane R, Zlokovic BV. Low-density lipoprotein receptor-related protein 1: a physiological Abeta homeostatic mechanism with multiple therapeutic opportunities. *Pharmacol Ther.* Oct 2012;136(1):94-105.
167. Demeule M, Currie JC, Bertrand Y, et al. Involvement of the low-density lipoprotein receptor-related protein in the transcytosis of the brain delivery vector angiopep-2. *J Neurochem.* Aug 2008;106(4):1534-1544.
168. Bertrand Y, Currie JC, Poirier J, et al. Influence of glioma tumour microenvironment on the transport of ANG1005 via low-density lipoprotein receptor-related protein 1. *Br J Cancer.* Nov 22 2011;105(11):1697-1707.
169. Huang S, Li J, Han L, et al. Dual targeting effect of Angiopep-2-modified, DNA-loaded nanoparticles for glioma. *Biomaterials.* Oct 2011;32(28):6832-6838.
170. Xin H, Sha X, Jiang X, Zhang W, Chen L, Fang X. Anti-glioblastoma efficacy and safety of paclitaxel-loading Angiopep-conjugated dual targeting PEG-PCL nanoparticles. *Biomaterials.* Nov 2012;33(32):8167-8176.
171. Drappatz J, Brenner A, Wong ET, et al. Phase I study of GRN1005 in recurrent malignant glioma. *Clin Cancer Res.* Mar 15 2013;19(6):1567-1576.
172. Che C, Yang G, Thiot C, et al. New Angiopep-modified doxorubicin (ANG1007) and etoposide (ANG1009) chemotherapeutics with increased brain penetration. *J Med Chem.* Apr 8 2010;53(7):2814-2824.
173. Koffie RM, Farrar CT, Saidi LJ, William CM, Hyman BT, Spires-Jones TL. Nanoparticles enhance brain delivery of blood-brain barrier-impermeable probes for in

vivo optical and magnetic resonance imaging. *Proc Natl Acad Sci U S A.* Nov 15 2011;108(46):18837-18842.
174. Tanaka N, Sasahara M, Ohno M, Higashiyama S, Hayase Y, Shimada M. Heparin-binding epidermal growth factor-like growth factor mRNA expression in neonatal rat brain with hypoxic/ischemic injury. *Brain Res.* May 8 1999;827(1-2):130-138.
175. Mishima K, Higashiyama S, Asai A, et al. Heparin-binding epidermal growth factor-like growth factor stimulates mitogenic signaling and is highly expressed in human malignant gliomas. *Acta Neuropathol.* Oct 1998;96(4):322-328.
176. Kuo YC, Chung CY. Transcytosis of CRM197-grafted polybutylcyanoacrylate nanoparticles for delivering zidovudine across human brain-microvascular endothelial cells. *Colloids Surf B Biointerfaces.* Mar 1 2012;91:242-249.
177. Wang P, Liu Y, Shang X, Xue Y. CRM197-induced blood-brain barrier permeability increase is mediated by upregulation of caveolin-1 protein. *J Mol Neurosci.* Mar 2011;43(3):485-492.
178. Zhang P, Hu L, Yin Q, Zhang Z, Feng L, Li Y. Transferrin-conjugated polyphosphoester hybrid micelle loading paclitaxel for brain-targeting delivery: synthesis, preparation and in vivo evaluation. *J Control Release.* May 10 2012;159(3):429-434.
179. Boado RJ, Hui EK, Lu JZ, Pardridge WM. Drug targeting of erythropoietin across the primate blood-brain barrier with an IgG molecular Trojan horse. *J Pharmacol Exp Ther.* Jun 2010;333(3):961-969.
180. Ke W, Shao K, Huang R, et al. Gene delivery targeted to the brain using an Angiopep-conjugated polyethyleneglycol-modified polyamidoamine dendrimer. *Biomaterials.* Dec 2009;30(36):6976-6985.
181. van Rooy I, Mastrobattista E, Storm G, Hennink WE, Schiffelers RM. Comparison of five different targeting ligands to enhance accumulation of liposomes into the brain. *J Control Release.* Feb 28 2011;150(1):30-36.
182. van der Meel R, Vehmeijer LJ, Kok RJ, Storm G, van Gaal EV. Ligand-targeted particulate nanomedicines undergoing clinical evaluation: current status. *Adv Drug Deliv Rev.* Oct 2013;65(10):1284-1298.
183. Pardridge WM. The blood-brain barrier: bottleneck in brain drug development. *NeuroRx.* Jan 2005;2(1):3-14.
184. Dohgu S, Yamauchi A, Takata F, et al. Transforming growth factor-beta1 upregulates the tight junction and P-glycoprotein of brain microvascular endothelial cells. *Cell Mol Neurobiol.* Jun 2004;24(3):491-497.
185. Patnaik R, Mohanty S, Sharma HS. Blockade of histamine H2 receptors attenuate blood-brain barrier permeability, cerebral blood flow disturbances, edema formation and cell reactions following hyperthermic brain injury in the rat. *Acta Neurochir Suppl.* 2000;76:535-539.
186. Abbott NJ. Inflammatory mediators and modulation of blood-brain barrier permeability. *Cell Mol Neurobiol.* Apr 2000;20(2):131-147.
187. Argaw AT, Zhang Y, Snyder BJ, et al. IL-1beta regulates blood-brain barrier permeability via reactivation of the hypoxia-angiogenesis program. *J Immunol.* Oct 15 2006;177(8):5574-5584.
188. Stamatovic SM, Shakui P, Keep RF, et al. Monocyte chemoattractant protein-1 regulation of blood-brain barrier permeability. *J Cereb Blood Flow Metab.* May 2005;25(5):593-606.

189. Reuss B, Dono R, Unsicker K. Functions of fibroblast growth factor (FGF)-2 and FGF-5 in astroglial differentiation and blood-brain barrier permeability: evidence from mouse mutants. *J Neurosci.* Jul 23 2003;23(16):6404-6412.
190. Dimitrijevic OB, Stamatovic SM, Keep RF, Andjelkovic AV. Effects of the chemokine CCL2 on blood-brain barrier permeability during ischemia-reperfusion injury. *J Cereb Blood Flow Metab.* Jun 2006;26(6):797-810.
191. Zhang ZG, Zhang L, Jiang Q, et al. VEGF enhances angiogenesis and promotes blood-brain barrier leakage in the ischemic brain. *J Clin Invest.* Oct 2000;106(7):829-838.
192. On NH, Savant S, Toews M, Miller DW. Rapid and reversible enhancement of blood-brain barrier permeability using lysophosphatidic acid. *J Cereb Blood Flow Metab.* Dec 2013;33(12):1944-1954.
193. Rapoport SI. Advances in osmotic opening of the blood-brain barrier to enhance CNS chemotherapy. *Expert Opin Investig Drugs.* Oct 2001;10(10):1809-1818.
194. Rapoport SI. Effect of concentrated solutions on blood-brain barrier. *Am J Physiol.* Jul 1970;219(1):270-274.
195. Boockvar JA, Tsiouris AJ, Hofstetter CP, et al. Safety and maximum tolerated dose of superselective intraarterial cerebral infusion of bevacizumab after osmotic blood-brain barrier disruption for recurrent malignant glioma. Clinical article. *J Neurosurg.* Mar 2011;114(3):624-632.
196. Angelov L, Doolittle ND, Kraemer DF, et al. Blood-brain barrier disruption and intra-arterial methotrexate-based therapy for newly diagnosed primary CNS lymphoma: a multi-institutional experience. *J Clin Oncol.* Jul 20 2009;27(21):3503-3509.
197. Jahnke K, Kraemer DF, Knight KR, et al. Intraarterial chemotherapy and osmotic blood-brain barrier disruption for patients with embryonal and germ cell tumors of the central nervous system. *Cancer.* Feb 1 2008;112(3):581-588.
198. Hall WA, Doolittle ND, Daman M, et al. Osmotic blood-brain barrier disruption chemotherapy for diffuse pontine gliomas. *J Neurooncol.* May 2006;77(3):279-284.
199. Rapoport SI, Fredericks WR, Ohno K, Pettigrew KD. Quantitative aspects of reversible osmotic opening of the blood-brain barrier. *Am J Physiol.* May 1980;238(5):R421-431.
200. Bellavance MA, Blanchette M, Fortin D. Recent advances in blood-brain barrier disruption as a CNS delivery strategy. *AAPS J.* 2008;10(1):166-177.
201. Elliott PJ, Hayward NJ, Dean RL, Blunt DG, Bartus RT. Intravenous RMP-7 selectively increases uptake of carboplatin into rat brain tumors. *Cancer Res.* Sep 1 1996;56(17):3998-4005.
202. Inamura T, Nomura T, Bartus RT, Black KL. Intracarotid infusion of RMP-7, a bradykinin analog: a method for selective drug delivery to brain tumors. *J Neurosurg.* Nov 1994;81(5):752-758.
203. Prados MD, Schold SJS, Fine HA, et al. A randomized, double-blind, placebo-controlled, phase 2 study of RMP-7 in combination with carboplatin administered intravenously for the treatment of recurrent malignant glioma. *Neuro Oncol.* Apr 2003;5(2):96-103.
204. Bartus RT, Snodgrass P, Marsh J, Agostino M, Perkins A, Emerich DF. Intravenous cereport (RMP-7) modifies topographic uptake profile of carboplatin within rat glioma and brain surrounding tumor, elevates platinum levels, and enhances survival. *J Pharmacol Exp Ther.* Jun 2000;293(3):903-911.
205. Choi JW, Herr DR, Noguchi K, et al. LPA receptors: subtypes and biological actions. *Annu Rev Pharmacol Toxicol.* 2010;50:157-186.

206. Zhao Y, Natarajan V. Lysophosphatidic acid signaling in airway epithelium: role in airway inflammation and remodeling. *Cell Signal.* Mar 2009;21(3):367-377.
207. Aryal M, Arvanitis CD, Alexander PM, McDannold N. Ultrasound-mediated blood-brain barrier disruption for targeted drug delivery in the central nervous system. *Adv Drug Deliv Rev.* Jun 2014;72:94-109.
208. Sheikov N, McDannold N, Vykhodtseva N, Jolesz F, Hynynen K. Cellular mechanisms of the blood-brain barrier opening induced by ultrasound in presence of microbubbles. *Ultrasound Med Biol.* Jul 2004;30(7):979-989.
209. Hynynen K, McDannold N, Vykhodtseva N, Jolesz FA. Noninvasive MR imaging-guided focal opening of the blood-brain barrier in rabbits. *Radiology.* Sep 2001;220(3):640-646.
210. Park J, Zhang Y, Vykhodtseva N, Jolesz FA, McDannold NJ. The kinetics of blood brain barrier permeability and targeted doxorubicin delivery into brain induced by focused ultrasound. *J Control Release.* Aug 20 2012;162(1):134-142.
211. Hynynen K, McDannold N, Sheikov NA, Jolesz FA, Vykhodtseva N. Local and reversible blood-brain barrier disruption by noninvasive focused ultrasound at frequencies suitable for trans-skull sonications. *Neuroimage.* Jan 1 2005;24(1):12-20.
212. Liu HL, Hua MY, Yang HW, et al. Magnetic resonance monitoring of focused ultrasound/magnetic nanoparticle targeting delivery of therapeutic agents to the brain. *Proc Natl Acad Sci U S A.* Aug 24 2010;107(34):15205-15210.
213. Nance E, Timbie K, Miller GW, et al. Non-invasive delivery of stealth, brain-penetrating nanoparticles across the blood-brain barrier using MRI-guided focused ultrasound. *J Control Release.* Sep 10 2014;189:123-132.
214. Yao L, Song Q, Bai W, et al. Facilitated brain delivery of poly (ethylene glycol)-poly (lactic acid) nanoparticles by microbubble-enhanced unfocused ultrasound. *Biomaterials.* Mar 2014;35(10):3384-3395.
215. Etame AB, Diaz RJ, O'Reilly MA, et al. Enhanced delivery of gold nanoparticles with therapeutic potential into the brain using MRI-guided focused ultrasound. *Nanomedicine.* Oct 2012;8(7):1133-1142.
216. Wang PH, Liu HL, Hsu PH, et al. Gold-nanorod contrast-enhanced photoacoustic micro-imaging of focused-ultrasound induced blood-brain-barrier opening in a rat model. *J Biomed Opt.* Jun 2012;17(6):061222.
217. Diaz RJ, McVeigh PZ, O'Reilly MA, et al. Focused ultrasound delivery of Raman nanoparticles across the blood-brain barrier: potential for targeting experimental brain tumors. *Nanomedicine.* Jul 2014;10(5):1075-1087.
218. Fan CH, Ting CY, Lin HJ, et al. SPIO-conjugated, doxorubicin-loaded microbubbles for concurrent MRI and focused-ultrasound enhanced brain-tumor drug delivery. *Biomaterials.* May 2013;34(14):3706-3715.
219. Moraes L, Vasconcelos-Dos-Santos A, Santana FC, et al. Neuroprotective effects and magnetic resonance imaging of mesenchymal stem cells labeled with SPION in a rat model of Huntington's disease. *Stem Cell Res.* Sep 2012;9(2):143-155.
220. Maier-Hauff K, Ulrich F, Nestler D, et al. Efficacy and safety of intratumoral thermotherapy using magnetic iron-oxide nanoparticles combined with external beam radiotherapy on patients with recurrent glioblastoma multiforme. *J Neurooncol.* Jun 2011;103(2):317-324.

221. Kenzaoui BH, Bernasconi CC, Hofmann H, Juillerat-Jeanneret L. Evaluation of uptake and transport of ultrasmall superparamagnetic iron oxide nanoparticles by human brain-derived endothelial cells. *Nanomedicine (Lond).* Jan 2012;7(1):39-53.
222. Prohaska R, Sibon OC, Rudnicki DD, et al. Brain, blood, and iron: perspectives on the roles of erythrocytes and iron in neurodegeneration. *Neurobiol Dis.* Jun 2012;46(3):607-624.
223. Zheng W, Monnot AD. Regulation of brain iron and copper homeostasis by brain barrier systems: implication in neurodegenerative diseases. *Pharmacol Ther.* Feb 2012;133(2):177-188.
224. Batista-Nascimento L, Pimentel C, Menezes RA, Rodrigues-Pousada C. Iron and neurodegeneration: from cellular homeostasis to disease. *Oxid Med Cell Longev.* 2012;2012:128647.
225. Kubinova S, Sykova E. Nanotechnology for treatment of stroke and spinal cord injury. *Nanomedicine (Lond).* Jan 2010;5(1):99-108.
226. Stoll G, Bendszus M. Imaging of inflammation in the peripheral and central nervous system by magnetic resonance imaging. *Neuroscience.* Feb 6 2009;158(3):1151-1160.
227. Ma P, Luo Q, Chen J, et al. Intraperitoneal injection of magnetic Fe(3)O(4)-nanoparticle induces hepatic and renal tissue injury via oxidative stress in mice. *Int J Nanomedicine.* 2012;7:4809-4818.
228. Naqvi S, Samim M, Abdin M, et al. Concentration-dependent toxicity of iron oxide nanoparticles mediated by increased oxidative stress. *Int J Nanomedicine.* 2010;5:983-989.
229. Rivet CJ, Yuan Y, Borca-Tasciuc DA, Gilbert RJ. Altering iron oxide nanoparticle surface properties induce cortical neuron cytotoxicity. *Chem Res Toxicol.* Jan 13 2012;25(1):153-161.
230. Bernardi A, Frozza RL, Meneghetti A, et al. Indomethacin-loaded lipid-core nanocapsules reduce the damage triggered by Abeta1-42 in Alzheimer's disease models. *Int J Nanomedicine.* 2012;7:4927-4942.
231. Hong SC, Lee JH, Lee J, et al. Subtle cytotoxicity and genotoxicity differences in superparamagnetic iron oxide nanoparticles coated with various functional groups. *Int J Nanomedicine.* 2011;6:3219-3231.
232. Galeotti F, Bertini F, Scavia G, Bolognesi A. A controlled approach to iron oxide nanoparticles functionalization for magnetic polymer brushes. *J Colloid Interface Sci.* Aug 15 2011;360(2):540-547.
233. Yathindranath V, Rebbouh L, Moore DF, Miller DW, van Lierop J, Hegmann T. A Versatile Method for the Reductive, One-Pot Synthesis of Bare, Hydrophilic and Hydrophobic Magnetite Nanoparticles. *Advanced Functional Materials.* 2011;21(8):1457-1464.
234. Zamzow CR, Xiong W, Parkinson FE. Adenosine produced by neurons is metabolized to hypoxanthine by astrocytes. *J Neurosci Res.* Nov 15 2008;86(15):3447-3455.
235. Luft JH. Improvements in epoxy resin embedding methods. *J Biophys Biochem Cytol.* Feb 1961;9:409-414.
236. Wohlfart S, Gelperina S, Kreuter J. Transport of drugs across the blood-brain barrier by nanoparticles. *J Control Release.* Jul 20 2012;161(2):264-273.
237. Celia C, Cosco D, Paolino D, Fresta M. Nanoparticulate devices for brain drug delivery. *Med Res Rev.* Feb 16 2010.

238. Wagner S, Zensi A, Wien SL, et al. Uptake mechanism of ApoE-modified nanoparticles on brain capillary endothelial cells as a blood-brain barrier model. *PLoS ONE.* 2012;7(3):e32568.
239. Wankhede M, Bouras A, Kaluzova M, Hadjipanayis CG. Magnetic nanoparticles: an emerging technology for malignant brain tumor imaging and therapy. *Expert Rev Clin Pharmacol.* Mar 2012;5(2):173-186.
240. Hutter E, Boridy S, Labrecque S, et al. Microglial response to gold nanoparticles. *ACS Nano.* May 25 2010;4(5):2595-2606.
241. Zhao J, Xu L, Zhang T, Ren G, Yang Z. Influences of nanoparticle zinc oxide on acutely isolated rat hippocampal CA3 pyramidal neurons. *Neurotoxicology.* Mar 2009;30(2):220-230.
242. Wang J, Chen C, Liu Y, et al. Potential neurological lesion after nasal instillation of TiO(2) nanoparticles in the anatase and rutile crystal phases. *Toxicol Lett.* Dec 15 2008;183(1-3):72-80.
243. Chertok B, David AE, Yang VC. Polyethyleneimine-modified iron oxide nanoparticles for brain tumor drug delivery using magnetic targeting and intra-carotid administration. *Biomaterials.* Aug 2010;31(24):6317-6324.
244. Boridy S, Takahashi H, Akiyoshi K, Maysinger D. The binding of pullulan modified cholesteryl nanogels to Abeta oligomers and their suppression of cytotoxicity. *Biomaterials.* Oct 2009;30(29):5583-5591.
245. Feeney CJ, Frantseva MV, Carlen PL, et al. Vulnerability of glial cells to hydrogen peroxide in cultured hippocampal slices. *Brain Res.* Mar 10 2008;1198:1-15.
246. Haase A, Rott S, Mantion A, et al. Effects of silver nanoparticles on primary mixed neural cell cultures: uptake, oxidative stress and acute calcium responses. *Toxicol Sci.* Apr 2012;126(2):457-468.
247. Mahmoudi M, Laurent S, Shokrgozar MA, Hosseinkhani M. Toxicity evaluations of superparamagnetic iron oxide nanoparticles: cell "vision" versus physicochemical properties of nanoparticles. *ACS Nano.* Sep 27 2011;5(9):7263-7276.
248. Kang YS, Pardridge WM. Brain delivery of biotin bound to a conjugate of neutral avidin and cationized human albumin. *Pharm Res.* Sep 1994;11(9):1257-1264.
249. Safi M, Courtois J, Seigneuret M, Conjeaud H, Berret JF. The effects of aggregation and protein corona on the cellular internalization of iron oxide nanoparticles. *Biomaterials.* Dec 2011;32(35):9353-9363.
250. Lamkowsky MC, Geppert M, Schmidt MM, Dringen R. Magnetic field-induced acceleration of the accumulation of magnetic iron oxide nanoparticles by cultured brain astrocytes. *J Biomed Mater Res A.* Nov 7 2011.
251. Tresilwised N, Pithayanukul P, Mykhaylyk O, et al. Boosting oncolytic adenovirus potency with magnetic nanoparticles and magnetic force. *Mol Pharm.* Aug 2 2010;7(4):1069-1089.
252. Pardridge WM. Why is the global CNS pharmaceutical market so under-penetrated? *Drug Discov Today.* Jan 1 2002;7(1):5-7.
253. Daneman R. The blood-brain barrier in health and disease. *Ann Neurol.* Nov 2012;72(5):648-672.
254. On NH, Chen F, Hinton M, Miller DW. Assessment of P-glycoprotein activity in the Blood-Brain Barrier (BBB) using Near Infrared Fluorescence (NIRF) imaging techniques. *Pharm Res.* Oct 2011;28(10):2505-2515.

255. Nicolazzo JA, Katneni K. Drug transport across the blood-brain barrier and the impact of breast cancer resistance protein (ABCG2). *Curr Top Med Chem.* 2009;9(2):130-147.
256. Loscher W, Potschka H. Blood-brain barrier active efflux transporters: ATP-binding cassette gene family. *Neurorx.* Jan 2005;2(1):86-98.
257. Pardridge WM. Drug targeting to the brain. *Pharm Res.* Sep 2007;24(9):1733-1744.
258. Tietze R, Lyer S, Durr S, Alexiou C. Nanoparticles for cancer therapy using magnetic forces. *Nanomedicine (Lond).* Mar 2012;7(3):447-457.
259. Zhu L, Wang D, Wei X, et al. Multifunctional pH-sensitive superparamagnetic iron-oxide nanocomposites for targeted drug delivery and MR imaging. *J Control Release.* Feb 26 2013.
260. Lee GY, Qian WP, Wang L, et al. Theranostic nanoparticles with controlled release of gemcitabine for targeted therapy and MRI of pancreatic cancer. *ACS Nano.* Mar 26 2013;7(3):2078-2089.
261. Xu C, Sun S. New forms of superparamagnetic nanoparticles for biomedical applications. *Adv Drug Deliv Rev.* May 2013;65(5):732-743.
262. Lee MJ, Veiseh O, Bhattarai N, et al. Rapid pharmacokinetic and biodistribution studies using cholorotoxin-conjugated iron oxide nanoparticles: a novel non-radioactive method. *PLoS ONE.* 2010;5(3):e9536.
263. Peer D, Karp JM, Hong S, Farokhzad OC, Margalit R, Langer R. Nanocarriers as an emerging platform for cancer therapy. *Nat Nanotechnol.* Dec 2007;2(12):751-760.
264. Alexiou C, Schmid RJ, Jurgons R, et al. Targeting cancer cells: magnetic nanoparticles as drug carriers. *Eur Biophys J.* May 2006;35(5):446-450.
265. On NH, Mitchell R, Savant SD, Bachmeier CJ, Hatch GM, Miller DW. Examination of blood-brain barrier (BBB) integrity in a mouse brain tumor model. *J Neurooncol.* Jan 2013;111(2):133-143.
266. Sun Z, Yathindranath V, Worden M, et al. Characterization of cellular uptake and toxicity of aminosilane-coated iron oxide nanoparticles with different charges in central nervous system relevant cell culture models. *Int J Nanomedicine.* 2013;8:961-970.
267. Yathindranath V, Sun Z, Worden M, et al. One-pot synthesis of iron oxide nanoparticles with functional silane shells: a versatile general precursor for conjugations and biomedical applications. *Langmuir.* Aug 27 2013;29(34):10850-10858.
268. Li G, Simon MJ, Cancel LM, et al. Permeability of endothelial and astrocyte cocultures: in vitro blood-brain barrier models for drug delivery studies. *Ann Biomed Eng.* Aug 2010;38(8):2499-2511.
269. Berne BJ, Pecora R. *Dynamic Light Scattering: With Applications to Chemistry, Biology, and Physics.* Dover Publications; 2000.
270. Wang J, Chen Y, Chen B, et al. Pharmacokinetic parameters and tissue distribution of magnetic Fe(3)O(4) nanoparticles in mice. *Int J Nanomedicine.* 2010;5:861-866.
271. Petri B, Bootz A, Khalansky A, et al. Chemotherapy of brain tumour using doxorubicin bound to surfactant-coated poly(butyl cyanoacrylate) nanoparticles: revisiting the role of surfactants. *J Control Release.* Jan 22 2007;117(1):51-58.
272. Qiao R, Jia Q, Huwel S, et al. Receptor-mediated delivery of magnetic nanoparticles across the blood-brain barrier. *ACS Nano.* Apr 24 2012;6(4):3304-3310.
273. Etame AB, Smith CA, Chan WC, Rutka JT. Design and potential application of PEGylated gold nanoparticles with size-dependent permeation through brain microvasculature. *Nanomed.* Dec 2011;7(6):992-1000.

274. Kiptoo P, Sinaga E, Calcagno AM, et al. Enhancement of drug absorption through the blood-brain barrier and inhibition of intercellular tight junction resealing by E-cadherin peptides. *Mol Pharm.* Feb 7 2011;8(1):239-249.
275. On NH, Savant S, Toews M, Miller DW. Rapid and reversible enhancement of blood-brain barrier permeability using lysophosphatidic acid. *J Cereb Blood Flow Metab.* Sep 18 2013.
276. Borlongan CV, Glover LE, Sanberg PR, Hess DC. Permeating the blood brain barrier and abrogating the inflammation in stroke: implications for stroke therapy. *Curr Pharm Des.* 2012;18(25):3670-3676.
277. Hynynen K. Ultrasound for drug and gene delivery to the brain. *Adv Drug Deliv Rev.* Jun 30 2008;60(10):1209-1217.
278. Muldoon LL, Nilaver G, Kroll RA, et al. Comparison of intracerebral inoculation and osmotic blood-brain barrier disruption for delivery of adenovirus, herpesvirus, and iron oxide particles to normal rat brain. *Am J Pathol.* Dec 1995;147(6):1840-1851.
279. Burgess A, Hynynen K. Noninvasive and targeted drug delivery to the brain using focused ultrasound. *ACS Chem Neurosci.* Apr 17 2013;4(4):519-526.
280. Carenza E, Barcelo V, Morancho A, et al. In vitro angiogenic performance and in vivo brain targeting of magnetized endothelial progenitor cells for neurorepair therapies. *Nanomedicine.* Jan 2014;10(1):225-234.
281. Kong SD, Lee J, Ramachandran S, et al. Magnetic targeting of nanoparticles across the intact blood-brain barrier. *J Control Release.* Nov 28 2012;164(1):49-57.
282. Chertok B, David AE, Yang VC. Brain tumor targeting of magnetic nanoparticles for potential drug delivery: effect of administration route and magnetic field topography. *J Control Release.* Nov 7 2011;155(3):393-399.
283. Chertok B, Moffat BA, David AE, et al. Iron oxide nanoparticles as a drug delivery vehicle for MRI monitored magnetic targeting of brain tumors. *Biomaterials.* Feb 2008;29(4):487-496.
284. Zhang J, Shin MC, Yang VC. Magnetic Targeting of Novel Heparinized Iron Oxide Nanoparticles Evaluated in a 9L-glioma Mouse Model. *Pharm Res.* Mar 2014;31(3):579-592.
285. Delgado AV, González-Caballero F, Hunter RJ, Koopal LK, Lyklema J. Measurement and interpretation of electrokinetic phenomena. *J Colloid Interface Sci.* 2007;309(2):194-224.
286. Lesniak A, Salvati A, Santos-Martinez MJ, Radomski MW, Dawson KA, Aberg C. Nanoparticle adhesion to the cell membrane and its effect on nanoparticle uptake efficiency. *J Am Chem Soc.* Jan 30 2013;135(4):1438-1444.
287. Jedlovszky-Hajdu A, Bombelli FB, Monopoli MP, Tombacz E, Dawson KA. Surface coatings shape the protein corona of SPIONs with relevance to their application in vivo. *Langmuir.* Oct 23 2012;28(42):14983-14991.
288. Ruh H, Kuhl B, Brenner-Weiss G, Hopf C, Diabate S, Weiss C. Identification of serum proteins bound to industrial nanomaterials. *Toxicol Lett.* Jan 5 2012;208(1):41-50.
289. Yemisci M, Gursoy-Ozdemir Y, Caban S, Bodur E, Capan Y, Dalkara T. Transport of a caspase inhibitor across the blood-brain barrier by chitosan nanoparticles. *Methods Enzymol.* 2012;508:253-269.

290. Lu W, Wan J, She Z, Jiang X. Brain delivery property and accelerated blood clearance of cationic albumin conjugated pegylated nanoparticle. *J Control Release.* Mar 12 2007;118(1):38-53.
291. McNeeley KM, Karathanasis E, Annapragada AV, Bellamkonda RV. Masking and triggered unmasking of targeting ligands on nanocarriers to improve drug delivery to brain tumors. *Biomaterials.* Aug 2009;30(23-24):3986-3995.
292. Chen W, Zhan C, Gu B, et al. Targeted brain delivery of itraconazole via RVG29 anchored nanoparticles. *J Drug Target.* Apr 2011;19(3):228-234.
293. Xie Y, Ye L, Zhang X, et al. Transport of nerve growth factor encapsulated into liposomes across the blood-brain barrier: in vitro and in vivo studies. *J Control Release.* Jun 20 2005;105(1-2):106-119.
294. Georgieva JV, Kalicharan D, Couraud PO, et al. Surface characteristics of nanoparticles determine their intracellular fate in and processing by human blood-brain barrier endothelial cells in vitro. *Mol Ther.* Feb 2011;19(2):318-325.
295. Wegscheid ML, Morshed RA, Cheng Y, Lesniak MS. The art of attraction: applications of multifunctional magnetic nanomaterials for malignant glioma. *Expert Opin Drug Deliv.* Jun 2014;11(6):957-975.
296. Costantino L, Boraschi D, Eaton M. Challenges in the design of clinically useful brain-targeted drug nanocarriers. *Curr Med Chem.* 2014;21(37):4227-4246.
297. Xin H, Sha X, Jiang X, et al. The brain targeting mechanism of Angiopep-conjugated poly(ethylene glycol)-co-poly(epsilon-caprolactone) nanoparticles. *Biomaterials.* Feb 2012;33(5):1673-1681.
298. Sun Z, Worden M, Wroczynskyj Y, et al. Magnetic field enhanced convective diffusion of iron oxide nanoparticles in an osmotically disrupted cell culture model of the blood-brain barrier. *Int J Nanomedicine.* 2014;9:3013-3026.
299. Tomsig JL, Snyder AH, Berdyshev EV, et al. Lipid phosphate phosphohydrolase type 1 (LPP1) degrades extracellular lysophosphatidic acid in vivo. *Biochem J.* May 1 2009;419(3):611-618.
300. Triguero D, Buciak J, Pardridge WM. Capillary depletion method for quantification of blood-brain barrier transport of circulating peptides and plasma proteins. *J Neurochem.* Jun 1990;54(6):1882-1888.
301. Sun Z, Yathindranath V, Worden M, et al. Characterization of cellular uptake and toxicity of aminosilane-coated iron oxide nanoparticles with different charges in central nervous system-relevant cell culture models. *Int J Nanomedicine.* 2013;8:961-970.
302. Li SD, Huang L. Nanoparticles evading the reticuloendothelial system: role of the supported bilayer. *Biochim Biophys Acta.* Oct 2009;1788(10):2259-2266.
303. Doi T, Higashino K, Kurihara Y, et al. Charged collagen structure mediates the recognition of negatively charged macromolecules by macrophage scavenger receptors. *J Biol Chem.* Jan 25 1993;268(3):2126-2133.
304. Chao Y, Makale M, Karmali PP, et al. Recognition of dextran-superparamagnetic iron oxide nanoparticle conjugates (Feridex) via macrophage scavenger receptor charged domains. *Bioconjug Chem.* May 16 2012;23(5):1003-1009.
305. Schleich N, Po C, Jacobs D, et al. Comparison of active, passive and magnetic targeting to tumors of multifunctional paclitaxel/SPIO-loaded nanoparticles for tumor imaging and therapy. *J Control Release.* Nov 28 2014;194:82-91.

306. Tredan O, Galmarini CM, Patel K, Tannock IF. Drug resistance and the solid tumor microenvironment. *J Natl Cancer Inst.* Oct 3 2007;99(19):1441-1454.
307. Kroll RA, Pagel MA, Muldoon LL, Roman-Goldstein S, Fiamengo SA, Neuwelt EA. Improving drug delivery to intracerebral tumor and surrounding brain in a rodent model: a comparison of osmotic versus bradykinin modification of the blood-brain and/or blood-tumor barriers. *Neurosurgery.* Oct 1998;43(4):879-886; discussion 886-879.
308. Rousseau V, Denizot B, Pouliquen D, Jallet P, Le Jeune JJ. Investigation of blood-brain barrier permeability to magnetite-dextran nanoparticles (MD3) after osmotic disruption in rats. *MAGMA.* Sep 1997;5(3):213-222.
309. Remsen LG, McCormick CI, Sexton G, Pearse HD, Garcia R, Neuwelt EA. Decreased delivery and acute toxicity of cranial irradiation and chemotherapy given with osmotic blood-brain barrier disruption in a rodent model: the issue of sequence. *Clin Cancer Res.* Jul 1995;1(7):731-739.
310. Shao K, Huang R, Li J, et al. Angiopep-2 modified PE-PEG based polymeric micelles for amphotericin B delivery targeted to the brain. *J Control Release.* Oct 1 2010;147(1):118-126.
311. Thomas FC, Taskar K, Rudraraju V, et al. Uptake of ANG1005, a novel paclitaxel derivative, through the blood-brain barrier into brain and experimental brain metastases of breast cancer. *Pharm Res.* Nov 2009;26(11):2486-2494.
312. Li XB, Zheng H, Zhang ZR, et al. Glia activation induced by peripheral administration of aluminum oxide nanoparticles in rat brains. *Nanomedicine.* Dec 2009;5(4):473-479.
313. De Astis S, Corradini I, Morini R, et al. Nanostructured TiO2 surfaces promote polarized activation of microglia, but not astrocytes, toward a proinflammatory profile. *Nanoscale.* Nov 21 2013;5(22):10963-10974.
314. Albertazzi L, Gherardini L, Brondi M, et al. In vivo distribution and toxicity of PAMAM dendrimers in the central nervous system depend on their surface chemistry. *Mol Pharm.* Jan 7 2013;10(1):249-260.
315. Cupaioli FA, Zucca FA, Boraschi D, Zecca L. Engineered nanoparticles. How brain friendly is this new guest? *Prog Neurobiol.* Aug-Sep 2014;119-120:20-38.
316. Knowlden S, Georas SN. The autotaxin-LPA axis emerges as a novel regulator of lymphocyte homing and inflammation. *J Immunol.* Feb 1 2014;192(3):851-857.
317. Gustin C, Van Steenbrugge M, Raes M. LPA modulates monocyte migration directly and via LPA-stimulated endothelial cells. *Am J Physiol Cell Physiol.* Oct 2008;295(4):C905-914.
318. Schober A, Siess W. Lysophosphatidic acid in atherosclerotic diseases. *Br J Pharmacol.* Oct 2012;167(3):465-482.
319. Laksitorini MD, Kiptoo PK, On NH, Thliveris JA, Miller DW, Siahaan TJ. Modulation of intercellular junctions by cyclic-ADT peptides as a method to reversibly increase blood-brain barrier permeability. *J Pharm Sci.* Mar 2015;104(3):1065-1075.
320. Worden M, Bruckman MA, Kim M-H, et al. Aqueous synthesis of polyhedral "brick-like" iron oxide nanoparticles for hyperthermia and T2 MRI contrast enhancement. *Journal of Materials Chemistry B.* 2015;3(34):6877-6884.
321. Silva AK, Luciani N, Gazeau F, et al. Combining magnetic nanoparticles with cell derived microvesicles for drug loading and targeting. *Nanomed.* Apr 2015;11(3):645-655.
322. Mertens ME, Koch S, Schuster P, et al. USPIO-labeled textile materials for non-invasive MR imaging of tissue-engineered vascular grafts. *Biomaterials.* Jan 2015;39:155-163.

323. Chen JP, Yang PC, Ma YH, Lu YJ. Superparamagnetic iron oxide nanoparticles for delivery of tissue plasminogen activator. *J Nanosci Nanotechnol.* Dec 2011;11(12):11089-11094.
324. Laurent S, Saei AA, Behzadi S, Panahifar A, Mahmoudi M. Superparamagnetic iron oxide nanoparticles for delivery of therapeutic agents: opportunities and challenges. *Expert Opin Drug Deliv.* Sep 2014;11(9):1449-1470.
325. Kaaki K, Herve-Aubert K, Chiper M, et al. Magnetic nanocarriers of doxorubicin coated with poly(ethylene glycol) and folic acid: relation between coating structure, surface properties, colloidal stability, and cancer cell targeting. *Langmuir.* Jan 17 2012;28(2):1496-1505.
326. Mai J, Huang Y, Mu C, et al. Bone marrow endothelium-targeted therapeutics for metastatic breast cancer. *J Control Release.* Aug 10 2014;187:22-29.
327. Hood ED, Chorny M, Greineder CF, I SA, Levy RJ, Muzykantov VR. Endothelial targeting of nanocarriers loaded with antioxidant enzymes for protection against vascular oxidative stress and inflammation. *Biomaterials.* Apr 2014;35(11):3708-3715.
328. Novokhatska T, Tishkin S, Dosenko V, et al. Correction of vascular hypercontractility in spontaneously hypertensive rats using shRNAs-induced delta protein kinase C gene silencing. *Eur J Pharmacol.* Oct 15 2013;718(1-3):401-407.
329. Hsu J, Bhowmick T, Burks SR, Kao JP, Muro S. Enhancing biodistribution of therapeutic enzymes in vivo by modulating surface coating and concentration of ICAM-1-targeted nanocarriers. *J Biomed Nanotechnol.* Feb 2014;10(2):345-354.
330. Dan M, Cochran DB, Yokel RA, Dziubla TD. Binding, transcytosis and biodistribution of anti-PECAM-1 iron oxide nanoparticles for brain-targeted delivery. *PLoS ONE.* 2013;8(11):e81051.
331. Yang H, Zhao F, Li Y, et al. VCAM-1-targeted core/shell nanoparticles for selective adhesion and delivery to endothelial cells with lipopolysaccharide-induced inflammation under shear flow and cellular magnetic resonance imaging in vitro. *Int J Nanomedicine.* 2013;8:1897-1906.
332. Hida K, Ohga N, Akiyama K, Maishi N, Hida Y. Heterogeneity of tumor endothelial cells. *Cancer Sci.* Nov 2013;104(11):1391-1395.
333. Dasgupta S, Auth T, Gompper G. Shape and orientation matter for the cellular uptake of nonspherical particles. *Nano Lett.* Feb 12 2014;14(2):687-693.
334. Hao N, Li L, Tang F. Shape-mediated biological effects of mesoporous silica nanoparticles. *J Biomed Nanotechnol.* Oct 2014;10(10):2508-2538.
335. Karagoz B, Yeow J, Esser L, et al. An efficient and highly versatile synthetic route to prepare iron oxide nanoparticles/nanocomposites with tunable morphologies. *Langmuir.* Sep 2 2014;30(34):10493-10502.
336. de Montferrand C, Hu L, Milosevic I, et al. Iron oxide nanoparticles with sizes, shapes and compositions resulting in different magnetization signatures as potential labels for multiparametric detection. *Acta Biomater.* Apr 2013;9(4):6150-6157.
337. Xia W, Song HM, Wei Q, Wei A. Differential response of macrophages to core-shell Fe3O4@Au nanoparticles and nanostars. *Nanoscale.* Nov 21 2012;4(22):7143-7148.
338. Munoz EM, Correa J, Riguera R, Fernandez-Megia E. Real-time evaluation of binding mechanisms in multivalent interactions: a surface plasmon resonance kinetic approach. *J Am Chem Soc.* Apr 24 2013;135(16):5966-5969.

339. Kolhar P, Anselmo AC, Gupta V, et al. Using shape effects to target antibody-coated nanoparticles to lung and brain endothelium. *Proc Natl Acad Sci U S A.* Jun 25 2013;110(26):10753-10758.
340. Parton RG, Simons K. The multiple faces of caveolae. *Nat Rev Mol Cell Biol.* Mar 2007;8(3):185-194.
341. Voigt J, Christensen J, Shastri VP. Differential uptake of nanoparticles by endothelial cells through polyelectrolytes with affinity for caveolae. *Proc Natl Acad Sci U S A.* Feb 25 2014;111(8):2942-2947.
342. Weis SM, Cheresh DA. Tumor angiogenesis: molecular pathways and therapeutic targets. *Nat Med.* 2011;17(11):1359-1370.
343. Gu G, Hu Q, Feng X, et al. PEG-PLA nanoparticles modified with APTEDB peptide for enhanced anti-angiogenic and anti-glioma therapy. *Biomaterials.* Sep 2014;35(28):8215-8226.
344. Ebos JM, Kerbel RS. Antiangiogenic therapy: impact on invasion, disease progression, and metastasis. *Nat Rev Clin Oncol.* Apr 2011;8(4):210-221.
345. Pardridge WM. Blood-brain barrier delivery. *Drug Discov Today.* Jan 2007;12(1-2):54-61.
346. Kemper EM, Cleypool C, Boogerd W, Beijnen JH, van Tellingen O. The influence of the P-glycoprotein inhibitor zosuquidar trihydrochloride (LY335979) on the brain penetration of paclitaxel in mice. *Cancer Chemother Pharmacol.* Feb 2004;53(2):173-178.
347. On NH, Kiptoo P, Siahaan TJ, Miller DW. Modulation of blood-brain barrier permeability in mice using synthetic E-cadherin peptide. *Mol Pharm.* Mar 3 2014;11(3):974-981.
348. Chrastina A, Massey KA, Schnitzer JE. Overcoming in vivo barriers to targeted nanodelivery. *Wiley Interdiscip Rev Nanomed Nanobiotechnol.* Jul-Aug 2011;3(4):421-437.
349. Jung YW, Lee H, Kim JY, Koo EJ, Oh KS, Yuk SH. Pluronic-based core/shell nanoparticles for drug delivery and diagnosis. *Curr Med Chem.* 2013;20(28):3488-3499.